Solution Processable Semiconducting TiO_x Thin Films for Photovoltaic Applications

---

A Dissertation
Presented to
the faculty of the School of Engineering and Applied Science
University of Virginia

In Partial Fulfillment
of the requirements for the Degree
Doctor of Philosophy in Electrical Engineering

by
Jiguang Li
August 2012

APPROVAL SHEET

The dissertation is submitted in partial fulfillment of the
requirements for the degree of
Doctor of Philosophy in Electrical Engineering

Jiguang Li

Jiguang Li

This dissertation has been read and approved by the examining Committee:

Professor Mool C. Gupta — Dissertation advisor

Professor Joe C. Campbell

Professor John Bean

Professor Lloyd Harriot

Professor Lin Pu

Accepted for the School of Engineering and Applied Science:

Dean, School of Engineering and
Applied Science
August 2012

Acknowledgment

First and foremost I would like to express my deep sense of gratitude to my advisor Professor Gupta for his tremendous technical, financial and moral support and insight throughout the years in my research. He has given me the opportunity to perform research in an exciting field at an excellent university. He has encouraged my intellectual growth. I have learned a lot of valuable skills from him.

I would like to thank Professor John Yates for his guidance. He has given me the opportunity to co-author a paper with a Nobel Prize winner. I would also like to thank Professor Lin Pu for his important suggestions and his generosity in allowing me to use his facilities to synthesize TiO_x material.

I would like to thank Professor Joe Campbell, Professor Lloyd R. Harriott and Professor John Bean for being on my annual review committee. The suggestions on my research are highly appreciated.

I would like to thank Albert DeBerardinis, Mark Turlington, Shanshan Yu and Wei Chen for their help during the material synthesis in the Chemistry department. I would also like to thank Sean Edington and Joseph Nedy for the degradation tests.

I would like to thank all of my fellow group members for their help. I want to thank Yang Shen for frequent academic discussion and support in my personal life. I want to thank Vikram Iyengar, Will Bagienski, and Vaishali Koppolu for help on problem discussions and facilities set up. I would also like to thank Dr. Chong Huang and Dr. B. K. Nayak, for helping me get started when I was new to the group. I would

also like to thank Keye Sun, Tyson Baldridge, Christian Rothenbach and Longteng Wang for their helpful discussion and experimental support.

I would like to thank Joe Beatrice, Harry Wade, Alex Lobo and Tim Pernell for clean room facility training and maintenance. I would like to thank departmental stuff Dan Fetko, Yadira Weaver, Elieen Thacker, Susan Malone and Gloria Walker for their help on numerous occasions.

I would like to thank Tyson Baldridge, Yang Shen, Maggie Varland, Christian Speck, and Kiet Tran for helping me to revise this dissertation.

Lastly I would like to thank my friends and family who encouraged and supported me throughout my academic career.

Abstract

Polymer based organic solar cells are promising due to advantages including light weight, mechanical flexibility and low cost roll-to-roll processing. Currently, organic solar cells have two major limitations, namely lower conversion efficiency and poor long-term environmental stability compared with inorganic solar cells. One method to address these limitations involves applying few tens of nanometer thin films of solution processable TiO_x in organic solar cell applications. The TiO_x thin film is used for enhancement of optical absorption and for protective coatings. The work described in this dissertation studied the properties and applications of this TiO_x material for organic photovoltaic devices.

The optical, structural, and morphological properties are important for optical applications. Optical constants were calculated by ellipsometry and modeling. X-Ray Diffraction (XRD) and Atomic Force Microscopy (AFM) were used to study the physical, structural and morphological properties. The results indicated that the sol-gel TiO_x may be used in optical thin film applications as an antireflection layer.

Electrical properties such as electrical resistivity and photoconductivity were studied. The resistivity of TiO_x was calculated as 1.5×10^7 $\Omega \cdot cm$ for the as-deposited films using vertical transmission line measurement model. The thermal annealing effect and temperature dependence of the resistivity of TiO_x thin films were also investigated.

The degradation of the PCBM/P3HT organic solar cell was studied under different UV light intensities and gas environments. Transmission infrared (IR) and Electron Spin Resonance (ESR) spectroscopies were used to study the chemical changes

of the TiO_x thin films under different conditions. The results suggested that the photochemical removal of O_2 by TiO_x films passivated the organic solar cells from oxygen induced degradation. The protection capacity by TiO_x films was calculated. Distribution of the local photocurrent in the cells with and without TiO_x protection layers were obtained by laser beam induced current measurements. The results demonstrated that the introduction of the TiO_x layer could effectively absorb water/oxygen from ambient air. TiO_x thin films protected the cells at the edge of the devices.

Further improvement of the TiO_x material properties was achieved by doping. Fe doped TiO_x material improves the organic solar cell efficiency while Cs doping does not benefit efficiency. The photovoltaic characteristic parameters such as efficiency, open circuit voltage, short circuit current and fill factor are reported.

The application of the TiO_x material on inorganic Si solar cells was also explored. Silicon solar cells using TiO_x thin films for surface passivation and anti-reflection coatings were successfully fabricated. The obtained efficiency of 15.7 % is comparable with devices using SiO_2 and Si_3N_4 as passivation and anti-reflection layers, respectively. The passivation effects were evaluated by near surface lifetime measurements.

This work covers the measurements of the fundamental optical and electrical properties, protection mechanism, modification and application of the TiO_x material.

Table of Contents

Chapter 1. Background....1

1.1 Photovoltaic....1

1.2 Titanium dioxide (TiO_2) material....4

1.2.1 TiO_2 properties....4

1.2.2 TiO_2 thin films applications....4

1.2.3 TiO_2 thin films fabrication....5

1.3. TiO_x material....5

1.3.1 TiO_x material properties....5

1.3.2 TiO_x thin films for protection of organic solar cells degradation....6

1.3.3 TiO_x thin films for Si solar cells....6

1.4 Objective of the research....7

1.5 Organization of the dissertation....8

Chapter 2. TiO_x precursor synthesis and thin films fabrication....11

2.1 TiO_x precursor synthesis....11

2.2 TiO_x thin films fabrication....12

2.2.1 Hydrolysis and condensation....12

2.2.3 Coating morphology....17

2.3 Summary....18

Chapter 3. Optical properties of TiO_x thin films....19

3. 1. Introduction....19

3. 2. Experiment....19

3.2.1. Thin films preparation....19

3.2.2. Sample characterization....20

3.3. Results and discussion....21

3.3.1. Optical constant....21

3.3.2 Film thickness....26

3.3.3 Surface morphology....26

3.3.4. Crystalline structure....28

3.3.5. Optical reflectance....31

3. 4. Conclusions....32

Chapter 4. Electrical resistivity of TiO_x thin films 34
4.1. Introduction 34
4.2. Experiment 35
4.2.1. Device fabrication 35
4.2.2 Electrical characterization 36
4.3. Results and discussion 37
4.3.1 Electrical resistance measurement 37
4.3.2 Temperature ependence of electrical resistance 41
4.3.3 Electrical resistivity after thermal annealing 42
4.3.4 Photoconductivty under UV illumination 43
4.4. Conclusion 44
Chapter 5. Organic solar cells: device physics, fabrication and characterization 46
5.1 Introduction 46
5.2 Development of polymer solar cells 46
5.3 Operating principles 47
5.4 Materials 49
5.5 Device structure 52
5.7 Fabrication of organic solar cells 54
5.6 Organic solar cell characterizations 56
5.7 Conclusion 59
Chapter 6. Stabilization of P3HT/PCBM organic solar cells by photochemical active TiO_x layer 60
6.1. Introduction 60
6.2. Experimental 61
6.3. Results and Discussion 67
6.3.1. Study of solar cell degradation and improvements by TiO_x 67
6.3.2. TiO_x improvement mechanism study 77
6.3.3 Protection capacity calculation 82
6.4. Conclusions 83
Chapter 7. Laser beam induced current mapping study on organic solar cell with TiO_x protection layer 85
7.1 Introduction 85
7.2 Experiment 86
7.2.1 Organic solar cell fabrication 86

7.2.3 LBIC set up 86
7.3 Results and discussion 88
7.3.1 Efficiency patterns 88
7.3.2 Island formation 89
7.3.3 Comparison of devices with/without TiO_x protection 91
7.4 Conclusion 97
Chapter 8. A study on doping of TiO_x thin films 98
8.1 Introduction 98
8.2 Experiment 100
8.2.1 TiO_x precursor doping 100
8.2.2 Resistivity measurement 100
8.2.3 Organic solar cell fabrication 101
8.3 Results and discussion 101
8.3.1 Fe doped TiO_x 101
8.3.2 Cs doped TiO_x 104
8.4 Conclusion 105
Chapter 9. TiO_x thin films as surface passivation and anti-reflection coating for silicon solar cells 106
9.1 Introduction 106
9.2 Experiment 106
9.3 Results and discussion 108
9.3.1 Optical measurement 108
9.3.2 Photovoltaic device characterization 109
9.3.3 Surface passivation 111
9.4 Summary 114
Chapter 10. Summary and future work 115
10.1 Summary 115
10.2 Future work 117
10.2.1 Optical absorption enhancement by textured structure 117
10.2.2 Further improvement from degradation 119
10.2.3 TiO_x material property tuning 120
Appendix 122
Publications: 122

Presentations: 123
References ……..124

List of Figures

Figure 1-1: Global, average PV module prices, all PV technologies, 1984-2010, $/W$_p$ stands for the prices that are not adjusted for inflation. 2010 $/W$_p$ stands for the prices that are adjusted for inflation. 2
Figure 2-1: Experimental set up for TiO_x precursor synthesis.....12
Figure 2-2: The FTIR spectrum of spinning coated TiO_x film 14
Figure 2-3: The FTIR spectrum of TiO_x films on CaF_2 during hydrolysis process. Blue line represents the sample in the high humidity environment; red line represents the sample in the high humidity environment. (a) Fresh sample (b) Hydrolysis process for 30 minutes (b) Hydrolysis process for 4 hours (d) Hydrolysis process for 20 hours.....16
Figure 2-4: (a) Optical image of a polished silicon surface spin coated with TiO_x film and (b) SEM image of a chemically textured silicon surface coated with 40 nm of TiO_x film.....18
Figure 3-1: Three layers model of TiO_x films [] 21
Figure 3-2: The variation of refractive index with wavelength when TiO_x films are annealed at various temperatures in (a) forming gas, (b) O_2 atmosphere, The variation of extinction coefficient (k) with wavelength when TiO_x films are annealed at various temperatures in (c) forming gas, (d) O_2 atmosphere[41] 25
Figure 3-3: (a) AFM image of as deposited film (b) AFM image of film annealed in O_2 at 900 ℃ for 10 minutes (c) AFM image of film annealed in forming gas at 900 ℃ for 10 minutes[41] 28
Figure 3-4: The XRD spectra for TiO_x films annealed in (a) forming gas and (b) O_2 at various temperatures of 400 ℃, 500 ℃, 700 ℃ and 900 ℃, respectively. R (1 1 0) stands for the Rutile peak at $2\theta = 27.5°$, A (1 0 1) stands for the Anatase peak at $2\theta = 25.6°$ [41].....30
Figure 3-5: The measured optical reflectance from TiO_x thin films coated Si substrate for different thickness and annealing conditions, including as deposited TiO_x films before annealing, TiO_x films annealed in forming gas and in oxygen at 400 ℃. The reflectance from bare silicon and commonly used Si_3N_4 antireflection coating layer on Si are also shown. Si_3N_4 film thickness is 70 nm [41] 32
Figure 4-1: (a) ITO-TiO_x-Al device structure for vertical transmission line resistance measurement (b) Device structure to process sample at high- temperature annealing studies.....36
Figure 4-2: Schematic showing equivalent circuit for diode 37
Figure 4-3: (a) Typical I-V curve for ITO-TiO_x-Al structure, (b) *I(dV/dI)-I* characteristic curve of the ITO-TiO_x-Al structure 39
Figure 4-4: The variation of total resistance with TiO_x film thickness.....40

Figure 4-5: Electrical resistance of an ITO-TiO_x-Al device with 40 nm TiO_x thin films at the temperature ranging from 20 ℃ to 140 ℃ 41
Figure 4-6: Electrical resistivity of TiO_x after different annealing temperatures. Different values at same temperature stands for different samples.....43
Figure 4-7: The photoconductivity response of TiO_x sample (annealed at 500 ℃) at room temperature in air.....44
Figure 5-1: Operation mechanism of polymer organic solar cells. 49
Figure 5-2: Chemical structure of PCBM 50
Figure 5-3: Chemical structure of P3HT.....51
Figure 5-4: Chemical structure of PEDOT: PSS.....51
Figure 5-5: Organic solar cell device structure and band diagram.....53
Figure 5-6: Schematic representation of the spatial distribution of the squared optical electricfield strength $|E|^2$ inside the devices with a structure of ITO/PEDOT/active layer/Al (left) and ITO/PEDOT/active layer/optical spacer/Al (right). From J. Y. Kim [6].....54
Figure 5-7: Fabrication process of organic solar cells in our experiment 56
Figure 5-8: (a) the experiment set up for characterization of the organic solar cells in this dissertation. (b) Current-voltage (I-V) curves of an organic solar cell. the maximum current density and voltage defined as I_{MP} and $V_{MP.}$ V_{oc} is open circuit voltage, I_{sc} is short circuit current. FF is fill factor.....57
Figure 6-1: Organic solar cell device structure [].....62
Figure 6-2: Organic solar cell fabrication process: Color coded for process in air (purple) and process in vacuum (orange) [73].....62
Figure 6-3 500 W Hg UV lamp spectrum, AM 1.5 solar spectrum and transmission of FGUV11S band pass filter [73] 64
Figure 6-4: Experiment set up for UV irradiation 65
Figure 6-5: Variation of normalized organic solar cell efficiency in air and nitrogen in dark with time [73] 68
Figure 6-6: Variation of normalized organic solar cell efficiency under combined effect of UV and air exposure (UV power density = 10 mW/cm^2)[73].....68
Figure 6-7**:** Variation of normalized organic solar cell efficiency with UV exposure time while the sample was in a nitrogen atmosphere. (UV power density = 10 mW/cm^2)[73] 69
Figure 6-8**:** Variation of normalized organic solar cell efficiency with UV exposure time while the sample was surrounded by the 1 atmosphere oxygen environment. (weak UV power density = 10 mW/cm^2 and strong UV power density = 300 mW/cm^2)[73].....70

Figure 6-9: Variation of (a) open circuit voltage(V_{oc}), (b) short circuit current (I_{sc}) and (c) fill factor with UV exposure time when sample was surrounded by nitrogen atmosphere (UV power density = 10 mW/cm^2) [73] 72
Figure 6-10: Current voltage characteristics data indicating the significant change in I-V curve shape due to air degradation[73] 73
Figure 6-11: Optical path for absorption measurement of quartz substrate and TiO_x film on quartz. 74
Figure 6-12: Absorption spectrum of quartz substrate and TiO_x film on quartz 75
Figure 6-13: The calculated absorption of 20 nm TiO_x films (a) absorption spectrum (b) corresponding absorption coefficient 76
Figure 6-14: Gas phase photooxidation products from TiO_x films containing alkoxide functionalities. CO_2 (gas) and H_2O (gas) are observed. The slow formation of ice on the IR detector is an artifact to be disregarded. The spectrum through the gas phase at each time was ratioed by the spectrum taken before UV irradiation [73] 78
Figure 6-15: Surface species consumption and formation during photooxidation of TiO_x films containing alkoxide functionalities. The consumption of the alkoxide functionality is accompanied by the formation of carboxylate and hydroxyl surface-bound species, as well as nitrile moieties from the oxidation of ethanolamine [73] 79
Figure 6-16: ESR spectrum showing the effect of UV light on TiO_x under O_2 at 1 atm. (a) after UV irradiation, 15 minutes; (b) before irradiation[73] 80
Figure 6-17: ESR spectrum of the effect of UV light on TiO_x under N_2 at 1 atm. (a) after UV irradiation, 60 minutes; (b) before irradiation. The results, compared to Figure 6-16, show that O_2^- species require O_2(g) for photochemical formation on TiO_x[73] 81
Figure 7-1: A schematic of LBIC set up 87
Figure 7-2: LBIC mapping of as prepared devices (a) with TiO_x (device efficiency η=2.4) (b) without TiO_x (device efficiency η=1.6) 89
Figure 7-3: Degradation pattern of OSC device with TiO_x layer (a) as prepared device (b) device degraded in dark for 1 week. 91
Figure 7-4: The mapping of degradation process for device without TiO_x protection (a) as prepared device (b) degradation after 1 day (c) degradation after 3 days (d) degradation after 10 days 93
Figure 7-5: The current mapping of degradation process for device with TiO_x protection (a) as prepared device (b) degradation after 1 day (c) degradation after 5 days (d) degradation after 10 days 96

Figure 7-6: The current mapping of degradation without TiO_x protection (a) as prepared device (b) device after 1 week. 97
Figure 8-1: Energy level of TiO_2 changes after Fe doping, From C.-Y. Wang et. al 2003 99
Figure 8-2: TiO_x between to electrodes to measure the resistivity 101
Figure 8-3 : I-V curve of device with 1 % Fe doped TiO_x under 1 sun light illumination. Ref stands for devices without TiO_x, TiO_x and doped TiO_x stand for devices with original TiO_x and doped TiO_x material, respectively 103
Figure 8-4: The resistivity of TiO_x material upon doping with Fe of different concentration..... 103
Figure 8-5 : I-V curve of device with 1% TiO_x of different Cs doping level. 104
Figure 9-1: Process flow for fabricating silicon solar cells [46] 107
Figure 9-2: (a) Pattern and (b) experimental set-up for surface lifetime measurement [46] 108
Figure 9-3: Total integrated reflection for a chemically textured surface with and without TiO_x films [46] 109
Figure 9-4: Device structures for Si solar cells with (a) SiO_2 and Si_3N_4 layer and (b) TiO_x layer 109
Figure 9-5: (a) Dark and light I-V curves and (b) external quantum efficiency and reflection curves for Si solar cells with TiO_x thin films as the surface passivation and anti-reflection coating[46] 110
Figure 9-6: (a) Dark and light I-V curves and (b) external quantum efficiency and reflection curves for Si solar cells with TiO_x thin films as the surface passivation and anti-reflection coating on chemically textured surface [46] 111
Figure 9-7: (a) The passivation on n-type wafer, (b) The passivation on p-type wafer,..... 114
Figure 10-1: Non-conformal coating on top of textured substrate 118
Figure 10-2: TiO_x on the top of the non-conformal coating on textured substrate..... 119
Figure 10-3: Proposed structure of device with TiO_x and nickel oxide protection layer 120

List of Tables

Table 3-1: Modeling parameters for refractive index simulation.....22
Table 3-2: Layer thickness at different thermal annealing conditions 26
Table 6-1: Initial photovoltaic characterization parameters 63
Table 6-2: Comparison of efficiency degradation with time for the device with TiO_x protection and device without TiO_x.....83
Table 7-1: The photovoltaic parameters of the device for LBIC study 86
Table 8-1 The photovoltaic parameters of devices with Fe doped TiO_x.....102
Table 8-2: Photovoltaic parameters of devices of different doping levels at various TiO_x concentration levels 104
Table 9-1: Device performance for the Si solar cells with TiO_x layer and SiO_2 and Si_3N_4 layers 109

Chapter 1. **Background**

1.1 Photovoltaic

With the rising concerns of fossil fuel depletion and global warming, there is a growing demand for renewable and clean energy sources. Photovoltaic (PV) cells are one of the most promising choices. Of all the renewable resources, solar is by far the most abundant [1]. Photovoltaic solar power has several advantages. For example, photovoltaic cell modules produce no emissions and can be installed and operated anywhere including remote locations and areas with poor accessibility.

Photovoltaics are also currently one of the most expensive sources of renewable energy. Two categories of PV cells are used in most commercial PV modules: crystalline silicon and thin film. The crystalline silicon PV cells are the most efficient of the mainstream PV technologies and accounted for about 84% of PV cells produced in the world in 2008 [2].

Higher-efficiency modules require less installation area per watt of electricity production than lower-efficiency modules. Photovoltaic modules have undergone significant cost reductions over the last few decades, which is illustrated in Figure 1-1[2], and shows the average global PV module selling prices for all PV technologies. Thin-film PV technologies achieved lower manufacturing costs and selling prices than crystalline silicon modules.

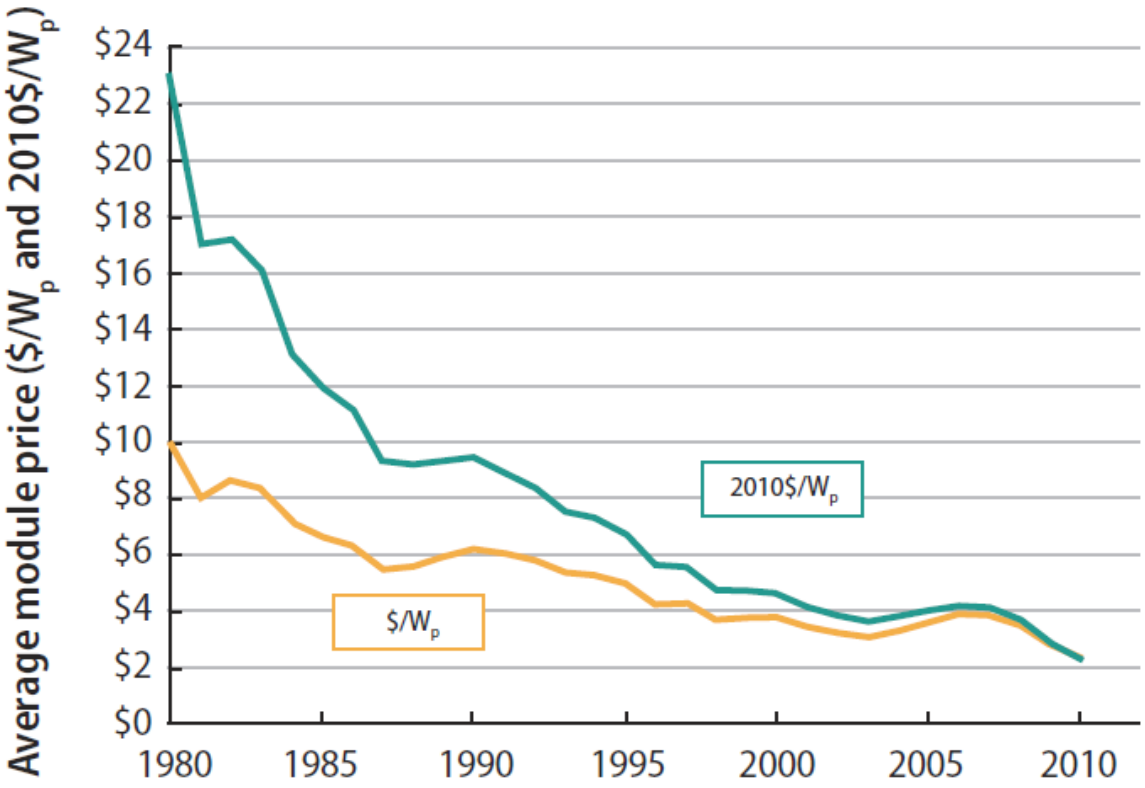

Figure 1-1: Global, average PV module prices, all PV technologies, 1984-2010, $/W$_p$ stands for the prices that are not adjusted for inflation. 2010 $/W$_p$ stands for the prices that are adjusted for inflation [2].

The price is affected by many factors such as efficiency. The current estimated effect is a $0.10 increase in price per 1 % increase in efficiency. One way to reduce the cost is to simplify the processing techniques. Currently, Si solar cell fabrication requires special processes. For example, the anti-reflection coating and surface passivation are achieved by depositing silicon nitride using plasma enhanced chemical vapor deposition (PECVD). However, PECVD deposition is time consuming and relatively expensive. Alternatively, solution processable techniques can be cost effective for anti-reflection and surface passivation.

Organic solar cells offer the potential for substantial manufacturing cost reductions. Organic semiconductors have relatively strong absorption coefficient (usually $>10^5$ cm^{-1}) [1]. Therefore they offer the possibility for the production of very thin solar cells with low specific weight. Organic solar cells can be manufactured using highly efficient ink-jet printing. Organic semiconductors can also be deposited on thin flexible substrates that enable integration within products while keeping the weight low. Concisely, low manufacturing costs can be attained by processing photovoltaic modules with large-area manufacturing technologies such as high-throughput roll-to-roll printing techniques onto flexible substrates.

One of the most promising device structures for organic solar cells is the bulk-heterojunction, which leads to several breakthroughs in efficiency, reaching 10.6 % [3]. It composes the blend of a hole-conducting and electron-donating conjugated polymer, such as the low-bandgap conjugated polymer: poly{2,6′-4,8-di(5-ethylhexylthienyl)benzo[1,2-b;3,4-b]dithiophene-alt-5-dibutyloctyl-3,6-bis(5-bromothiophen-2-yl)pyrrolo[3,4-c]pyrrole-1,4-dione} (PBDTT-DPP), and an electron-conducting and electron-accepting compound, such as [6,6]-phenyl-C_{71}-butyric acid methyl ester ($PC_{71}BM$).

The short operational stability and lifetime remain as the key issues of organic solar devices. The organic devices are vulnerable to the diffusion of ambient oxygen or humidity into the active layer. The devices degrade quickly when exposed to air. Improvement of stability that could comply with concepts such as the simple fabrication by solution processing, flexibility, and thin form factor are desired for further progress.

Recently, Heeger's group demonstrated that novel sol-gel TiO_x thin films could dramatically increase the efficiency and lifetime of organic solar cells by using it as an

optical spacer, hole blocking layer, and oxygen protecting layer [4, 5, 6]. In this project, we explore this novel solution processable semiconducting TiO_x thin films for low cost photovoltaic applications through investigation of fundamental properties, protection mechanism, and modification of the TiO_x materials.

1.2 Titanium dioxide (TiO_2) material

1.2.1 TiO_2 properties

TiO_2 is a relatively abundant material, existing in nature as the minerals in rutile, anatase, and brookite. TiO_2 thin films are generally amorphous for low deposition temperatures (≤ 350℃). The properties of TiO_2 thin films strongly depend on the phase of the material and processing techniques. Typically, TiO_2 has high electrical resistance with resistivity of 10^{14} Ω cm [7]. It shows excellent optical transmittance in the visible region.

The electrical conductivity, photoconductivity, and structural and optical properties of TiO_2 made using different processing techniques and conditions have been extensively studied.

1.2.2 TiO_2 thin films applications

TiO_2 thin films have been extensively used in optical device applications, including planar waveguides [8], diffraction gratings [9], self-cleaning optical coatings [10], infrared detectors [11], and electrochromic displays [12].

The high refractive index and low absorbance at visible wavelengths make TiO_2 well suited for solar cells applications, such as anti-reflection coatings [13], surface

passivation [14], transparent conducting oxide layers [15], and transparent electrodes in dye sensitizer solar cells [16].

1.2.3 TiO_2 thin films fabrication

Various methods are available for the fabrication of the TiO_2 films, including the sol-gel method [17,18], electron-beam evaporation [19], electrodeposition [20], plasma enhanced chemical vapor deposition (PECVD) [21,22], sputtering [23], atmospheric pressure chemical vapor deposition (APCVD) [24], laser ablation [25], ion assisted deposition [26], and ultrasonic spraying [27]. The properties of the TiO_2 films can be modified by different processing conditions.

The sol-gel method is one of the most promising techniques. It is a simple and low cost process. TiO_2 can be synthesized numerous ways. For example, Phadke et al. produced TiO_2 thin films by spin coating a solution made from titanium isopropoxide, acetic acid and 1-butanol on silicon substrates [17]. Sankapal et al. used titanium peroxide (titanium peroxo-complex) as a titanium source to produce nanocrystalline TiO_2 (anatase) thin films [18]. Kaewwiset et al. prepared TiO_2 sol-gel from titanium tetra isopropoxide in isopropanol by adjusting the pH of the solution using nitric acid [28].

1.3. TiO_x material

1.3.1 TiO_x material properties

The TiO_x produced by Heeger's group contains Ti : O = 42.1:56.4 as determined by X-ray photoelectron spectroscopy (XPS) measurement [6]. TiO_x material contains ···Ti-O-Ti··· interpenetrating structures. The uniform dense TiO_x films are

semiconducting. In TiO_x, the electron mobility is higher as compared to the amorphous oxide films prepared by the typical sol–gel processes. The sol-gel precursor is stable, can be used for coatings after synthesis, and does not require any acid catalyst unlike the previously mentioned work.

1.3.2 TiO_x thin films for protection of organic solar cells degradation

Degradation of organic solar cells in general has been investigated by several groups. Kwano et al. showed that water absorption by the PEDOT: PSS layer accounted for some of the observed degradation [29]. Reese et al. concluded that the metal/organic interface can be a major source of degradation [30]. Gevorgyan et al. reported that the degradation mechanism in ambient atmosphere was related to chemical reactions of the active layer and metal electrodes with O_2 and H_2O [31]. The decay of organic solar cells is complex and may involve several mechanisms.

Different approaches of achieving higher stability have been considered, such as using improved active materials and encapsulation schemes. Lee et al. demonstrated the enhanced stability of polymer light emitting diodes and polymer solar cells by incorporating a solution processable TiO_x layer between the active layer and the metal electrode [5]. TiO_x has been used to block the passage of oxygen and humidity into active layer. The TiO_x layer provided the protection from O_2 and H_2O.

1.3.3 TiO_x thin films for Si solar cells

Various groups have studied titanium dioxide (TiO_2) films deposited by CVD, sputtering and sol-gel methods for anti-reflection and surface passivation [32,33,34]. The surface passivation of silicon is usually accomplished by annealing the TiO_2 layer in an

oxygen rich atmosphere which leads to the formation of an interfacial silicon dioxide layer. The other mechanism of surface passivation can be due to the accumulation of interfacial charges, either positive or negative, depending on the stoichiometry [35] of the films or light-induced effects. The most notable one being in 1987 where the authors evaporated Ti in an oxygen ambient [36]. There are few reports, however, which demonstrate the incorporation of solution processable TiO_x films for surface passivation and an anti-reflection coating, and its application for silicon solar cells.

1.4 Objective of the research

The objective of the research is to study TiO_x materials for photovoltaic applications. Optical and electrical properties are critical in photonic devices for the light absorption and carrier transport. Therefore, we studied the optical and electrical properties of TiO_x. The optical properties of TiO_x thin films were investigated as a function of wavelength using ellipsometric and optical reflection technique. The XRD and AFM were used to study the TiO_x phase, density and morphology changes under thermal annealing. The electrical resistivity of solution processable semiconducting TiO_x thin films was investigated. TiO_x bulk resistance and contact resistance were extracted from the vertical transmission line measurement model. Temperature dependence of the electrical resistivity and the variation of electrical resistivity with different annealing temperature will be studied.

To verify the postulation that photo-oxidation of the bound organic moieties causes oxygen gas scavenging, we examined the individual effect of oxygen and UV radiation as well as their combined effect on the degradation behavior of P3HT/PCBM organic solar cell devices and the improvements provided by placing the TiO_x layer

between the active layer and a metal electrode. IR and ESR spectroscopy measurements were used to examine the chemical composition of the films.

Laser beam induced current mapping was used to obtain the local current distribution of the device with/without TiO_x protection. This data improves the understanding of the protection mechanism.

The modification of the TiO_x material was explored since the TiO_x layer changes the series resistance of the organic solar cells. Doping the metal oxide can improve the electrical properties of the material. We examined the doping effects of Cs and Fe doping on TiO_x material as well as the effects on the organic solar cell performance.

The application of solution processable TiO_x thin films for silicon solar cells was studied. TiO_x thin films were used as anti-reflection and passivation layers. The surface passivation quality of these films was evaluated by surface lifetime measurement.

1.5 Organization of the dissertation

This dissertation is organized in 10 chapters as follows:

Chapter 1 gives a brief introduction of the photovoltaic market and the basic properties of TiO_2 and TiO_x material.

Chapter 2 describes the TiO_x precursor synthesis and thin films fabrication. The TiO_x thin films were formed through hydrolysis and condensation. The humidity effects on the hydrolysis process were studied by infrared (IR) spectroscopy.

Chapter 3 details the optical properties of TiO_x thin films. The optical constants of the TiO_x films were studied by ellipsometric technique and 3-layer modeling. Crystalline structure and surface morphology were examined to explore the origin of the changes of optical constants of TiO_x thin films.

Chapter 4 provides the electrical resistivity of TiO_x thin films, including electrical resistivity of as-deposited films, temperature dependence of electrical resistance of Al/TiO_x/ITO structure, thermal annealing effect on TiO_x thin films and photoconductivity under UV illumination.

Chapter 5 gives the introduction of organic solar cells, such as the development of polymer solar cells, operating principle, donor/acceptor materials and characterization parameters for organic solar cells. The device structure and fabrication of polymer solar cells used in this dissertation are introduced.

Chapter 6 presents a study of stabilization of P3HT/PCBM organic solar cells by a photochemically active TiO_x layer. Degradation and improvements by TiO_x of organic solar cells under different condition is shown. The photovoltaic characterization parameters are analyzed. The protection mechanism is investigated using IR and ESR spectroscopy techniques. Protection capacity is calculated.

Chapter 7 presents further study on the TiO_x protection using a laser beam induced current mapping technique. The efficiency patterns, island formation and comparison of devices with/without TiO_x protection are analyzed.

Chapter 8 shows the results on doping TiO_x material with Fe and Cs for further improvement, such as the doping effects on TiO_x resistivity and organic solar cell performance.

Chapter 9 describes the application of TiO_x thin films in Si solar cells. The photovoltaic device characterization results for Si solar cells with TiO_x thin films as a surface passivation and anti-reflection coating are shown. Surface passivation is evaluated using results from the near-surface lifetime measurement technique.

Chapter 10 summarizes the work in this project and shows some possible directions for future work.

Chapter 2. TiO_x precursor synthesis and thin films fabrication

2.1 TiO_x precursor synthesis

The TiO_x material is synthesized using sol-gel chemistry according to reference [4]. The experimental set up is shown in Figure 2-1. All the glassware was left in a heating oven overnight to remove moisture.

The sol–gel procedure started with the injection of titanium isopropoxide [Ti (OCH $(CH_3)_2)_4$] (Aldrich, 99.999 %, 2 ml), 2-methoxyethanol [$CH_3OCH_2CH_2OH$] (Aldrich, 99.9+ %, 8 ml) and ethanolamine [$H_2NCH_2CH_2OH$] (Aldrich, 99.5+ %, 0.8 ml) one by one into a three-necked flask connected with water condensers and a nitrogen gas inlet at room-temperature. The mixed solution was stirred for 1 hour at room-temperature. Then it was heated at 80 ℃ for 1 hour, followed by heating to 120 ℃ for 1 hour until the solution was transformed to a low-density viscous gel with a dark wine color. The inside of the flask was supplied with continuous dry N_2, and the mixed solution was stirred continuously during the experiment. After cooling to room temperature, 4 ml methanol was injected to extract the final TiO_x sol–gel product.

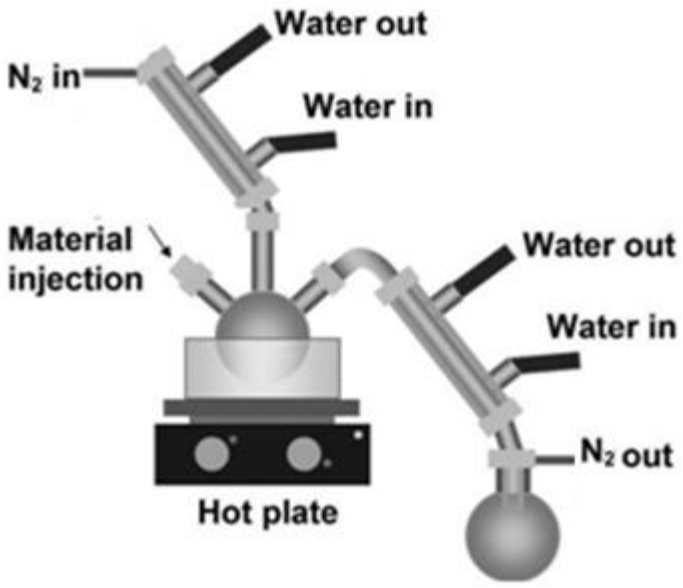

Figure 2-1: Experimental set up for TiO_x precursor synthesis

2.2 TiO_x thin films fabrication

2.2.1 Hydrolysis and condensation

Hydrolysis and condensation occurs when the TiO_x sol–gel is taken out into air, which contains water molecules, resulting in the formation of Ti–O–Ti linkages. These reactions occur slowly in the solution form, because the methanol solution inhibits the interaction of the TiO_x with moisture in the ambient environment. The reactions are significantly accelerated, however, after spin casting to form thin solid films.

At present, the hydrolysis reaction scheme proposed by Livage [37] is generally accepted. The first step comprises substitution of one alkoxy group with a hydroxy group by a nucleophilic mechanism:

```
H-O +Ti-OR  =>      H-O:->Ti-OR  => Ti-OH + R-OH
  |                   |
  H                   H
```

In the second step, -Ti-O-Ti- bridges form during the course of condensation reactions:

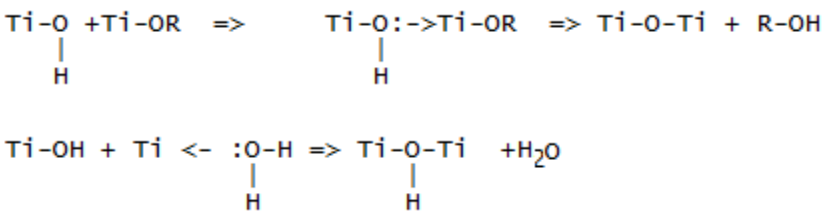

The thickness of the films can be controlled by adjusting sol-gel concentration and the spinning speed.

The water molecules act as a catalyst in the hydrolysis process. Therefore humidity affects the reaction speed of the hydrolysis process. The C-H components in the –OR group should evaporate after hydrolysis. Therefore we can monitor the C-H component to characterize the hydrolysis process.

Fourier transform infrared spectroscopy (FTIR) is a useful tool for identifying types of chemical bonds (functional groups). FTIR can be used to identify chemical groups in spills, paints, polymers and coatings. The wavelength of light absorbed is characteristic of the chemical bond. By interpreting the infrared absorption spectrum, the chemical bonds in a molecule can be determined.

The experiment setup for the humidity effect measurement is described as follows:

The TiO_x material was dissolved to 10 % by volume in methanol, and used at room temperature to spin coat ~ 200 nm films onto a CaF_2 single crystal disk, which is transparent in the visible-infrared wavelength. The CaF_2 disk was 25 mm in diameter and 5 mm in thickness. Transmission IR measurements were made with a Nicolet Avatar 330 FT-IR spectrometer.

Two samples were made to compare the hydrolysis process in high and low humidity environments. One sample stayed in normal condition. The humidity was measured as 40 % by humidity meter. Another sample was put on the top of a humidifier, which generates water vapors at room temperature. The humidity was measured as 70 %.

The FTIR spectrum of spinning coated TiO_x film is shown in Figure 2-2. C-H bonds peak appears around 3000-2750 wave number (cm^{-1}), as shown in the black circle region in the Figure. This C-H bond peak region is the characteristic of the alkoxide functional groups remaining in the TiO_x films. The absorbance indicates the quantity of the C-H bonds in the films.

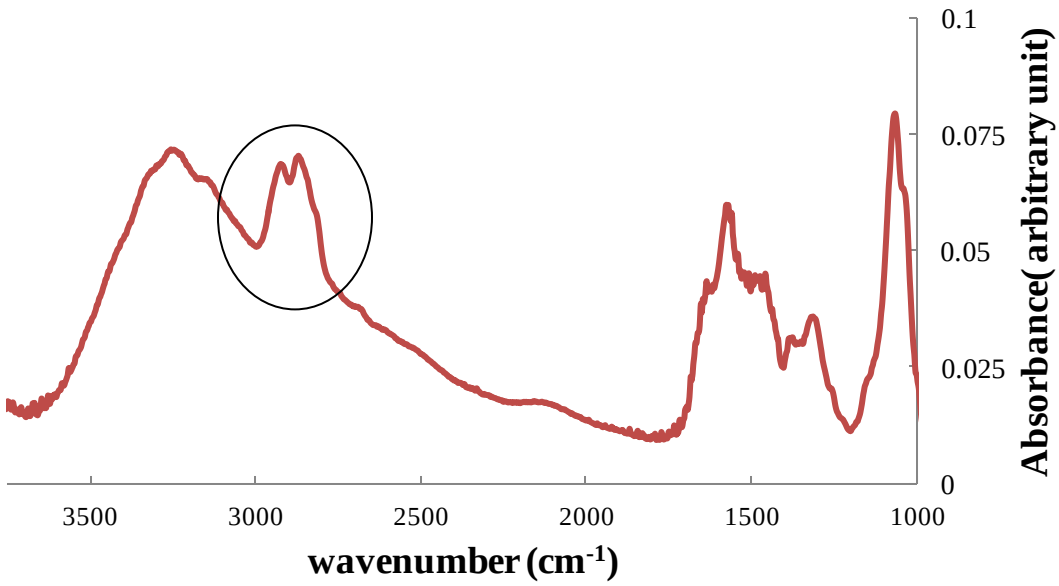

Figure 2-2: The FTIR spectrum of spin coated TiO_x film

The FTIR spectrum after hydrolysis process is shown in Figure 2-3. The C-H bond position is basically identical for the two fresh samples right after spin coating, as shown in Figure 2-3 (a). There are obviously differences after 30 minutes in different humid environment, as shown in Figure 2-3 (b). The absorbance of the C-H bonds region

is lower for the sample in the high humidity environment. This indicates the hydrolysis process is faster in the high humidity environment. There are still differences for the samples after 4 hours in different humid environments, as shown in Figure 2-3 (c). However, the spectrums of the two samples become similar after 20 hours, as shown in Figure 2-3 (d), which indicates that the hydrolysis is complete. The time frame is consistent with the hydrophobic/hydrophilic measurement reported by Heeger's group [4].

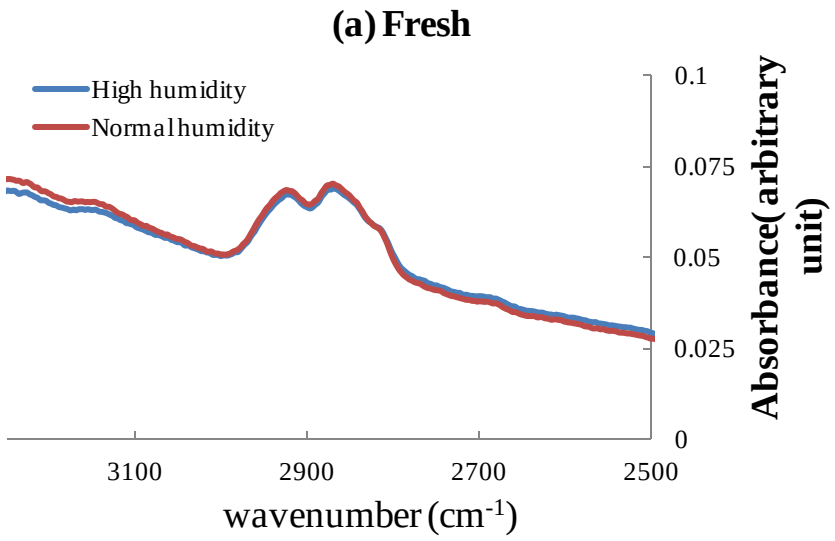

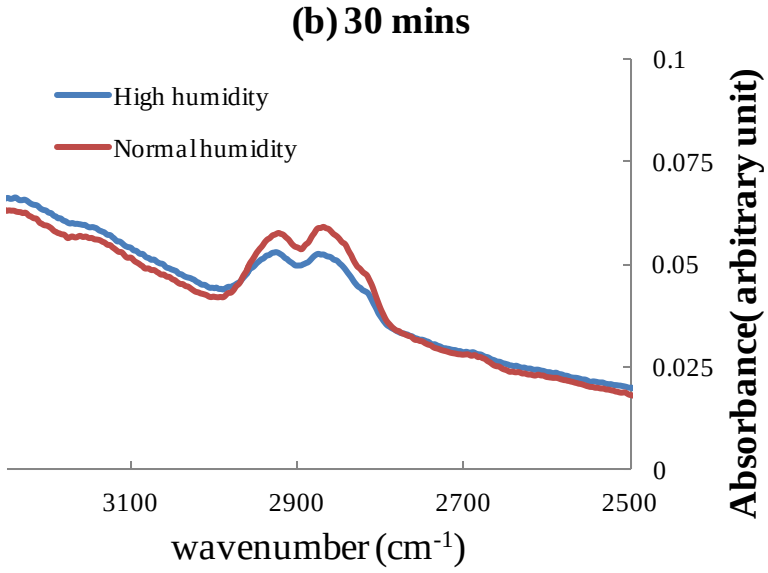

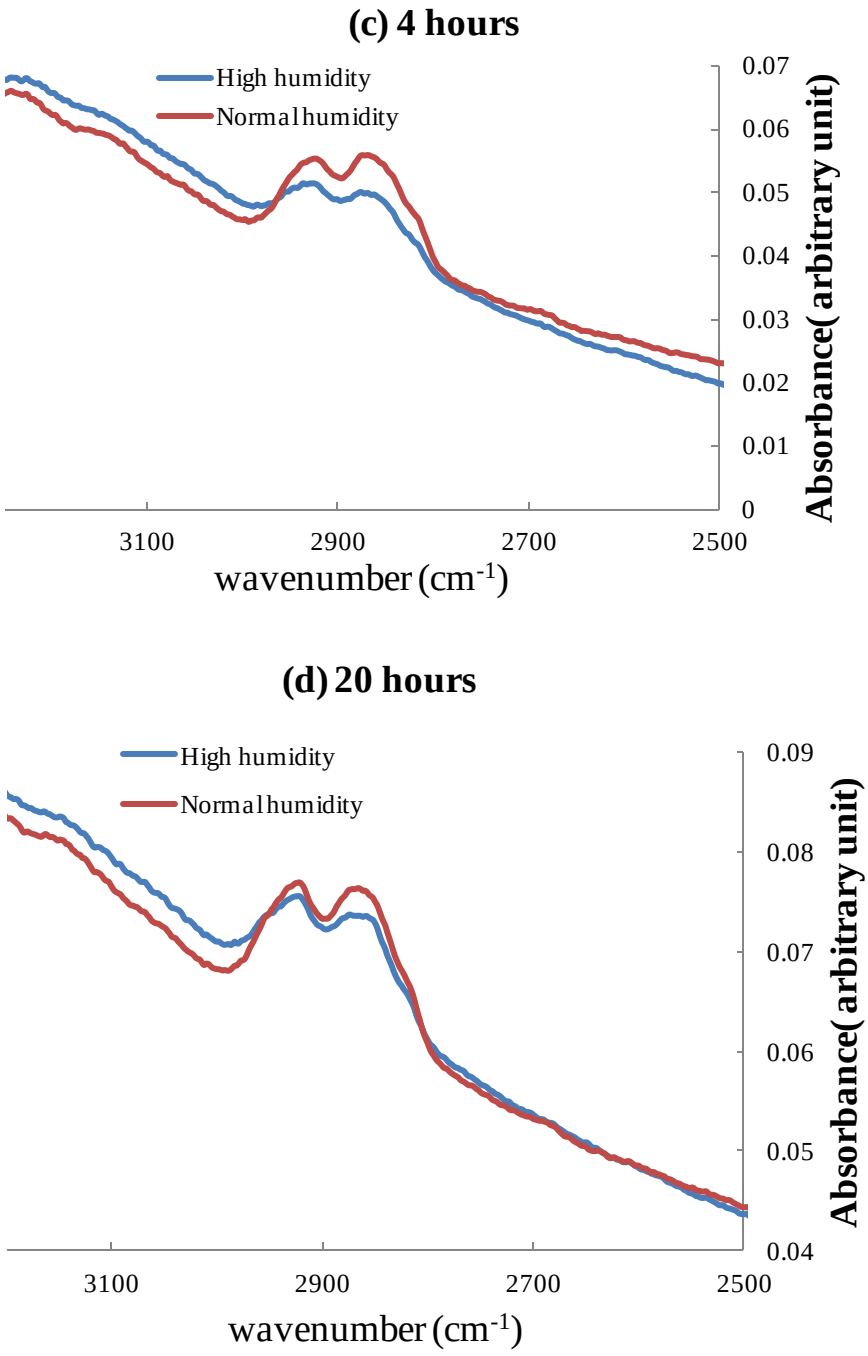

Figure 2-3: The FTIR spectrum of TiO_x films on CaF_2 during hydrolysis process. Blue line represents the sample in the high humidity environment; red line represents the

sample in the high humidity environment. (a) Fresh sample (b) Hydrolysis process for 30 minutes (b) Hydrolysis process for 4 hours (d) Hydrolysis process for 20 hours

2.2.3 Coating morphology

The TiO_x sol gel can be spin-coated on flat substrates such as silicon, quartz, glass and so on. It forms uniform thin films as shown in Figure 2-4 (a).

The spin-coating process on the P3HT: fullerene active layer surface is not straightforward. Because of hydrophobicity of P3HT (particularly alkyl chain of P3HT), wetting is not good. To obtain good TiO_x films on the surface of P3HT: fullerene active layer, waiting for approximately 1 min is required after dropping the TiO_x solution, then the spinning starts.

The TiO_x thin films also conform well to the chemically textured silicon surface as shown in the SEM image in Figure 2-4 (b). Placing a spin-coated sample directly on an 80 ^oC hot plate led to cracked films with poorer quality. Coating thicker films in a single step leads to solution accumulation between texture cones and severe cracking of the films was observed. Therefore ramp heating and thin layer coating were used to achieve uniform coating. A 20 nm TiO_x film was spin-coated followed by ramp soft-baking from 25 ^oC to 80 ^oC in 20 minutes. Next, an additional 20 nm of TiO_x film was spin-coated followed by soft-baking.

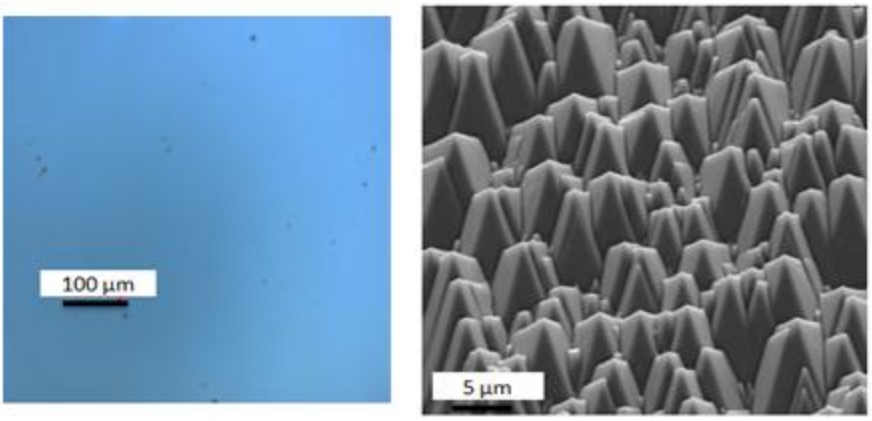

Figure 2-4: (a) Optical image of a polished silicon surface spin coated with TiO_x film and (b) SEM image of a chemically textured silicon surface coated with 40 nm of TiO_x film

2.3 Summary

In this chapter, we described the synthesis and thin film fabrication of the TiO_x material. The effect of humid on the hydrolysis process in thin film formation was studied. The hydrolysis process was accelerated in the high humidity environment. The coating properties on different substrates were also characterized.

Chapter 3. Optical properties of TiO_x thin films

3. 1. Introduction

As stated in chapter 1, titanium dioxide (TiO_2) thin films have been extensively used in optical device applications. Various methods are available for the fabrication of the TiO_2 films, including sol-gel method, electron-beam evaporation, electro-deposition and PECVD. The properties of the TiO_2 films can be modified by different processing conditions, as a consequence, the optical properties of thin films change. Sol-gel method is one of the most promising techniques. It is simple and low cost process.

This chapter presents the measurement results of the optical properties of TiO_x thin films. The variation of refractive index of thin films was measured through ellipsometry and modeling. The AFM was used for measuring the surface morphology and thicknesses of the films. Further study of X-ray diffraction was conducted to explore the crystalline nature of the films.

3. 2. Experiment

3.2.1. Thin films preparation

The TiO_x material is synthesized using sol-gel chemistry as described in chapter 2. P-type (1 0 0), 1 ohm-cm silicon wafers were used as substrate. The Si wafer was dipped in buffered oxide etchant (BOE) for 10 minutes to remove the native silicon oxide layer. The TiO_x precursor solution was then spin-coated on the Si substrate in air. The sample was baked in air at 90 ℃ for 10 minutes. The precursor was converted to TiO_x by hydrolysis.

Annealing was carried out in a rapid thermal annealing (RTA) chamber to study the variation of optical properties under different annealing temperatures and environment. The samples were annealed under O_2 or forming gas (mixture of N_2 and 5.05% H_2) for 10 minutes at 400 ℃, 500 ℃ , 700 ℃ and 900 ℃.

3.2.2. Sample characterization

The measurement of a multi-wavelength refractive index was carried out using an ellipsometer at an angle of incidence of 70 °. Ellipsometer is an optical technique for the investigation of the dielectric properties of thin films. The reflection at a dielectric interface depends on the polarization of the light. The transmission of light through a transparent layer changes the phase of the incoming wave depending on the refractive index of the material. An ellipsometer measures the changes in the polarization state of light when it is reflected from a sample. Then the optical constants can be extracted. The ellipsometer used in this work is a Jobin Yvon UVISEL NIR Spectroscopic Phase Modulated Ellipsometer. The data was obtained from 350 nm to 800 nm.

The thickness of the spin coated films was also measured using AFM. AFM measures the height between substrate and the top of the TiO_x films.

The surface morphology of the films was investigated by Dimension Nanoscope 3100 AFM. AFM was set to non-contact scanning probe microscopy mode. Scanning of the sample surface was taken before and after annealing, and root mean square (RMS) surface roughness was calculated.

The structure and crystallinity of the films were determined by a Scintag automated XDS 2000 XRD system. The measurement was conducted at room temperature.

The reflectance of various TiO_x thin films on Si substrate was measured by Filmetrics Filmeasure tool Version 2.1.2.

3.3. Results and discussion

3.3.1. Optical constant

The optical constants of the TiO_x thin films layer are simulated with Bruggemann effective medium approximation [38,39,40]. A three layer films structure model was established in order to determine the optical constants of the films by ellipsometric method. The model consists of a Si substrate, a dense TiO_x layer and a 50 % TiO_x: 50 % void surface layer, as shown in Figure 3-1. The mixture of TiO_x and void layer simulates the surface roughness. This model has been widely used and it agrees well with the experimental data [38].

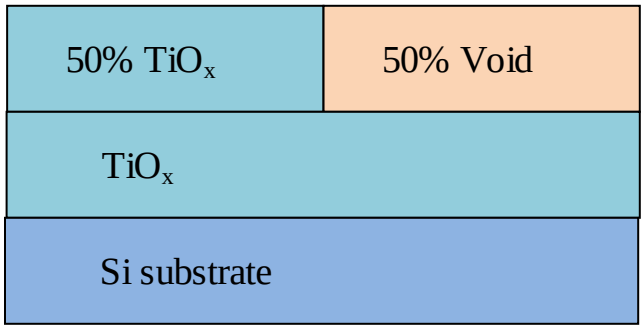

Figure 3-1: Three layers model of TiO_x films [41]

The dispersion model used to describe the TiO_x material is based on the original Forouhi-Bloomer formula [42]. This formula is consistent with the Kramers–Kronig analysis, which works well for a broad wavelength range. In this work, we calculated the optical constants in the visible range (from 350 nm to 800 nm) using equation (3-1).

$$n = n_\infty + \frac{B(\omega-\omega_0)+C}{(\omega-\omega_0)^2+\Gamma^2}\ ,\quad k(\omega)=\begin{cases}0,(\omega\le\omega_g)\\ \dfrac{f(\omega-\omega_0)^2}{(\omega-\omega_0)^2+\Gamma^2},(\omega>\omega_g)\end{cases} \qquad (3\text{-}1)$$

where $B=\dfrac{f}{\Gamma}(\Gamma^2-(\omega-\omega_g)^2)$, $C=2\Gamma f(\omega-\omega_g)$.

n_∞ is a constant greater than 1. The value depends on particular material [43].ω is the photon energy. ω_g is the optical gap energy. ω_0 is the bonding–antibonding states energy difference, the absorption is assumed to be maximum for this photon energy. The quantity f is related to the position matrix element and lifetime of the electrons involved in the optical transitions. Γ is related to the life time of the electrons involved in the optical transitions. B and C are not mere fitting parameters, but are related to electronic structure of the material. Detailed explanation of these parameters can be found in reference [42].

All modeling of optical constants was performed using the Jobin Yvon DeltaPsi2 (DP2) software package. The calculated parameters from the model fitting of experimental data are shown in Table 3-1.

Table 3-1: Modeling parameters for refractive index simulation

Annealing condition /parameters	900 ℃ in O_2	700 ℃ in O_2	400 ℃ in O_2	As deposited	400 ℃ in forming gas	700 ℃ in forming gas	900 ℃ in forming gas
n_∞	2.3	2.30	2.21	1.65	2.16	2.10	2.03
ω_g (eV)	3.08	3.22	3.24	3.30	3.26	3.25	3.20

f	0.24	0.20	0.03	0.07	0.02	0.28	0.34
ω (eV)	3.98	3.91	3.55	4.55	3.63	4.28	4.20
Γ (eV)	0.39	0.36	0.13	0.41	0.16	0.65	0.54

Figure 3-2 (a) and 3-2 (b) show the measured refractive index changes when the sample is annealed in forming gas and O_2, respectively. The data show that the refractive index increases with the annealing temperature.

The annealing process increases the refractive index. The increase of the refractive index is due to complex changes of organic component removal, film density changes and changes due to crystalline phase and surface morphology.

The refractive index increases from 1.77 to 2.57 at a wavelength of 600 nm after annealing at 900 ℃. This is close to what was reported in publications for the TiO_2 films. After annealing at 700 ℃ and 900 ℃, the refractive index of samples annealed in O_2 is higher than the one annealed in forming gas.

The variation of extinction coefficient *k* with wavelength is shown in Figure 3-2 (c) and 3-2 (d) when TiO_x films are annealed at various temperatures in forming gas and O_2, respectively.

The annealing process increases the extinction coefficient. The as deposited TiO_x films prepared at room temperature contains short -Ti-O-Ti- structures within the film, leading to electron confinement and an electronic gap which is broader than for the infinite -Ti-O-Ti- entities within bulk TiO_2. TiO_2 in bulk anatase or rutile crystal phases exhibits a band gap of ~3.1 eV. The -Ti-O-Ti- structure develops into longer more organized structures as organic matter and water are removed from the film by thermal

annealing. In these annealed structures, electron confinement effects are reduced. Therefore the TiO_x shows a high extinction coefficient around 400 nm after annealing. The extinction coefficient is close to zero in most of the wavelength range from 350 nm to 800 nm.

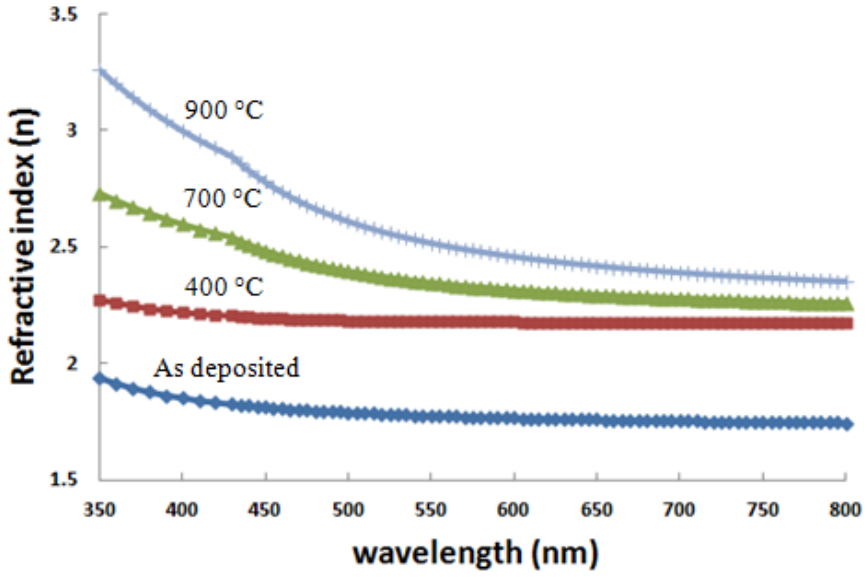

(a)

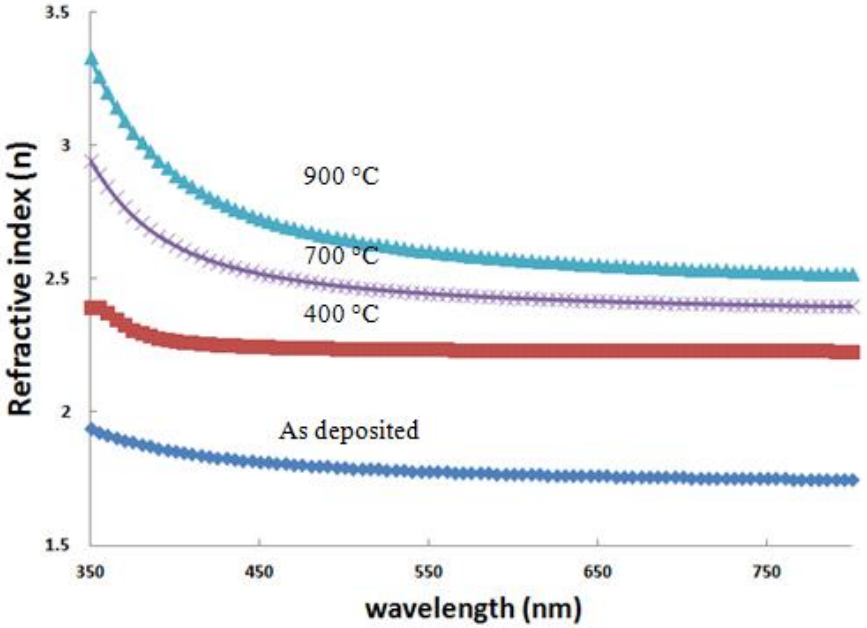

(b)

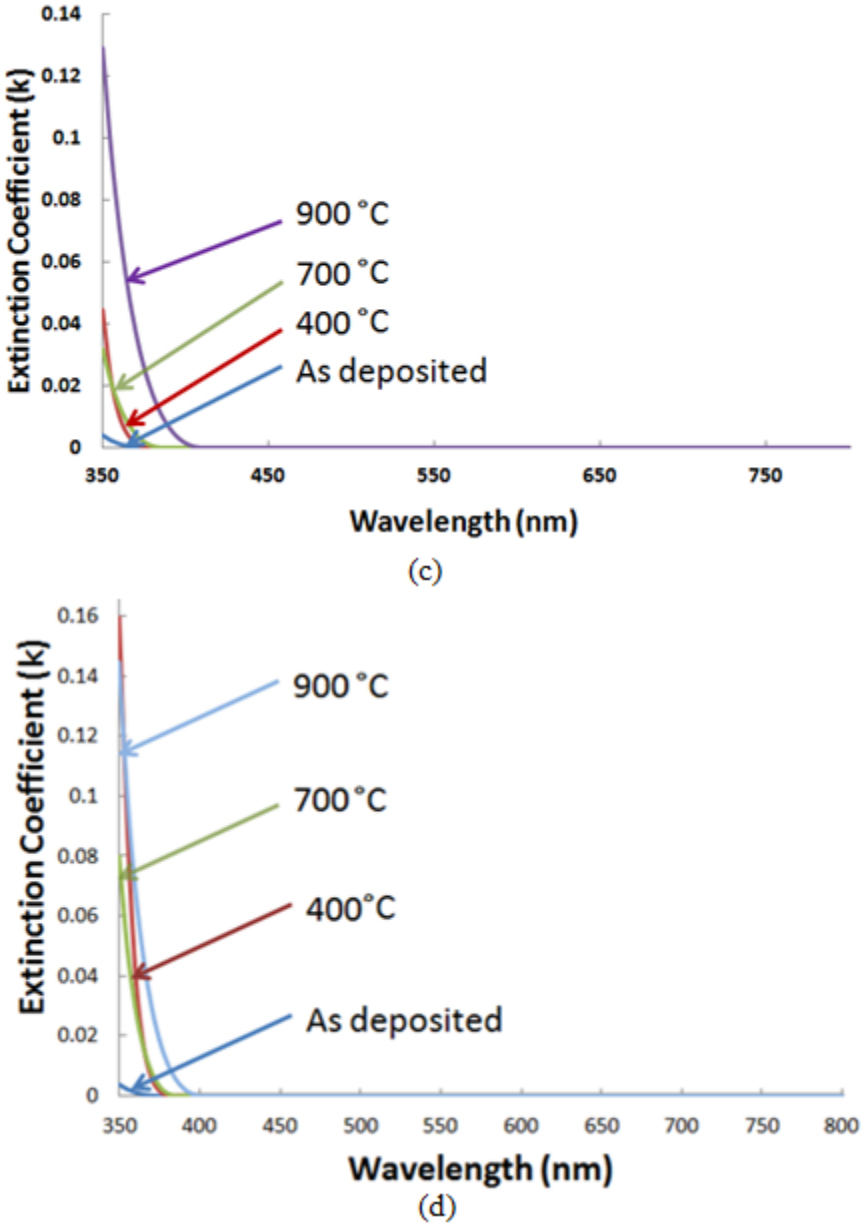

Figure 3-2: The variation of refractive index with wavelength when TiO_x films are annealed at various temperatures in (a) forming gas, (b) O_2 atmosphere, The variation of extinction coefficient (k) with wavelength when TiO_x films are annealed at various temperatures in (c) forming gas, (d) O_2 atmosphere[41]

3.3.2 Film thickness

It has been reported that there is a direct relationship between the refractive index and the density of the films [44]. Removal of the organic residue material and densification of the films occurs during the annealing process. The TiO_x films thickness is reduced after high temperature annealing. The layer thicknesses under different annealing conditions are listed in Table 3-2.

Table 3-2: Layer thickness at different thermal annealing conditions

Layer thickness (nm)	900 ℃ in O_2	700 ℃ in O_2	400 ℃ in O_2	As deposited	400 ℃ in forming gas	700 ℃ in forming gas	900 ℃ in forming gas
TiO_x	60	68	91	159	77	72	65
TiO_x/Void	2	1	1	1	1	1	5

3.3.3 Surface morphology

Surface morphology will affect optical constants due to the light reflection, absorption and scattering. Therefore changes of the surface morphology contribute to the variations in the effective refractive index. The surface morphology is studied by AFM.

Figure 3-3 (a) shows the surface morphology of as-deposited films obtained using AFM. The surface roughness of the bare silicon substrate is 0.24 nm. As deposited sample shows smooth surface with surface roughness of 1.5 nm which is evaluated from 10 μm × 10 μm surface areas. The surface becomes rougher after annealing, as indicated in Figures 3-3 (b) and 3-3 (c) , which show the surface morphology of samples annealed

in O_2 and forming gas at 900 ℃ for 10 minutes, respectively. The surface roughness increases to 2.5 nm.

It is noted that the surface roughness increases with the appearance of the crystalline phase by comparing with the crystalline phase change shown in Figure 3-4. Small grains can be observed on the surface by AFM. The morphology changes are due to the crystallization of TiO_x and densification of the films.

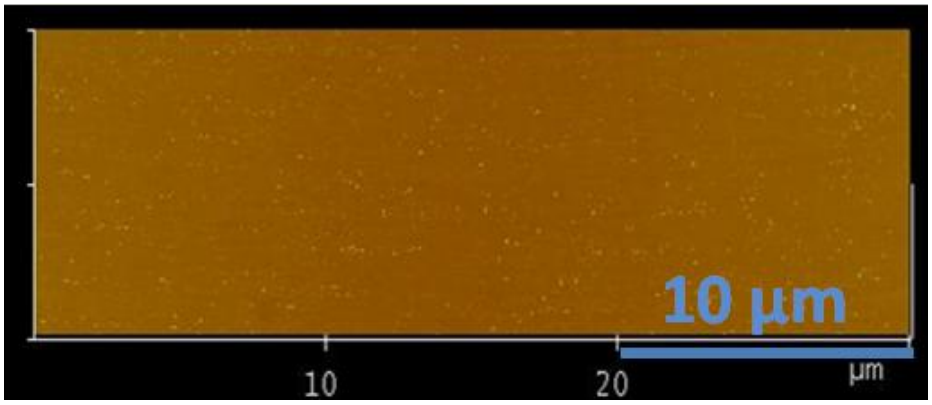

(a)

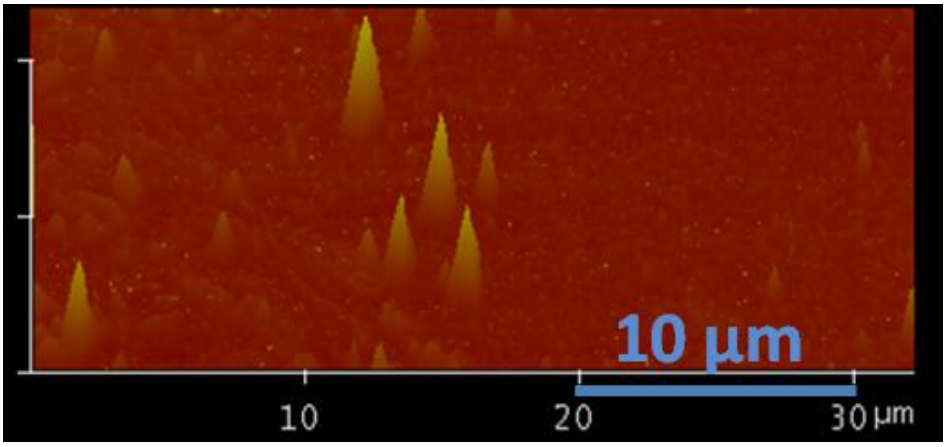

(b)

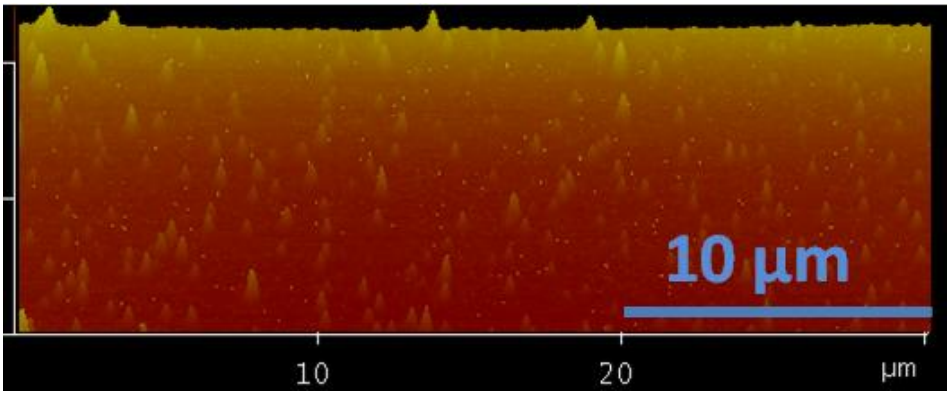

(c)

Figure 3-3: (a) AFM image of as deposited film (b) AFM image of film annealed in O_2 at 900 ℃ for 10 minutes (c) AFM image of film annealed in forming gas at 900 ℃ for 10 minutes[41]

3.3.4. Crystalline structure

Crystalline phase changes affect the refractive index. Crystallization occurs during the high temperature rapid thermal annealing process. Crystalline structure changes the refractive index. Rutile phase has different refractive index than anatase phase of TiO_2 [45]. The annealed films could be composed of amorphous, anatase and rutile structures. The results on phase changes after annealing process are discussed in this section.

Depositing TiO_x thin films onto substrates at low temperature leads to an amorphous structure. High temperature induces crystallization for the amorphous material. The titanium to oxygen ratio (Ti: O = 42.1: 56.4) indicates the sub-oxide characteristics of the as deposited TiO_x. Thermal annealing treatment promotes conversion of sub-oxide to dense crystalline structure. The effects of the thermal annealing on crystalline phase changes were examined.

The XRD results shown in Figure 3-4 indicate different phases of the films. The increase in annealing temperature could result in more observable crystalline phases. Figure 3-4 (a) and 3-4 (b) show the crystalline structure changes with temperature when annealed in forming gas and O_2, respectively. The as-deposited films show amorphous structure without any crystalline peak. The peaks at $2\theta = 33°$ and $2\theta = 70°$ are from Si substrate. They are the Si (1 0 0) and Si (4 0 0) peaks, respectively. The anatase (1 0 1) peak at $2\theta = 25.6°$ was observed at 500 ℃ when annealed in O_2. It indicates that crystalline structure appears in the film after annealing. No anatase peak was observed for the sample annealed at 500 ℃ in forming gas. The rutile (1 1 0) peak of TiO_2 material at $2\theta = 27.5°$ was observed after annealing in O_2 at 700 ℃. This peak corresponds to the rutile phase. The anatase phase peak disappears. It indicates that the films are transformed to a crystalline form with a rutile-dominant phase at high temperature. Anatase phase is a metastable phase at low temperatures. Therefore it is reasonable that the films were crystallized in a rutile-type structure at high temperature instead of the anatase-type structure. Similar rutile crystal structure was also clearly observed for the films annealed in forming gas at 900 ℃. It suggests that annealing in O_2 and forming gas will induce different Ti: O composition during the high temperature process. It is easier to form crystalline TiO_2 structure in rich oxygen environment.

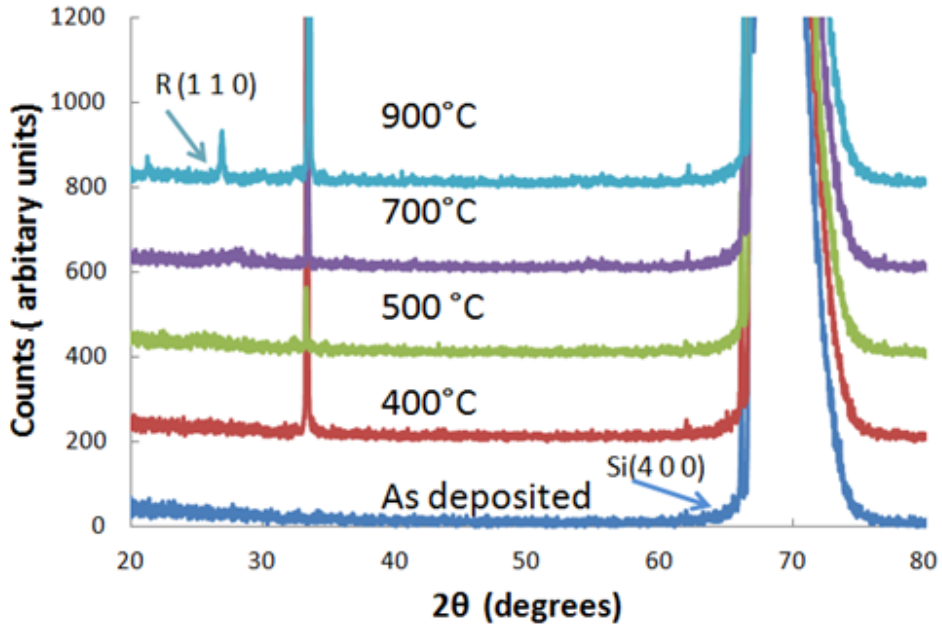

(a)

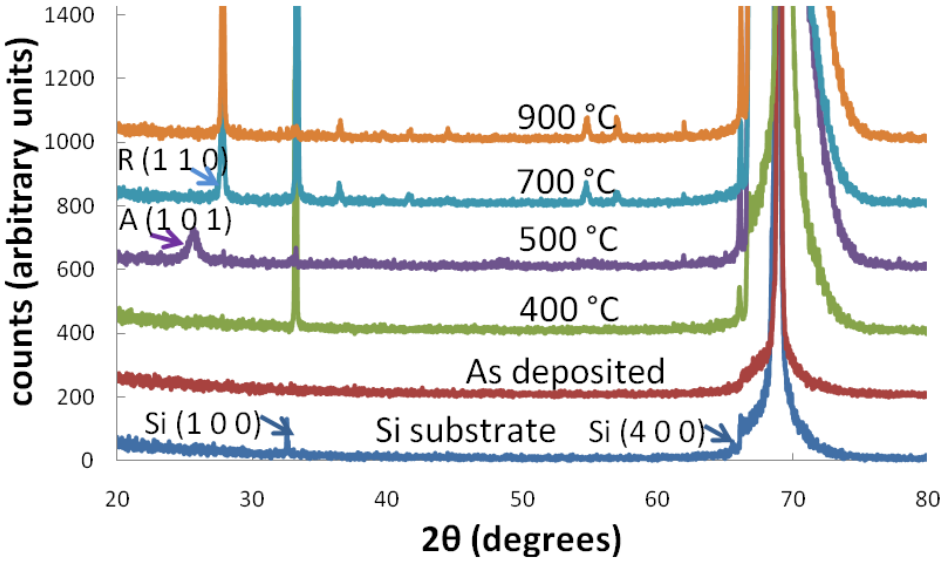

(b)

Figure 3-4: The XRD spectra for TiO_x films annealed in (a) forming gas and (b) O_2 at various temperatures of 400 ℃, 500 ℃, 700 ℃ and 900 ℃, respectively. R (1 1 0)

stands for the Rutile peak at 2θ = 27.5 °, A (1 0 1) stands for the Anatase peak at 2θ = 25.6 °[41]

The crystalline structure will affect the refractive index. At a wavelength of 600 nm, the mean refractive index is 2.70 and 2.53 for pure rutile and anatase crystalline structure, respectively. The TiO_x films after 700 ℃ and 900 ℃ contain anatase and rutile structures. The samples after annealing at 700 ℃ in O_2 and at 900 ℃ in forming gas show similar crystal structure and different refractive index.

3.3.5. Optical reflectance

The reflection of TiO_x film on silicon substrate can be tuned by changing the TiO_x overlay films thickness, annealing temperature and annealing gas. The variation of optical reflectance of TiO_x coated silicon with wavelength for different annealing conditions is shown in Figure 3-5, including as deposited TiO_x films, TiO_x films annealed in forming gas and in oxygen at 400 ℃.

Figure 3-5 shows that TiO_x material reduces the reflectance effectively compared with bare Si. Figure 3-5 also shows the reflectance comparison between TiO_x film and commonly used vacuum deposited Si_3N_4 film as an anti-reflection layer on Si. The optical reflection after annealing TiO_x films on Si at 400 ℃ in forming gas is very close to the Si_3N_4. This is considered as most optimized condition of thermal annealing for antireflection layer for silicon based devices. It indicates that such solution processable TiO_x material could be used as effective anti-reflection layer for Si based solar cells and other applications.

TiO_x forms uniform dense films though simple sol-gel hydrolysis process. The annealing process is also fully compatible with our Si solar cell fabrication process [46]. It

is a low cost substitution for the conventional thermal oxidation and vacuum process for TiO_2 deposition. Compared with other sol-gel TiO_2 material, TiO_x material could also effectively passivate the Si solar cell surface, as shown in chapter 10. Therefore TiO_x could be used for both as anti-reflection and passivation layer for Si solar cells instead of conventional high temperature thermally grown oxide and vacuum deposited Si_3N_4 layers.

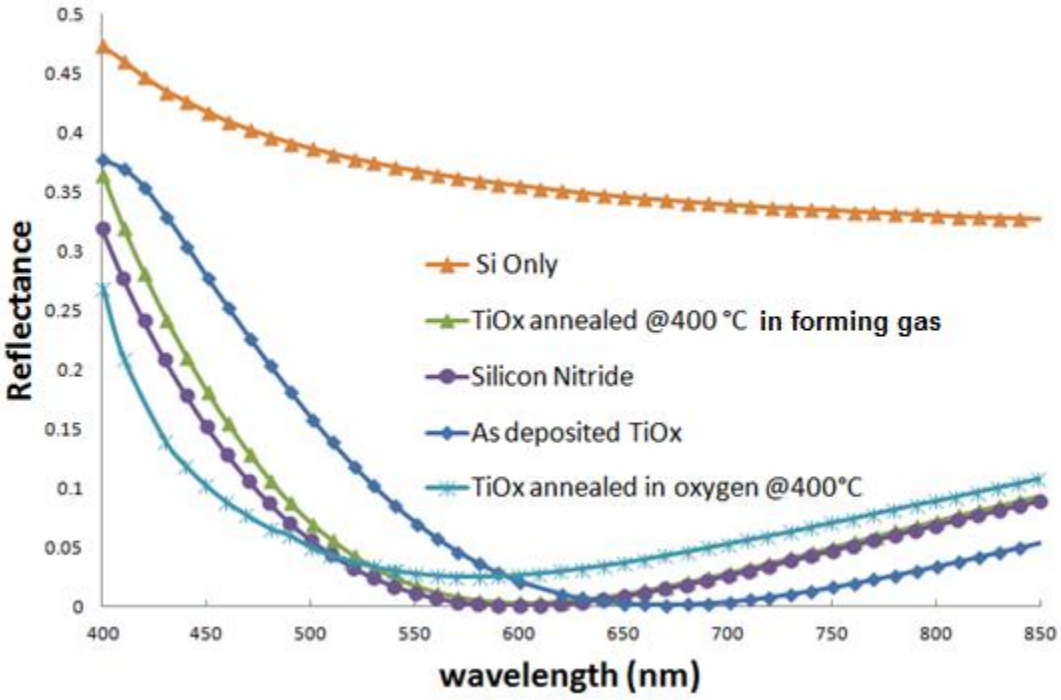

Figure 3-5: The measured optical reflectance from TiO_x thin films coated Si substrate for different thickness and annealing conditions, including as deposited TiO_x films before annealing, TiO_x films annealed in forming gas and in oxygen at 400 ℃. The reflectance from bare silicon and commonly used Si_3N_4 antireflection coating layer on Si are also shown. Si_3N_4 film thickness is 70 nm [41]

3. 4. Conclusions

In this chapter we presented optical constant measurement results obtained by ellipsometrical method for TiO_x thin films. Three layer modeling technique was used to

determine the refractive index and extinction coefficient of the thin films. At the wavelength of 600 nm, the obtained refractive index of the as-deposited films was 1.77. This value increased to 2.57 after annealing at higher temperature, which can be explained by the development of the crystalline structure, the difference of surface morphology and the increase of the packing density of the films as indicated by AFM and XRD results. The sol-gel TiO_x thin films may be used in optical thin film applications as antireflection layer.

Chapter 4. **Electrical resistivity of TiO_x thin films**

4.1. Introduction

Various groups have studied properties of TiO_2 thin films. For example, Asahi et al. calculated the electronic and optical properties of anatase TiO_2 thin films [47]. Pomoni et al. reported the electrical conductivity and photoconductivity of N-doped and undoped sol–gel TiO_2 thin films [48]. Sarah et al. reported electrical conductivity characteristics of TiO_2 thin films annealed at various temperatures [49]. Hassan et al. studied the structural and electrical properties of sol–gel derived spun TiO_2 thin films [50].

The uniform dense TiO_x thin films are semiconducting. The electron mobility is higher than that of amorphous oxide films prepared by typical sol–gel processes [6]. It is of interest to explore the electrical properties and other application of TiO_x thin films further.

In this chapter, we studied the electrical resistivity of TiO_x thin films material. Vertical transmission line measurement method was used to extract the TiO_x bulk resistance and contact resistance. The variation of electrical resistivity at ambient and different annealing temperature was also explored. Stable electrical resistance was observed at the temperature range from 20 ℃ to 140 ℃. The electrical resistivity decreased after high temperature annealing. The photoconductivity of TiO_x thin films was also studied.

4.2. Experiment

4.2.1. Device fabrication

The electrical resistivity measurement device structure used is shown in Figure 4-1(a). The Indium Tin Oxide (ITO) coated glass (Delta technology) was used as a substrate. The substrate was cleaned with acetone and isopropyl alcohol, and subsequently dried with nitrogen.

The TiO_x sol-gel solution in methanol was spin coated at various spin speeds onto an ITO coated glass substrate to achieve different film thicknesses. The coated sample was baked for 10 minutes at 80 ℃ in air, where the precursor converted to TiO_x through hydrolysis. Then a top aluminum electrode was deposited by electron beam evaporation in vacuum. The electrode was patterned through a shadow mask.

The thickness of the spin coated films was measured using a Veeco Dektak 8 stylus profilometer. Thickness was determined by the height between the top of the TiO_x film and the substrate.

To study the variation of electrical resistivity under different annealing temperatures, the heating was carried out in a rapid thermal annealing (RTA) chamber under O_2 for 2 minutes at various temperatures. The gas flow for O_2 was set to 100 standard cubic centimeters per minute (sccm). The TiO_x thin films, which had no heat treatment, are called as-deposited films.

When TiO_x thin films on ITO structure were annealed at temperature higher than 400 ℃, the films started peeling off due to thermal expansion difference between ITO and TiO_x. Therefore, a new device structure was designed for high-temperature annealing. The TiO_x thin films were spin coated on pre-cleaned quartz substrate. The sample was

annealed in RTA chamber at different temperatures. Then two Al pads with 20 μm separation distance were deposited above the TiO_x films, as shown in Figure 4-1 (b).

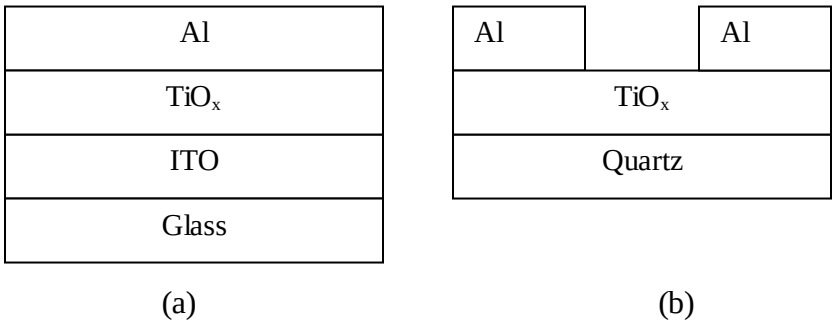

Figure 4-1: (a) ITO-TiO_x-Al device structure for vertical transmission line resistance measurement (b) Device structure to process sample at high- temperature annealing studies.

4.2.2 Electrical characterization

The electrical resistivity properties were measured through voltage-current measurements using a Keithley 2611 source meter.

Temperature-dependent measurements were made in a stainless steel vacuum chamber. The chamber was kept under nitrogen flow during the measurement. Samples inside the chamber were mounted onto a copper plate. The copper plate was in contact with a thermo-electric cooler that was used to heat and cool the samples. Temperature was controlled by varying the current supplied to the thermo-electric cooler. Temperature was monitored using a thermocouple inside the copper plate.

Data were taken through sequential temperature heating and cooling cycles: heating from 20 ℃ to 140 ℃, cooling from 140 ℃ to 20 ℃. Temperature was changed in 10 ℃ intervals, and data was recorded for each temperature. Temperature was held within ±1 ℃ for 5 minutes during each measurement.

The TiO_2 material is well-known for its photoconductivity properties. The measurements were made under room light conditions.

For the photoconductivity measurement, a 400W Dymax 5000-EC UV curing flood lamp system was use to illuminate the sample with structures shown in Figure 4-1 (b). UV light (power density = 200 mW/cm^2) illuminated the TiO_x thin films between the Al pads. The resistance was measured with Fluke mulitimeter.

4.3. Results and discussion

4.3.1 Electrical resistance measurement

The ITO-TiO_x-Al structure is expected to behave like a diode, which generally has series resistance (R_S) and shunt resistance (R_{SH}) associated with them. This is indicated in the equivalent circuit diagram shown in Figure 4-2.

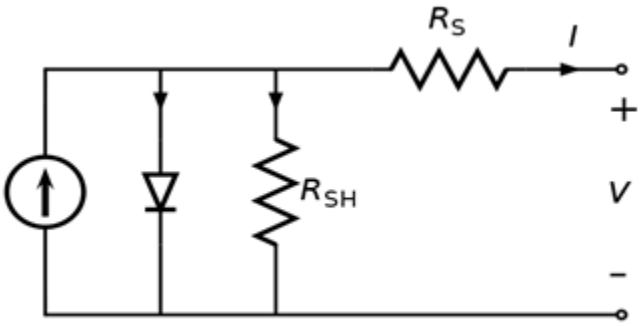

Figure 4-2: Schematic showing equivalent circuit for diode

A typical characteristic I-V curve of devices is shown in Figure 4-3 (a). It can be described by

$$I = I_0[e^{q(V-IR_s)/nkT} - 1] \quad (1)$$

where I_0 is the saturation current and n is the diode ideality factor. In the high current region, it can be written as [51]

$$I\frac{dV}{dI} = R_s I + \frac{nkT}{q} \tag{2}$$

Therefore, *I(dV/dI)* is linearly dependent on *I* with a slope equal to R_s in the high-current region. The series resistance can be extracted from the slope by a linear fit in the high-current region. *I(dV/dI)-I* characteristic curve of a diode is shown in Figure 4-3 (b).

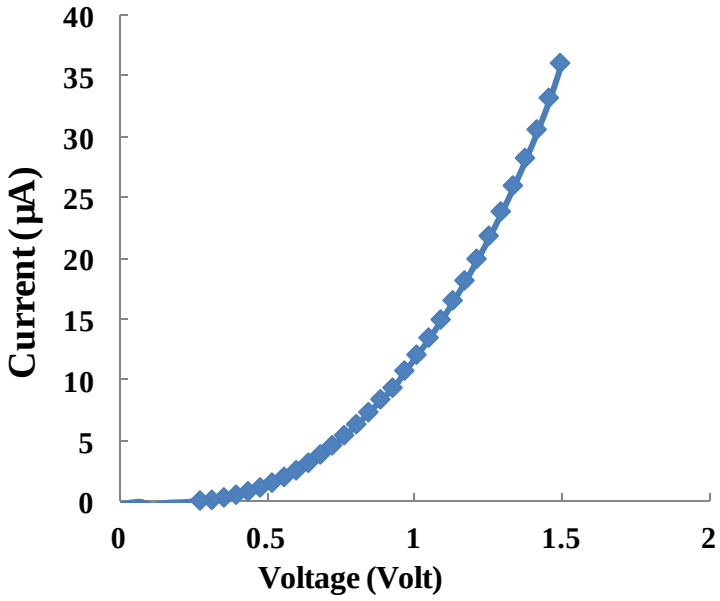

(a)

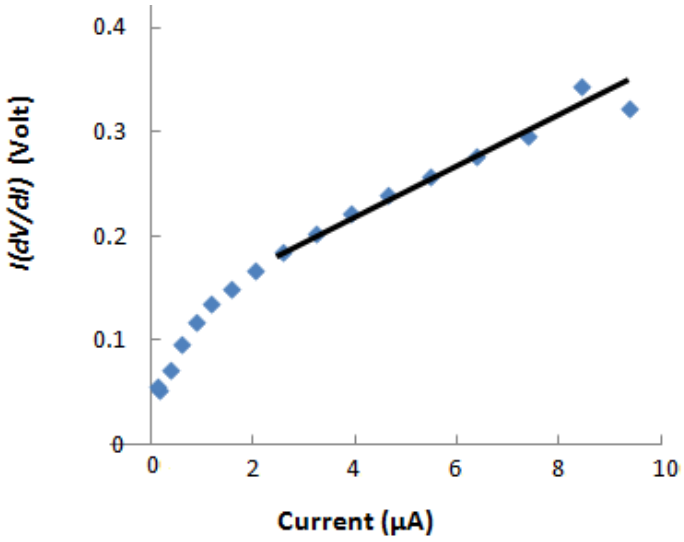

(b)

Figure 4-3: (a) Typical I-V curve for ITO-TiO_x-Al structure, (b) *I(dV/dI)-I* characteristic curve of the ITO-TiO_x-Al structure

Major contributors to the total series resistance are contact resistance between the ITO electrode and the TiO_x thin films, the bulk resistance of the TiO_x, contact resistance between the TiO_x thin films and Al electrode, and the bulk resistance of the Al contact. Al resistance is negligible because of the much lower resistivity of Al with respect to that of the TiO_x material. To extract the TiO_x films bulk resistance and contact resistance from total series resistance, we used vertical transmission line measurement model.

The transmission line measurement (TLM) method was originally proposed by Shockley [52] and offers a convenient method for determining contact resistance for planar contacts. The sheet resistance of the metallization is assumed to be zero. The total resistance R_{total} between any two contacts separated by a distance L could be measured and plotted as a function of L. The resulting equation between R_{total} and L provided an estimate of bulk resistance and contact resistance through the so-called transmission line equation

$$R_{total} = R_{bulk} + R_{contact} = \rho_{bulk} \times L + R_{contact}$$

where ρ_{bulk} is the specific resistivity of TiO_x thin films.

By fabricating devices with different TiO_x films thicknesses, the bulk resistance and contact resistance can be extracted.

Samples with different TiO_x thin films thicknesses were fabricated. Each sample had 8 individual devices. Each set of result is derived from the average of good devices on a single substrate. The R_{total} vs film thickness relation is shown in Figure 4-4.

From Figure 4-4, the total specific contact resistance of ITO-TiO_x, and TiO_x-Al interface was 30 Ω cm^2. For thin TiO_x films, the result indicates that the contact resistance is a major contributor to the total series resistance. The bulk resistivity of TiO_x was calculated as 1.5 ×10^7 Ω cm for the as-deposited films.

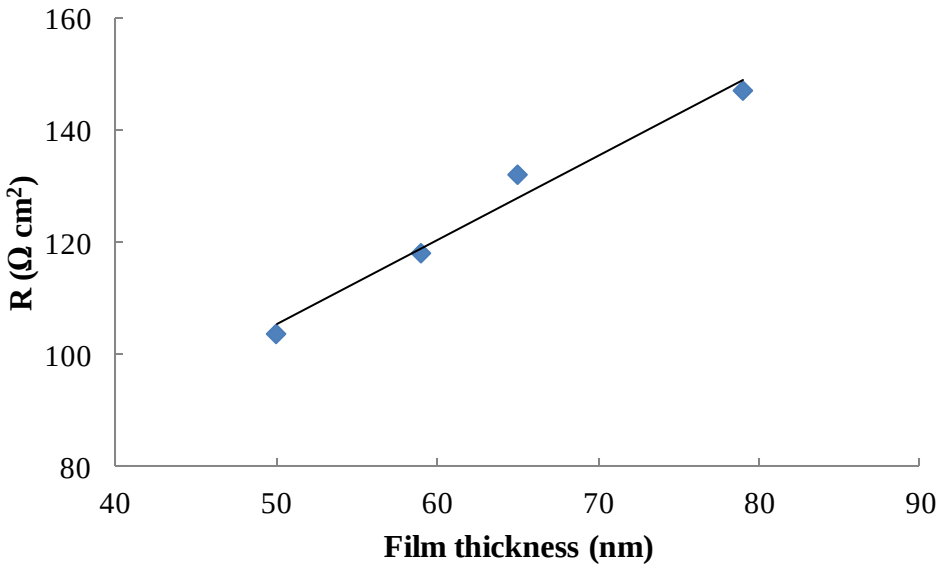

Figure 4-4: The variation of total resistance with TiO_x film thickness

4.3.2 Temperature ependence of electrical resistance

For TiO_2, band conduction is considered as the main charge transport mechanism at temperature higher than 220 K [48]. The free carriers in TiO_2 are due to stoichiometric deviations. The oxygen vacancies generates energy levels below the conduction band edge. The electrical resitivity of TiO_x films may change with temperature, because the energy supplied due to the heat will affect the carriers excitation in conduction band. We studied the resistivity of ITO-TiO_x-Al device structure from 20 ℃ to 140 ℃. Figure 4-5 shows the resistance measurement results for a device with 40 nm TiO_x film thickness.

There is no obvious changes for the electrical resistance of the ITO-TiO_x-Al structure from 20 ℃ to 140 ℃. It indicates that the heating has little effect for such ITO-TiO_x-Al structure.

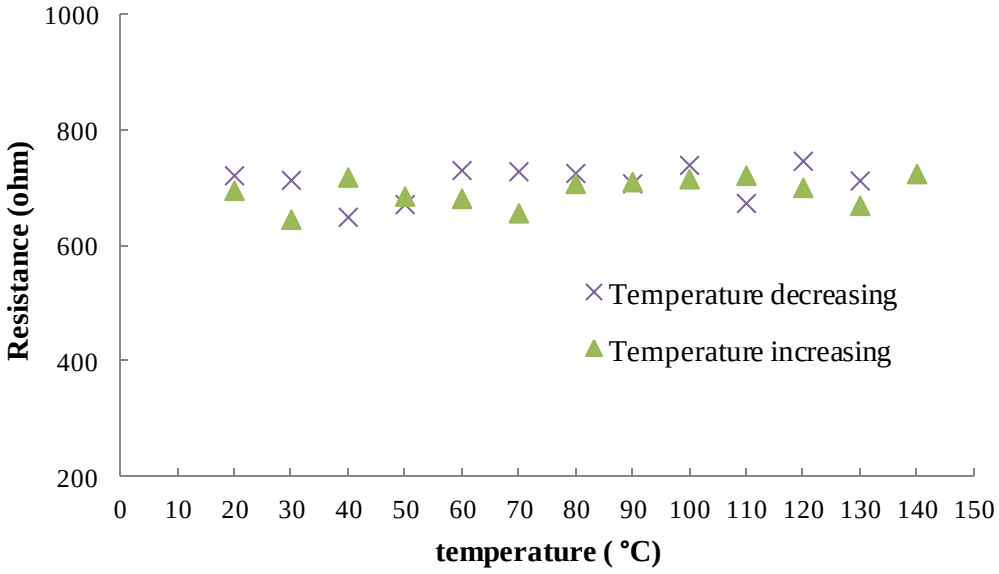

Figure 4-5: Electrical resistance of an ITO-TiO_x-Al device with 40 nm TiO_x thin films at the temperature ranging from 20 ℃ to 140 ℃

4.3.3 Electrical resistivity after thermal annealing

Thermal annealing has been shown to be a critical method for tuning organic material properties. The electrical resistivity is expected to change mainly due to the nonstoichiometric films composition and oxygen deficiency. As the annealing temperature increases, more oxygen vacancies are generated resulting in a sharp decrease in resistivity. Departures from stoichiometric TiO_2 will also change the resistivity dramatically，ranging from $< 10^{10}$ Ω cm for $TiO_{2.00}$ to 10^{-2} Ω cm for $TiO_{1.75}$ [53].

During the thermal annealing process, the residual organic materials were removed through oxidation and evaporation; therefore the films thickness reduced. The thickness reduced to 70 % after annealing at 300 ℃ for 20 minutes. The as-deposited TiO_x films are amorphous. There is a phase transition from amorphous to polycrystalline at high temperature. The anatase or rutile crystalline structure was observed after annealing at temperature higher than 500 ℃. The surface morphology, which will affect the contact resistance with electrode also changed after annealing [54].

The electrical resistivity changes after different thermal annealing temperature are shown in Figure 4-6. There are variations from sample to sample after annealing. The difference is due to the different composition, crystallinity, and oxygen vacancies concentration level in the samples. The lowest resistivity of 30 Ω cm is obtained after 700 ℃ annealing. The changes of chemical composition and oxygen vacancies level could be the main contributor for such large resistivity change.

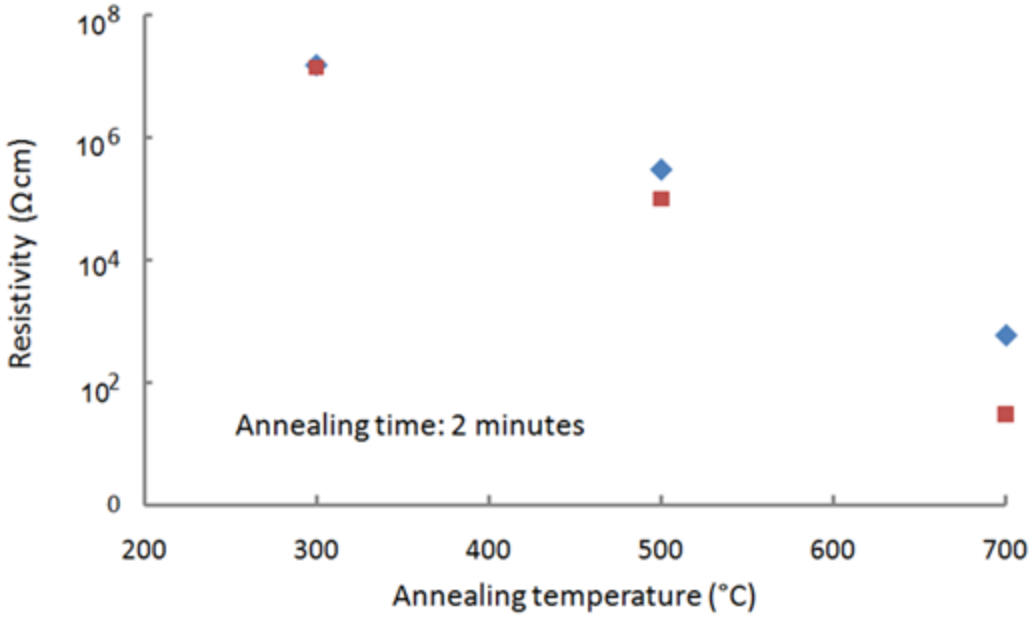

Figure 4-6: Electrical resistivity of TiO_x after different annealing temperatures. Different values at same temperature stands for different samples

4.3.4 Photoconductivty under UV illumination

There are photo-generated hole-electron pairs during UV illumination for typical crystalline TiO_2. Therefore the conductivity of TiO_2 films changes. We studied the photoconductivity response of TiO_x sample, as shown in Figure 4-7.

The resistance of the sample reduced from 3×10^6 Ω to 2×10^3 Ω under UV illumination after 40 seconds. It is due to the additional photo-generated carriers. When the UV light is off, the resistance recovers to the original value due to the recombination of the photo-generated carriers after 100 seconds. This recovery process is reproducible.

The sample is on a sample holder which is heated by UV exposure in the measurement. There is no such conductivity change when the UV light is blocked from

the sample. While the sample is still being heated. It indicates the change is not dominated by heating effects.

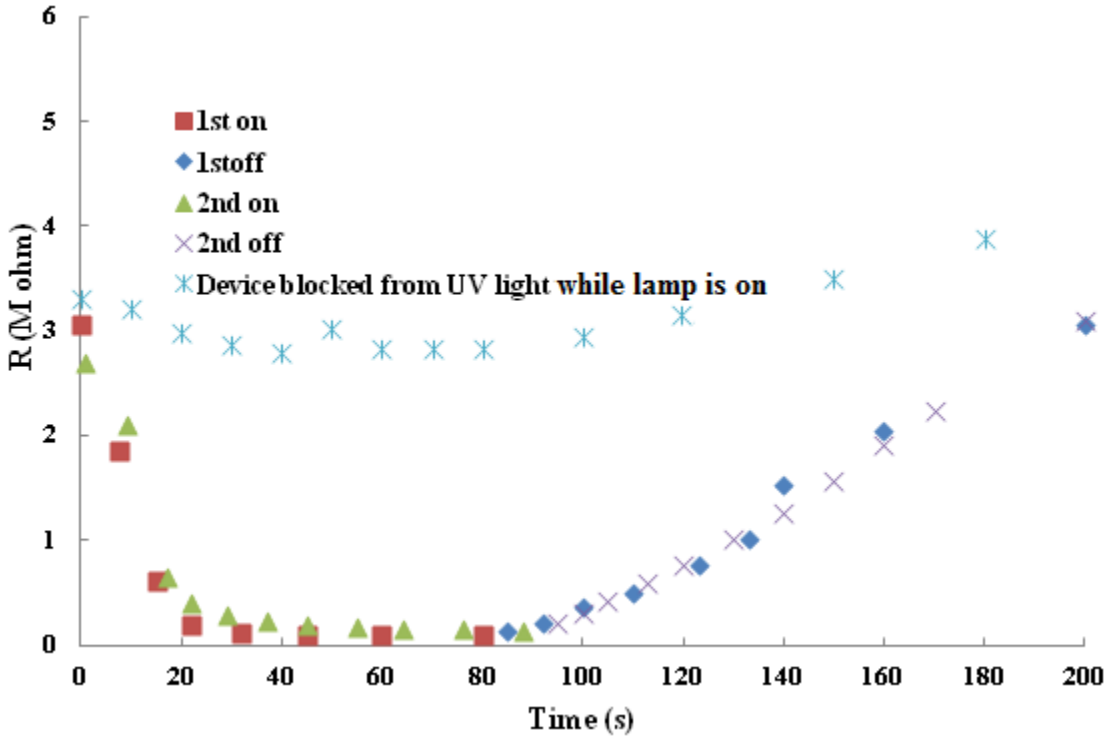

Figure 4-7: The photoconductivity response of TiO_x sample (annealed at 500 ℃) at room temperature in air

4.4. Conclusion

In this chapter, results about the electrical resistivity of TiO_x thin films are presented. ITO-TiO_x-Al device structure was fabricated to extract TiO_x bulk and contact resistance through vertical transmission line measurement model. The bulk resistivity of TiO_x film was found to be 4.7×10^7 Ω cm for the as-deposited sample. Current–voltage studies show that ITO-TiO_x-Al resistance is stable within the temperature range from 20 ℃ to 140 ℃. Thermal annealing increased the conductivity of the TiO_x thin films.

The resistivity of the TiO_x films reduces under UV illumination due to photo generated carriers.

Chapter 5. Organic solar cells: device physics, fabrication and characterization

5.1 Introduction

Organic solar cells have the potential to develop economical technology for large-scale power generation. Organic materials could produce very thin solar cells with low specific weight. They are also mechanically flexible. Much work on designing new materials, device structures and processing techniques has been carried out to improve the power conversion efficiency of such devices. Research on organic solar cells generally focuses either on solution processable organic semiconducting molecules/polymers or on vacuum-deposited small-molecular materials. Our research focuses on the solution processable fullerene/polymer devices.

In this chapter, we will first briefly review the development history of the polymer solar cells. The operation principles and characterization of the polymer solar cells will be introduced as well as the material system. Then we will describe the device structure and fabrication process of the polymer solar cells.

5.2 Development of polymer solar cells

In the 1980s the polymers (including poly (sulphur nitride) and polyacetylene) were investigated in solar cells. In 1982 Weinberger et al. [55] investigated polyacetylene as the active material in an Al/polyacetylene/graphite cell. The cell had a low open-circuit voltage of only 0.3 V and a low QE of only 0.3%. A major breakthrough came in 1986 when Tang discovered that bringing a donor and an acceptor together in one cell could

dramatically increase the power conversion efficiency to 1 % [56, 57]. Tang proposed the heterojunction structure.

The first report of a conducting polymer/fullerene cell, which is one of the most used donor/acceptors in heterojunction cells, came in 1993 by Sariciftci et al. [58] The cell had a relatively high fill factor of 0.48 and a PCE of 0.04 % under monochromatic illumination. The photocurrent increased more than 20 fold when C_{60} was added as a second layer. In 1994 Yu [59] made the first dispersed polymer heterojunction organic solar cell by spin-coating a solution of MEH-PPV and C_{60} in a 10:1 wt-ratio on ITO coated glass. Polymer/fullerene blends have been of particular interest since then. So far, polymer solar cells based on conjugated polymers as electron-donor materials blended with [6,6]-phenyl-C_{71}-butyric acid methyl ester ($PC_{71}BM$) as an electron-acceptor material have achieved ~10.6 % efficiency using tandem structure[60].

5.3 Operating principles

The process of conversion of light into electricity by an organic solar cell can be described by the following steps: (1) Light absorption, (2) Exciton diffusion, (3) Exciton dissociation, (4) Charge transport, (5) Charge collection.

(1) Light absorption

The photoexcitations in organic materials do not directly lead to free charge carriers but to coulombically bound electron-hole pairs, called excitons. The creation of an exciton after the absorption of a photon is the first step.

(2) Exciton diffusion

For efficient dissociation of excitons, strong electric fields are necessary. Such local fields can be supplied via donor/acceptor interfaces. At an interface, where abrupt changes of the potential energy occur, strong local electrical fields are possible. Excitons have to reach such an interface within its lifetime. Otherwise, excitons decay via radiative or nonradiative pathways. The exciton has a diffusion length related to the exciton lifetime and diffusion coefficient. Exciton diffusion lengths in polymers and in organic semiconductors are usually around 10-20 nm.

(3) Exciton dissociation

The exciton diffuses inside the material to reach the donor-acceptor interface. At the donor/acceptor interface, due to the different electron affinity of two materials, the electron will be acquired by the one with higher electron affinity, which is the acceptor. Blending conjugated polymers with fullerenes is a very efficient way to break apart photo-excited excitons into free charge carriers. The photo induced charge transfer in such blends happens on a time scale much faster than other competing relaxation processes.

(4) Charge transportation

A gradient in the chemical potentials of electrons and holes is built up in a donor-acceptor junction. It contributes to a field-induced drift of charge carriers. Asymmetrical contacts (one low work-function metal for the collection of electrons and one high work-function metal for the collection of the holes) also lead to an external field. This field will drive charge carriers to reach the electrodes.

(5) Charge collection

As a last step, charge carriers are extracted from the device through two selective contacts. A transparent indium tin oxide (ITO) matches the highest occupied molecular orbital (HOMO) levels of most of the conjugated polymers. Al contact with a work function of around 4.3 eV matches the lowest unoccupied molecular orbital (LUMO) of acceptor PCBM (electron contact) on the other side. There is carrier recombination at the active layer/ electrode interface. Therefore, additional layer that could block certain carriers would enhance the efficiency. PEDOT: PSS layer was usually put on top of ITO layer as electron blocking layer. TiO_x layer also works as hole blocking layer.

The operation mechanism is shown in the Figure 5-1.

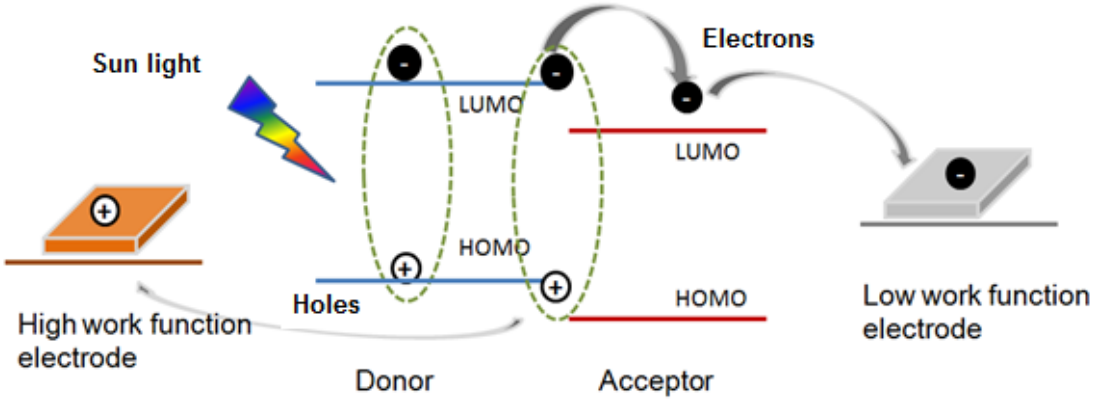

Figure 5-1: Operation mechanism of polymer organic solar cells.

5.4 Materials

Acceptors

C_{60} has a high electron affinity. It is fairly transparent and also has fair electron conductance (10^{-4} Scm^{-1}). This makes fullerenes a good component in organic solar cells. The solubility of simple C_{60} is limited. Wudl et al.synthesized a soluble derivative of C_{60},

$PC_{61}BM$ (1-(3-methoxycarbonyl) propyl-1-phenyl [6, 6] C_{61}) [61], which has been widely used in polymer/fullerene solar cells due to its solubility. [6,6]-phenyl-C71-butyric acid methyl ester ($PC_{71}BM$) has also been used recently for its higher absorption than $PC_{61}BM$. In our experiment, we use $PC_{61}BM$ as the acceptor. The molecular structure of $PC_{61}BM$ is shown in Figure 5-2. The $PC_{61}BM$ material was purchased from NanoC Inc. It was used as purchased.

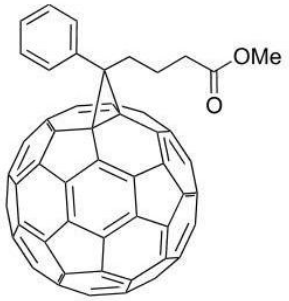

PCBM

Figure 5-2: Chemical structure of PCBM

Donors

Conjugated polymer materials have a delocalized π electron system. They have a high extinction coefficient (> 10^5 cm^{-1}), which makes it possible for sufficient light absorption with thin films (<100 nm). They can be modified to have a small optical band gap, which allows them to absorb most of the solar spectrum. Some important representatives of hole conducting donor-type polymers includes (1) derivatives of phenylene vinylene backbones such as poly[2-methoxy-5-(3,7-dimethyloctyloxy)]-1,4-phenylenevinylene) (MDMOPPV), (2) derivatives of thiophene chains such as poly(3-hexylthiophene) (P3HT), and poly[[9-(1-octylnonyl)-9H-carbazole-2,7-diyl]-2,5-thiophenediyl-2,1,3-

benzothiadiazole-4,7-diyl-2,5-thiophenediyl] (PCDTBT). In our experiment, we use P3HT as the donor. The molecular structure of P3HT is shown in Figure 5-3. The P3HT material was purchased from Sigma Aldrich Corp. It was used as purchased.

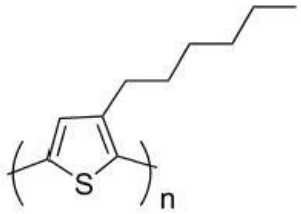

P3HT

Figure 5-3: Chemical structure of P3HT

Hole transporting layer

Poly (3,4-ethylenedioxylenethiophene):polystyrene sulfonic acid (PEDOT:PSS) is a polymer mixture of two ionomers. It is used as a transparent, conductive polymer with high ductility in different applications. Highly conducting PEDOT: PSS was purchased from H .C. Stark with a conductivity of 1×10^{-3} S/cm. PEDOT: PSS with a work function of around 5.0 eV can effectively block the transportation of electrons to the ITO electrode.

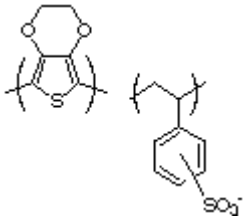

Figure 5-4: Chemical structure of PEDOT: PSS

Electrodes

A transparent ITO, with a work function of 4.8 eV, matches the highest occupied molecular orbital (HOMO) levels of most of the conjugated polymers. Therefore it is usually used as hole collecting electrodes.

Al with a work function of around 4.3 eV matches the lowest unoccupied molecular orbital (LUMO) of acceptor PCBM on the electron collection side. Ag electrode could also be used for electron extraction contacts. The device with Ag electrode is more stable than the one with Al electrode but it is expensive.

5.5 Device structure

The organic solar cells in this dissertation are based on the P3HT and PCBM material system. The organic solar cell device structure and band diagram used in this study are shown in Figure 5-5.

The absorbing and charge-separating bulk-heterojunction layer is sandwiched between the ITO electrode for collecting the holes and Al electrode for collecting the electrons. The work-function difference between electrodes and different electron affinity of P3HT and PCBM provide driving force for the photogenerated carriers toward their respective electrodes. The PEDOT: PSS layer is the electron blocking layer.

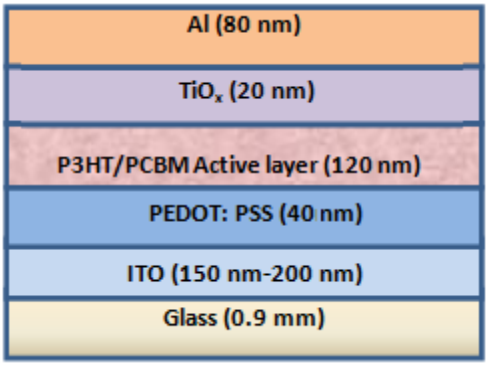

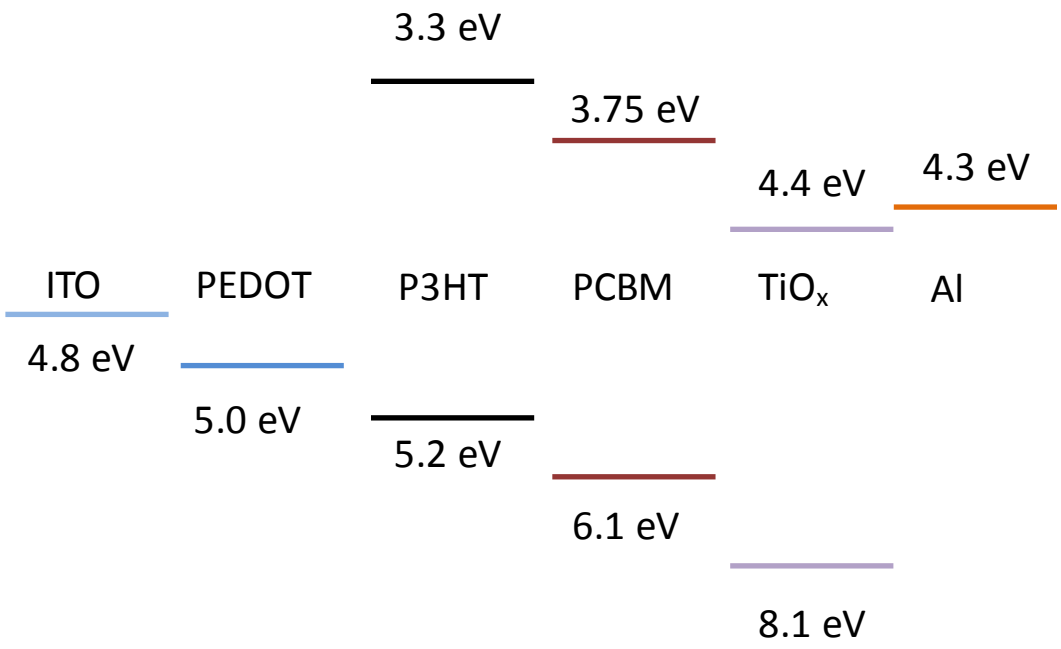

Figure 5-5: Organic solar cell device structure and band diagram

Compared with normal organic solar cell device, the organic solar cell studied in this dissertation uses additional optical spacer layer. There are optical interference between the incident and back-reflected light from the metallic electrode. The intensity of the light is zero at the metallic electrode and active layer. Thus, a large fraction of the active layer is in a dead-zone at the metallic electrode side. The photo generation of carriers is significantly reduced due to lack of light absorption for thin active layer.

Introducing an optical spacer between the active layer and the Al electrode changes the spatially redistributing the light intensity inside the device, as shown in Figure 5-6.

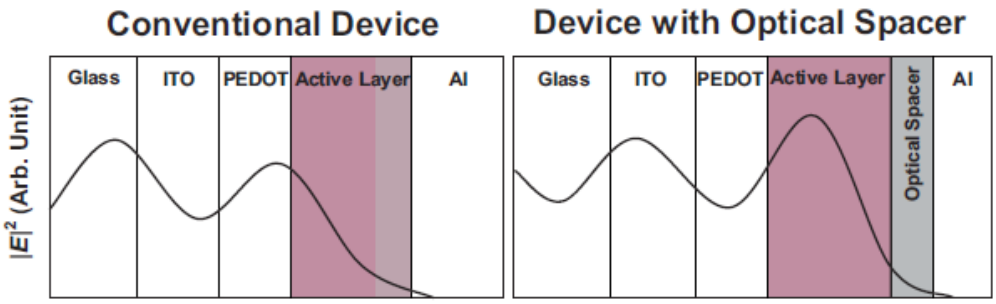

Figure 5-6: Schematic representation of the spatial distribution of the squared optical electricfield strength $|E|^2$ inside the devices with a structure of ITO/PEDOT/active layer/Al (left) and ITO/PEDOT/active layer/optical spacer/Al (right). From J. Y. Kim [6]

The optical spacer material should satisfy optical and electrical requirements to function as a good optical spacer. The material must be non-absorbing within the solar spectrum. The material must be an electron-transport material. The conduction band edge of the material must match the C_{60} and metallic electrode. TiO_x material and zinc oxide nanoparticles have also been shown to fulfill these requirements.

TiO_x layer is multi-functional layer in the organic solar cells. It is optical spacer, protection layer, hole blocking and electron transporting layer.

5.7 Fabrication of organic solar cells

The ITO coated glass was used as a substrate and cleaned with acetone and isopropyl alcohol and subsequently dried in nitrogen.

PEDOT: PSS was spin coated at 4000 rpm onto an ITO coated glass substrate to achieve a thickness of 40 nm. The substrate was baked for 15 minutes at 110 ℃ in air.

The P3HT material was purchased from Sigma Aldrich Corp and PCBM from NanoC Inc. They were dissolved in dichlorobenzene solution of 0.45 and 0.55 wt % respectively.

The solution was spin coated on an ITO coated glass substrate to produce a film of 120 nm thickness. The films were prebaked at 60 °C for 30 minutes in vacuum.

The TiO_x sol-gel precursor, dissolved to 2 % by volume in methanol, was spin-coated on the top of the active layer. Subsequently, the precursor converted to TiO_x by hydrolysis after 10 minutes baking in air at 90 °C. The resulting ~25 nm TiO_x film was transparent and smooth. Since the TiO_x layer was deposited at room temperature and treated at 90 °C, the film was amorphous.

Subsequently the device was put in vacuum chamber (< 10^{-6} torr), and 80 nm Al electrode was deposited by e-beam evaporation. The Al electrode area defined the active area of the devices.

The samples were post baked at 130 °C in air for 2 minutes before measurements of solar cell efficiency. Thermal annealing increased the crystallinty of the P3HT. The mobility of holes increased. Thermal annealing also improved the Al/active layer interaction, which helped to reduce the contact resistance.

The entire fabrication process is shown in Figure 5-7.

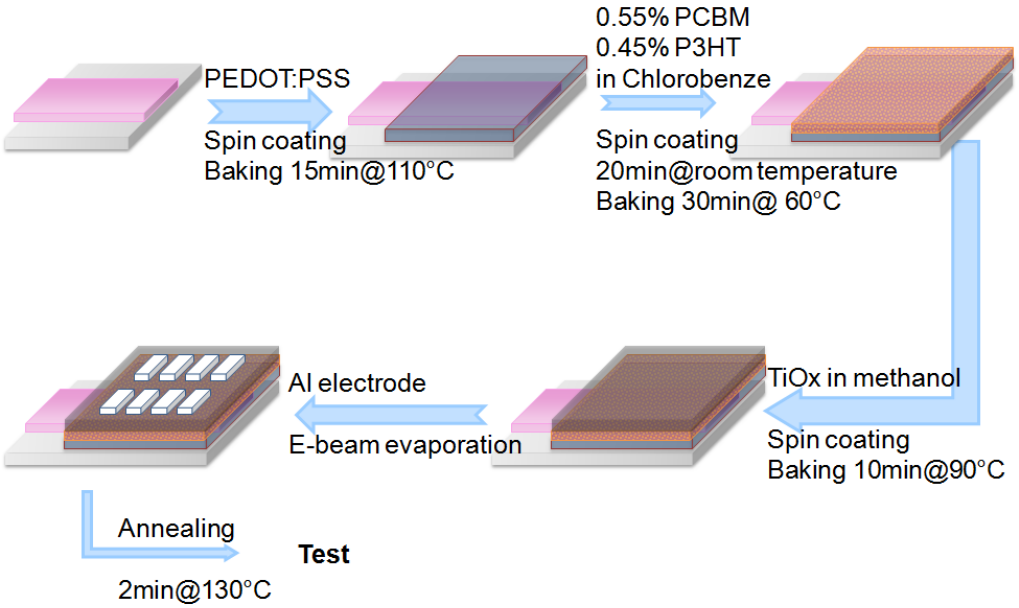

Figure 5-7: Fabrication process of organic solar cells in our experiment

5.6 Organic solar cell characterizations

Figure 5-8 (a) shows the experiment set up for characterization of the organic solar cells in this dissertation. The typical current-voltage characteristic of a solar cell under illumination is shown in Figure 5-8 (b). The parameters are described as follow.

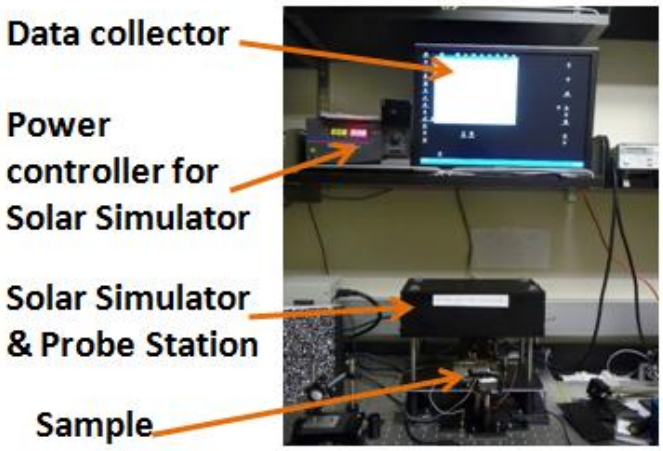

(a)

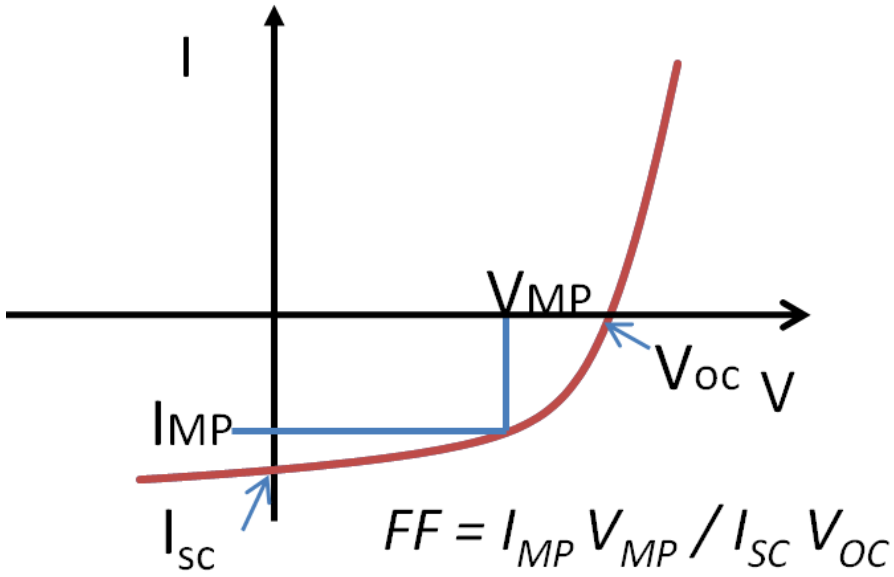

(b)

Figure 5-8: (a) the experiment set up for characterization of the organic solar cells in this dissertation. (b) Current-voltage (I-V) curves of an organic solar cell. the maximum current density and voltage defined as I_{MP} and V_{MP}. V_{oc} is open circuit voltage, I_{sc} is short circuit current. FF is fill factor

Open circuit voltage (V_{oc})

When the output contacts are isolated, the potential difference has its maximum value, the open circuit voltage V_{oc}. The operating regime of the solar cell is the range of bias, from 0 to V_{oc}, in which the cell delivers power. The open circuit voltage of this type of donor/acceptor bulk-heterojunction cell is related directly to the energy difference between the HOMO level of the donor and the LUMO level of the acceptor components. The variation of the negative electrode work function also influences the open circuit voltage. [62]

Short circuit current (I_{sc})

The short circuit current corresponds to the short circuit condition when the voltage across the device equals 0. I_{sc} occurs at the beginning of the forward-bias sweep and is the maximum current value in the power quadrant. In an ideal solar cell, which has loss free contacts, this maximum current value is the total current produced in the solar cell by photon excitation. It is determined by the product of the photo generated charge carrier density and the charge carrier mobility within the active layer. The bottlenecks of I_{sc} are the absorption of the material for active layer and the mobility of charge carriers.

Fill factor (FF)

The Fill factor is essentially a measure of quality of the solar cell. It is calculated by comparing the maximum power to the theoretical power that would be output at both the open circuit voltage and short circuit current together. A larger fill factor is desirable, and corresponds to an I-V curve that is more square-like. Physically, fill factor is determined by charge carriers reaching the electrodes. The series resistances influence the filling factor considerably and should be minimized. Fill factor is calculated as

$$\mathrm{FF} = \frac{\mathrm{I}_{MP} \times V_{MP}}{I_{sc} \times V_{oc}}$$

where the maximum power output point is defined as P_{MAX}, and the maximum current density and voltage defined as I_{MP} and V_{MP}, as shown in Figure 5-5.

Power conversion efficiency (η)

Power conversion efficiency represents the ability of the cell to convert light into electricity. Efficiency is defined as the ratio of the electrical power output, compared to the incident solar power.

$$\eta = \frac{V_{oc} \times I_{sc} \times FF}{P_{in}}$$

These four quantities: I_{sc}, V_{oc}, FF and η are the key performance characteristics of a solar cell. All of them should be defined for particular illumination condition. The standard test condition for solar cells is the air mass 1.5 spectrum, an incident power density of 100 mW cm^{-2}, and a temperature of 25 ℃.

5.7 Conclusion

In this chapter, we reviewed the development of polymer based organic solar cells. The operation principles from light absorption to free charge collection in the donor/acceptor organic solar cells were introduced. The device structure and fabrication technique used in this dissertation were described in detail.

Chapter 6. Stabilization of P3HT/PCBM organic solar cells by photochemical active TiO_x layer

6.1. Introduction

This chapter discusses the long-term stability of regioregular P3HT/ $PC_{61}BM$ based organic solar cells under ultraviolet (UV) and environmental degradation conditions.

Degradation of organic solar cells has been investigated by several groups and is considered a complex phenomenon. The degradation process involves several mechanisms, such as water absorption by a PEDOT: PSS layer, reaction of the metal/organic interface and oxidation of the organic layer [63,64, 65,66]. Lira-cantu et al. [67] studied the incorporation and transport of oxygen using combination of isotopic labeling and time of flight secondary ion mass spectrometry. Norrman et al. [68] found that water effect was found to be similar the effect of molecular oxygen by studying water-induced degradation of polymer solar cells using H_2 ^{18}O labeling. The results on the stability for roll-to-roll process for flexible polymer solar cells have also been reported [69]. However, further studies are needed to address the issue of long-term stability of organic solar cells.

Different approaches to achieve higher stability have been considered including use of improved active materials and encapsulation schemes. Hauch et al. [70] showed that flexible P3HT: PCBM bulk heterojunction solar cell modules with more than 1 year outdoor lifetime by packaging with transparent barrier films. Lee et al. reported enhanced environmental stability for P3HT/PCBM-based organic solar cells using a TiO_x layer on

top of the organic active layer [4]. Cho et al. demonstrated improvements in field effect transistor device lifetime by TiO_x layer [5]. TiO_x is postulated to block the passage of oxygen and humidity into the organic active layer. The mechanism proposed is based on oxygen deficiencies in the TiO_x films providing adsorption sites for O_2 [71].

The TiO_x layer contains both Ti-OR (OR=alkoxide) functionalities and Ti-OH groups. Under UV irradiation, the Ti-OR functionalities are photo oxidized, consuming O_2 and generating CO_2, H_2O gas products and [HCOO-] and Ti-OH moieties. The role of the photoexcitation of TiO_x layers was not postulated in previous works. This is another possible protection mechanism that forms the basis for TiO_x films to remove oxygen when exposed to ultraviolet light.

In this chapter we studied the individual effect of oxygen and UV radiation as well as the combined effect on the degradation behavior of P3HT/PCBM organic solar cell devices. The improvements provided by placing TiO_x layer between the active layer and Al electrode were examined. IR and ESR spectroscopy measurements showed that the improvements were due to photo-oxidation of the bound organic moieties causing oxygen gas scavenging.

6.2. Experimental

The organic solar cell device structure was based on the P3HT and PCBM material system. The organic solar cell device structure used in this study is shown in Figure 6-1.

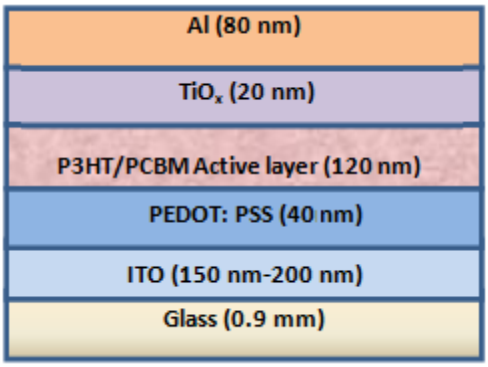

Figure 6-1: Organic solar cell device structure [72]

The TiO_x material was described previously and was provided by Heeger's group at UC Santa Barbara. The device fabrication method and process parameters used are shown in Figure 6-2.

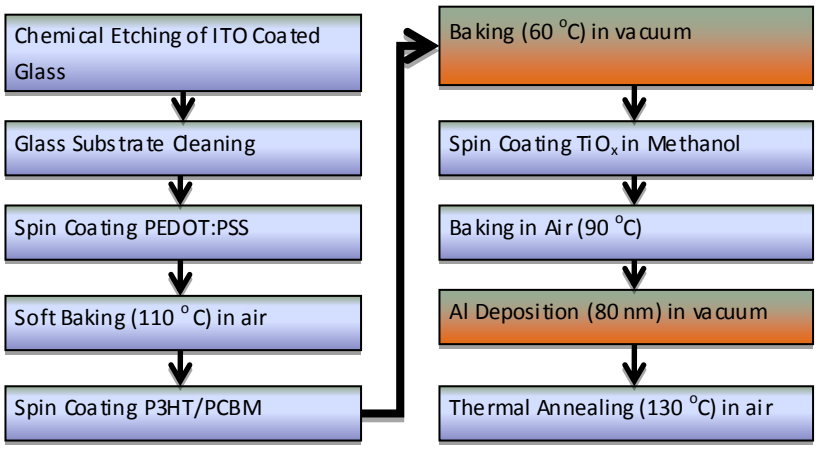

Figure 6-2: Organic solar cell fabrication process: Color coded for process in air (purple) and process in vacuum (orange) [72]

The photovoltaic cell performance was measured under AM 1.5 illumination using a calibrated solar simulator with irradiation intensity of 100 mW cm^{-2}. The solar cell size was around 0.12 cm^2. Efficiencies were 2.8% and 2% for the device with TiO_x and without TiO_x, respectively in air. The initial photovoltaic characterization parameters

are listed in Table 6-1. Three types of ambient conditions were used for this study that included air, oxygen and dry N_2 atmospheres. All experiments were carried out at room temperature.

Table 6-1: Initial photovoltaic characterization parameters

	Efficiency (%)	V_{oc} (V)	J_{sc} (mA/cm^2)	Fill Factor
Device without TiO_x	2	0.67	5.1	54
Device with TiO_x	2.8	0.64	7.2	57

All the devices without TiO_x protection have been found to degrade to lower than 80% of initial efficiency during 12 hours. Therefore 12 hours time is long enough to study the degradation according to the recommended procedures for reporting organic solar cell stability [73]. Each set of data is derived from the average of 8 devices on a single substrate. We can clearly see the degradation trend and improvement that could be achieved by TiO_x.

A 500 W Oriel 66033 Hg arc lamp was used in the UV light exposure studies. The radiation from the lamp was filtered with a Thorlab FGUV11S square colored glass UV filter to remove IR radiation. The lamp spectrum, compared well with solar spectrum and the transmission property of the filter is shown in Figure 6-3.

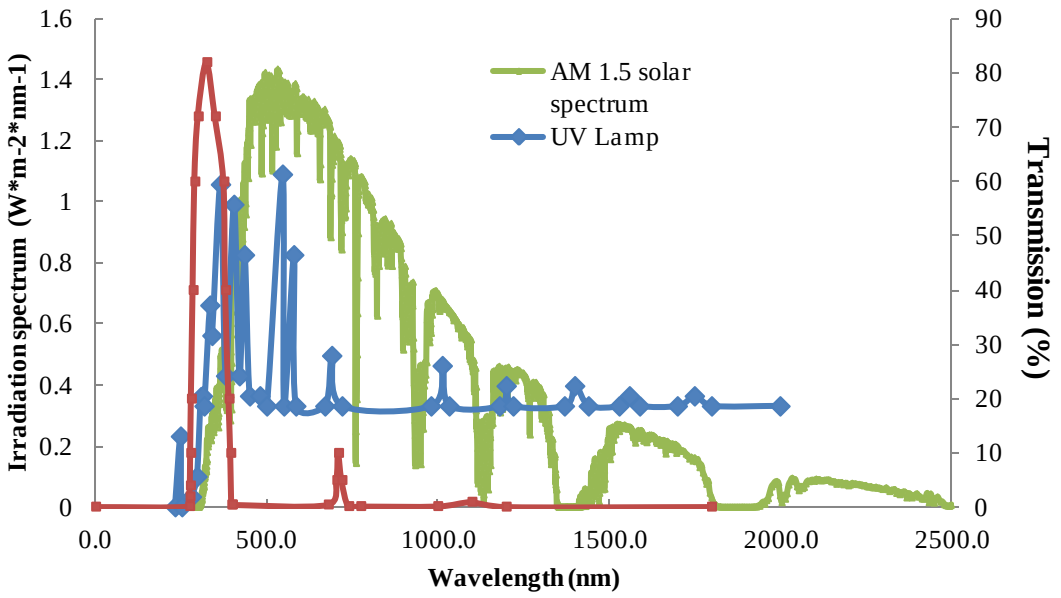

Figure 6-3 500 W Hg UV lamp spectrum, AM 1.5 solar spectrum and transmission of FGUV11S band pass filter [72]

Experiment set up for UV irradiation was shown in Figure 6-4. The lamp was held at 50 cm from the sample mounted inside the chamber and an aperture was used to limit the beam size. The solar cell samples were irradiated continuously except during few minutes of the measurement time. No heating of the samples was observed. The intensity of light incident on the sample was varied through changing the distance from light source to sample. The UV power density was measured using a Thorlab D3MM bolometer and was kept at 10 mW cm^{-2}.

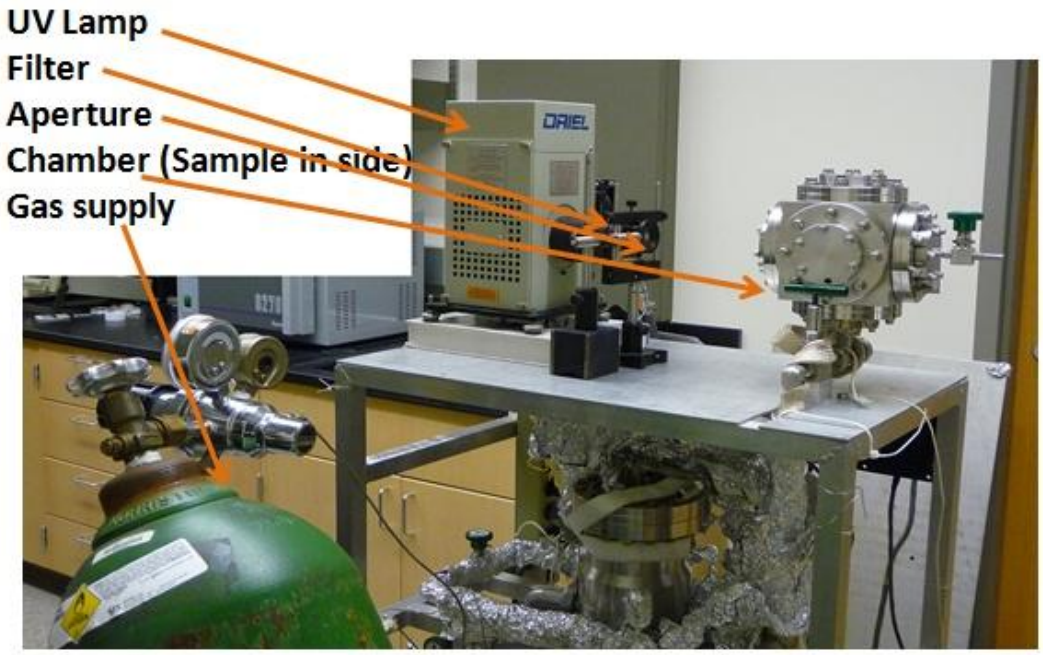

Figure 6-4: Experiment set up for UV irradiation

For mechanistic studies of the behavior of TiO_x films, a CaF_2 single crystal disk, 25 mm in diameter and 2 mm thick, is used as substrate. CaF_2 is transparent in the visible-infrared region. The TiO_x material was dissolved to 10 % by volume in methanol, and used at room temperature to spin coat ~ 200 nm films onto CaF_2 disk. The disk was coated and stored in the dark in air prior to use in the experiment. The thickness of the spin coated films was measured by a Veeco Dektak 8 stylus profilometer.

Transmission IR measurements were carried out with a Bruker Tensor 27 - FTIR spectrometer with a liquid nitrogen-cooled MCT detector. The spectrometer optical path was continuously purged with dry air, scrubbed of CO_2. The instrumental resolution was 2 cm^{-1} and typical spectra involved acquisition of 128 scans. The spin-coated disk was transferred to a stainless steel ultrahigh vacuum IR cell [74, 75]. The cell contained windows for both the IR measurements as well as for irradiation of the films. Oriel

66033 Hg arc lamp was used to irradiate the sample. The radiation from the lamp was filtered with a 10 cm column of water to remove IR radiation. UV light irradiate the sample in the cell at a 45˚ incidence angle.

Simultaneous UV irradiation and observation of changes in the transmission IR spectrum were carried out in vacuum with ~ 5×10^{-8} Torr base pressure and under an O_2 atmosphere at a pressure of 20 Torr. Separate IR spectra of the thin films and of the gas phase could be measured during irradiation by periodically translating the TiO_x films out of the IR beam. The spectral developments in the films alone were extracted by subtracting the gas phase spectra from the spectra of the films plus gas phase .

During some measurements, a small amount of ice condensed internally on the MCT detector giving a broad ice absorption band centered near 3300 cm^{-1}, and this band is to be disregarded. Most measurements did not involve this effect.

ESR measurements were made in a 4 mm diameter quartz ESR tube containing flakes of the fresh TiO_x films. The flakes are scraped from a glass slide, where TiO_x solution was spread and dried overnight in dark at room temperature in a N_2 environment. Exposure of the TiO_x to the UV lamp was carried out in the ESR tube. A Bruker ESP 3000 spectrometer, which was automatically calibrated internally, was employed. The ESR measurements were made under N_2 (g) or O_2 (g) at 1 atm pressure.

6.3. Results and Discussion

6.3.1. Study of solar cell degradation and improvements by TiO_x

Performance degradation was measured using the fabricated organic solar cell devices. Some of the degradation occurs during our fabrication process because most of the fabrication has been done in air. But the major degradation is governed by the UV and gas exposures.

At first we examined the effect of the gas environment on the degradation process. Figure 6-5 shows the change in normalized efficiency with time in dark. Significant degradation in solar cell efficiency was observed under air exposure. No degradation was noted when the experiment was repeated under nitrogen. The data also shows that significant protection is provided from air degradation by the presence of a TiO_x layer on top of the active layer.

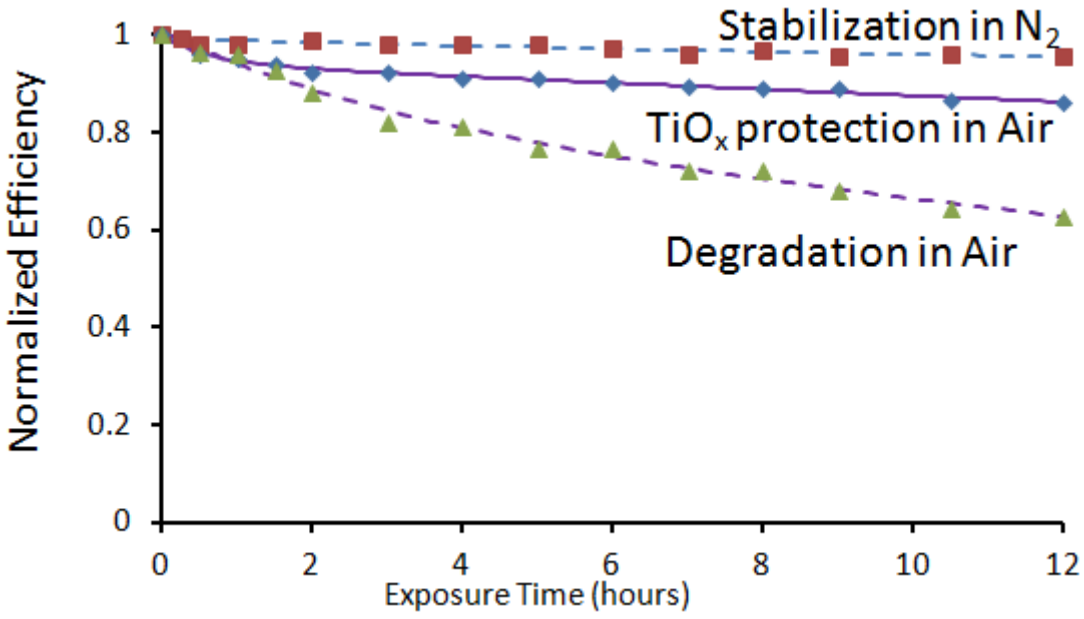

Figure 6-5: Variation of normalized organic solar cell efficiency in air and nitrogen in dark with time [72]

Then we examined the effect of UV irradiation on the degradation process. Figure 6-6 compares the protected and unprotected solar cells performance when exposed to UV radiation in a N_2 atmosphere. The presence of the TiO_x layer maintained the performance of the solar cells over time.

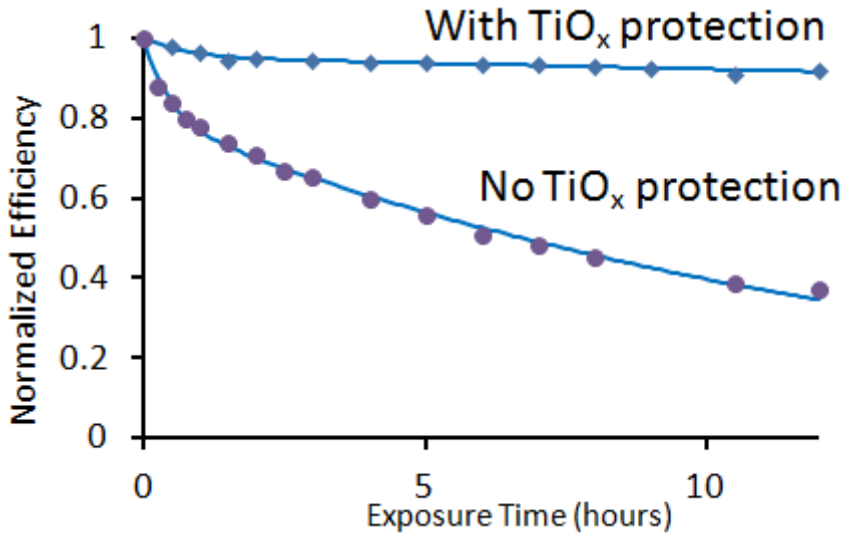

Figure 6-6: Variation of normalized organic solar cell efficiency under combined effect of UV and air exposure (UV power density = 10 mW/cm^2)[72]

The combined effect of gas environment and UV light was investigated as shown in Figure 6-7. The changes in normalized solar cell efficiency as a function of ultraviolet light/air exposure time for the P3HT/PCBM organic solar cell and for a cell with the TiO_x protection layer were presented. These data clearly indicate enhanced solar cell efficiency stabilization under UV irradiation in air caused by the presence of the TiO_x layer. The TiO_x protection is more effective in the presence of both UV and O_2. The TiO_x layer

when exposed to UV irradiation scavenges oxygen and consumes UV photons providing protection from UV and air exposure to organic solar cell devices.

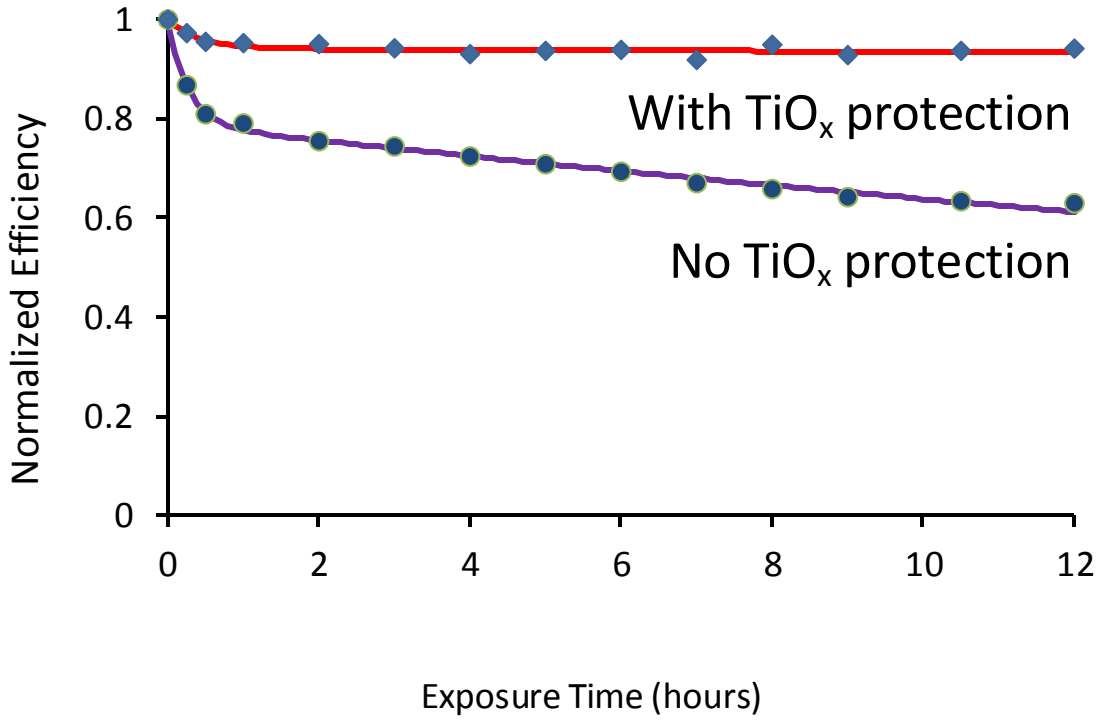

Figure 6-7**:** Variation of normalized organic solar cell efficiency with UV exposure time while the sample was in a nitrogen atmosphere. (UV power density = 10 mW/cm^2)[72]

The effect of UV light intensity was also examined. Figure 6-8 compares solar cell degradation under weak (10 mW/cm^2) and strong (300 mW/cm^2) UV irradiation in oxygen. Solar cells degrade faster when the UV flux increased 30 times. For both cases the presence of the TiO_x layer enhances the stabilization over time.

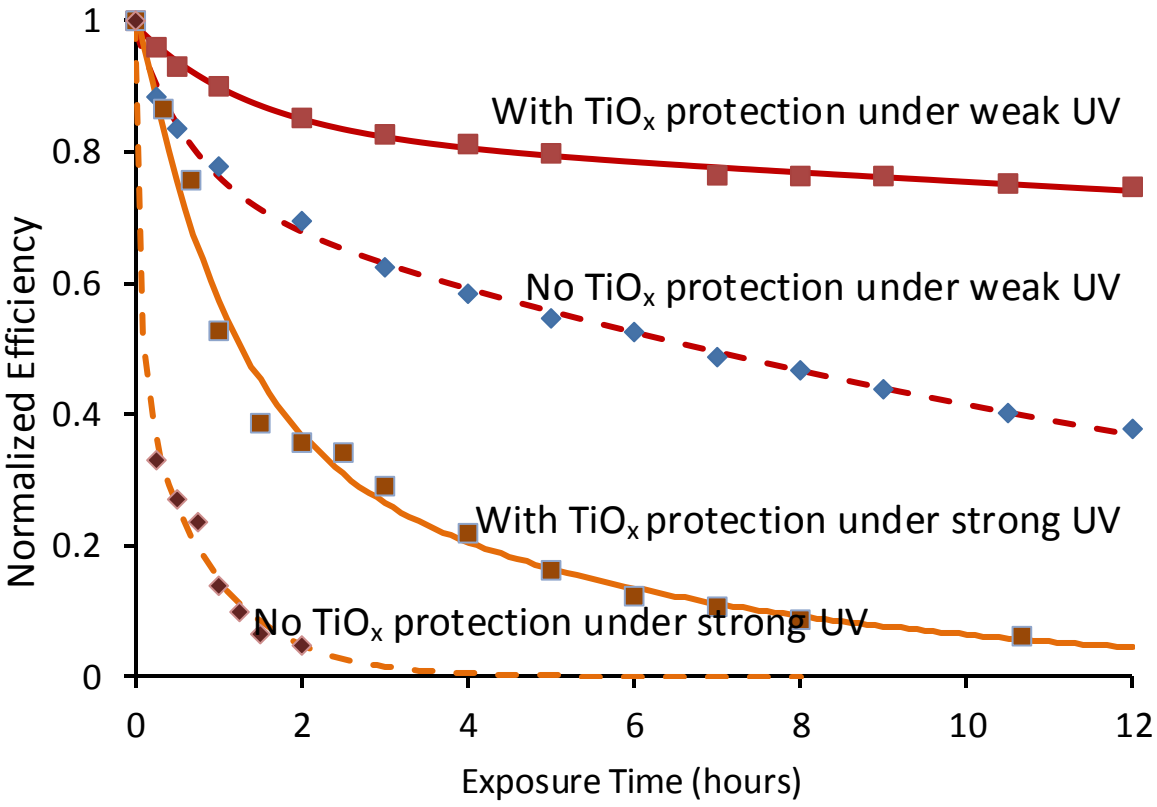

Figure 6-8**:** Variation of normalized organic solar cell efficiency with UV exposure time while the sample was surrounded by the 1 atmosphere oxygen environment. (weak UV power density = 10 mW/cm^2 and strong UV power density = 300 mW/cm^2)[72]

The degradation of P3HT/PCBM organic solar cells can be represented by two exponential terms that describes the fast initial decay and the long-term degradation.

$$\eta = \eta_0 [a\, e^{-\gamma t} + b\, e^{-\delta t}] \qquad (6\text{-}1)$$

where η_0 is the initial solar cell efficiency and a, b, γ and δ are curve fitting parameters [76].

The existence of the double exponential expression for the degradation of solar cells suggests that two major degradation processes act in parallel with time constant γ (hr^{-1}) and δ (hr^{-1}). The time constant γ indicates the fast decay process and δ is related to

slow decay. The decay process may be empirically expressed as the sum of two exponential degradation processes. But the degradation process is a complex process involving many factors. The two processes cannot be simply attributed to tow separable factors such as UV degradation of the polymer and oxygen-derived degradation of the active layer in this study.

It is noted that UV degradation obtained high values of γ than air exposure. It suggests that faster decay maybe due to UV exposure other than oxygen exposure.

We also examined the effect of the surrounding environment and UV irradiation on the various photovoltaic performance parameters such as open circuit voltage (V_{oc}), short circuit current (I_{sc}), fill factor (FF) and efficiency (η). Figure 6-8 shows the variation of V_{oc}, I_{sc}, and FF under UV irradiation in nitrogen. Similar results were obtained under air exposure conditions. The open circuit voltage remains essentially constant in the degradation process. It suggested that the energy level of the donor/acceptor did not change after degradation. The major loss of efficiency is due to lowering of the short circuit current and the fill factor. It suggested that the degradation affects the carrier transport of the devices.

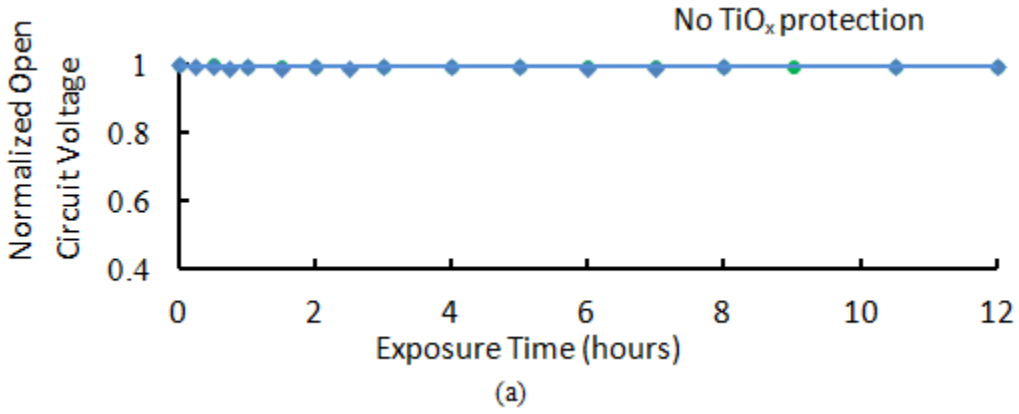

(a)

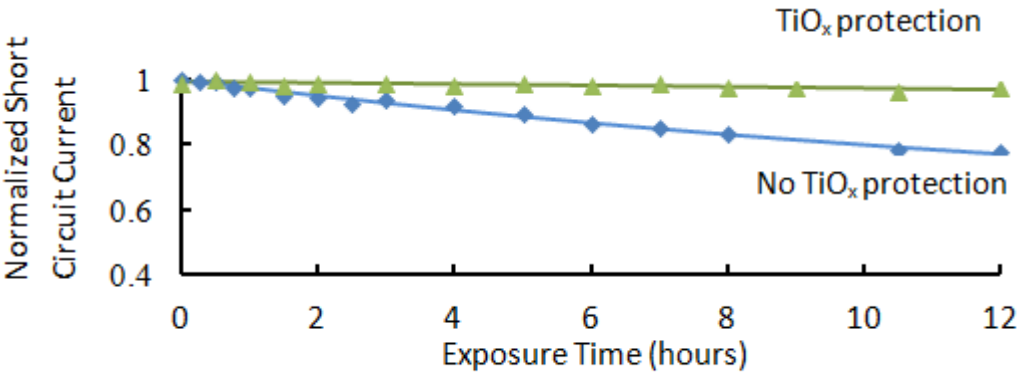

(b)

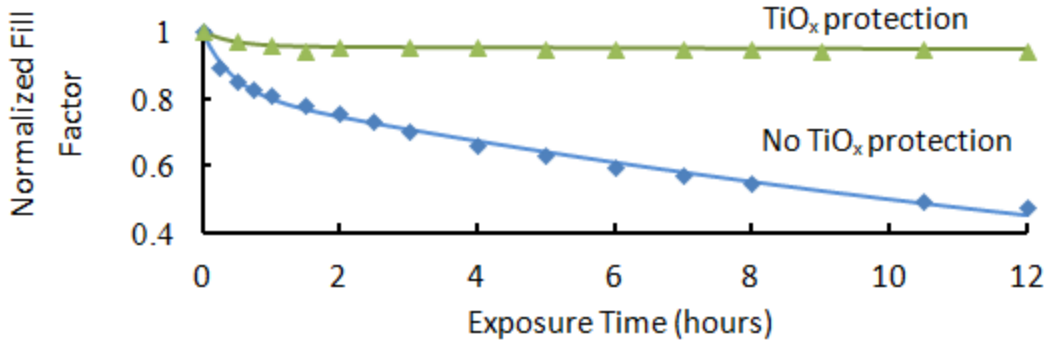

(c)

Figure 6-9: Variation of (a) open circuit voltage(V_{oc}), (b) short circuit current (I_{sc}) and (c) fill factor with UV exposure time when sample was surrounded by nitrogen atmosphere (UV power density = 10 mW/cm^2) [72]

A significant change in current vs. voltage curve shape was observed for the solar cell under air degradation. There is a kink in fourth quadrant. No change was noted when the TiO_x layer was used as a protection layer as indicated in Figure 6-10. Several authors [77,78,79] have reported the observation of kink in the fourth quadrant of Figure 6-10 and have provided some explanation [80,81]. Jørgensen [66] interpreted this effect as a counter diode behavior. This is considered to be due to the formation of an interfacial layer between active organic layer and metal electrode. TiO_x layer scavenges oxygen and it

works as barrier layer to prevent the formation of the interfacial layer. Therefore there is no such kink in the device with TiO_x.

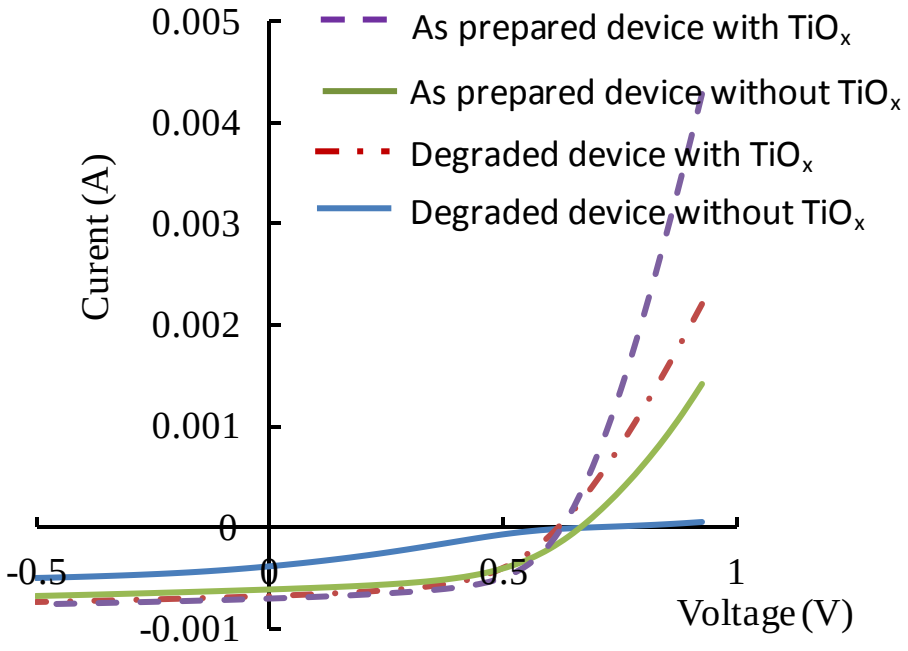

Figure 6-10: Current voltage characteristics data indicating the significant change in I-V curve shape due to air degradation[72]

Because the TiO_x absorbs UV light, this may help to protect the active layer. Therefore we studied the UV absorption effects of the protection layer. 20 nm TiO_x films were spun on quartz substrate to calculate the absorption of the TiO_x thin films. The optical path is shown in Figure 6-11.

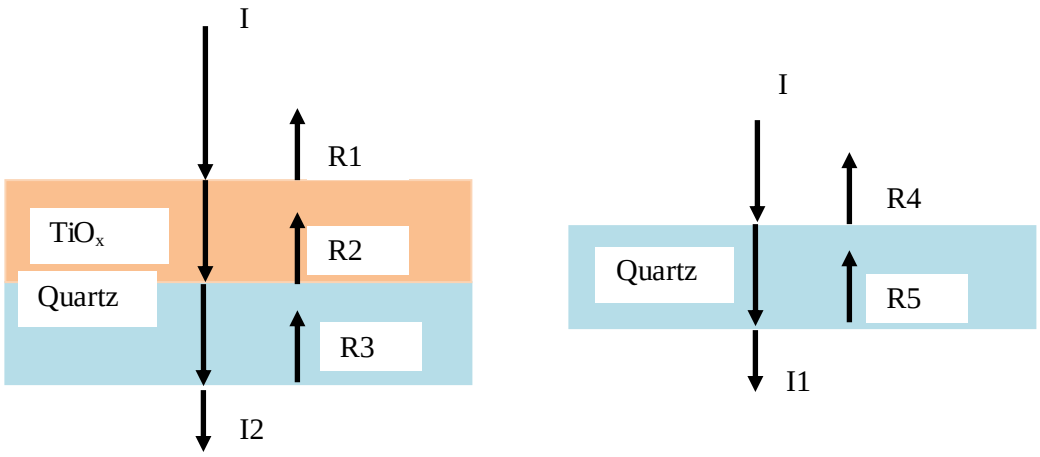

Figure 6-11: Optical path for absorption measurement of quartz substrate and TiO_x film on quartz.

The transmission from quartz is

$I1=I[(1-R4)- ABS_{quartz} -(1-R4-ABS_{quartz}) \times (1-R5)]$

The transmission from TiO_x on quartz is

$I2=I \{(1-R1)- ABS_{TiOx} -(1-R1- ABS_{TiOx}) \times (1-R2)- ABS_{quartz} -[(1-R1)- ABS_{TiOx} - (1-R1- ABS_{TiOx}) \times (1-R2)- ABS_{quartz}] \times (1-R3)\}$

where

$R1=\left|\frac{1-n_{TiO_x}}{1+n_{TiO_x}}\right|^2$ is the reflection at the Air/TiO_x interface

$R2=\left|\frac{n_{TiO_x}-n_{quartz}}{n_{TiO_x}+n_{quartz}}\right|^2$ is the reflection at the TiO_x/Quartz interface

$R3=\left|\frac{1-n_{quartz}}{1+n_{quartz}}\right|^2$ is the reflection at the Quartz/Air interface

$$R4=\left|\frac{1-n_{quartz}}{1+n_{quartz}}\right|^2$$ is the reflection at the Air/Quartz interface

$$R5=\left|\frac{1-n_{quartz}}{1+n_{quartz}}\right|^2$$ is the reflection at the Quartz/Air interface

ABS_{quartz} is the absorption of the 1 mm thick quartz. ABS_{quartz} is the absorption of the 20 nm TiO_x films.

The measured absorption spectrums of quartz substrate and TiO_x film on quartz are shown in Figure 6-12.

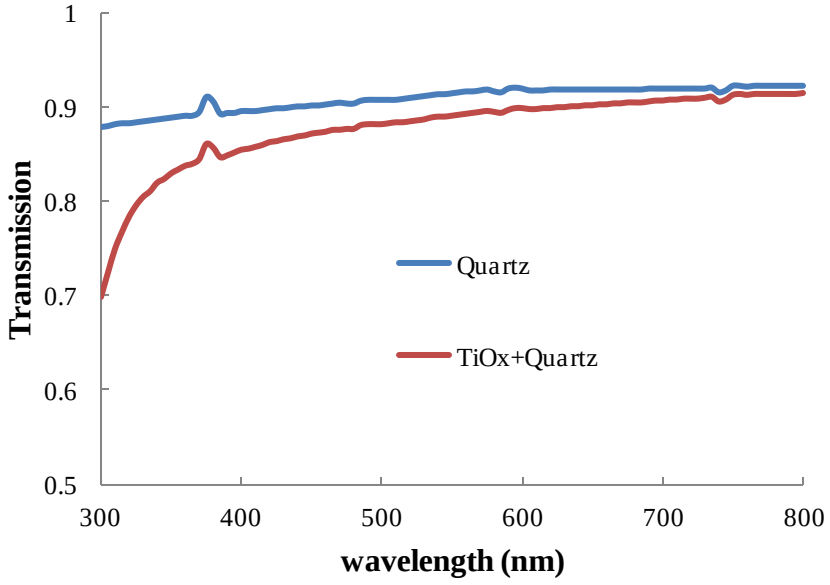

Figure 6-12: Absorption spectrum of quartz substrate and TiO_x film on quartz

The calculated absorption of 20 nm TiO_x films is shown in Figure 6-13 (a). The corresponding absorption coefficient of TiO_x is shown in Figure 6-13 (b). The 20 nm films would absorb less than 15 % of the photons in the UV region. It may affect the UV induced degradation. But it is not the major factors.

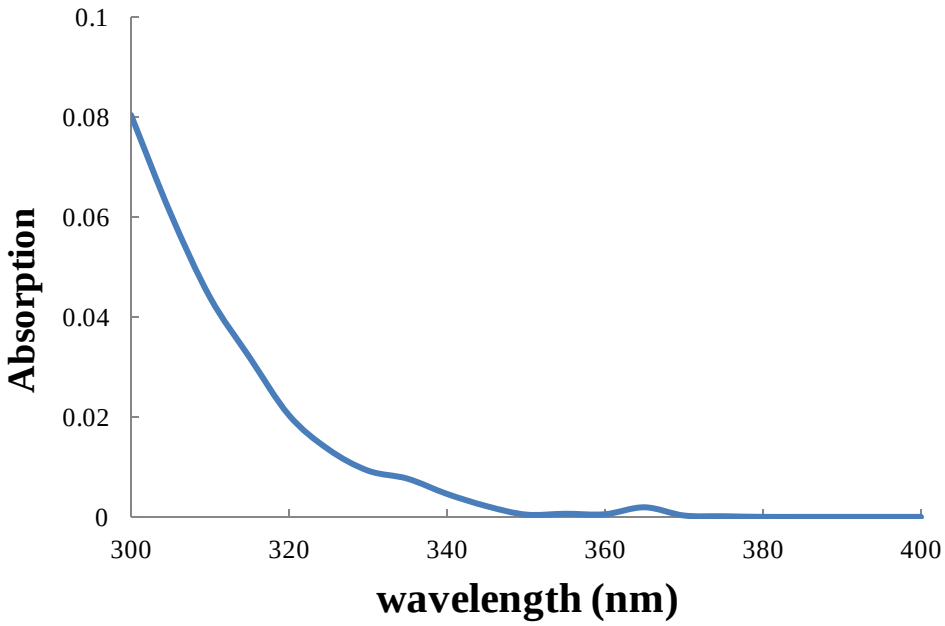

(a)

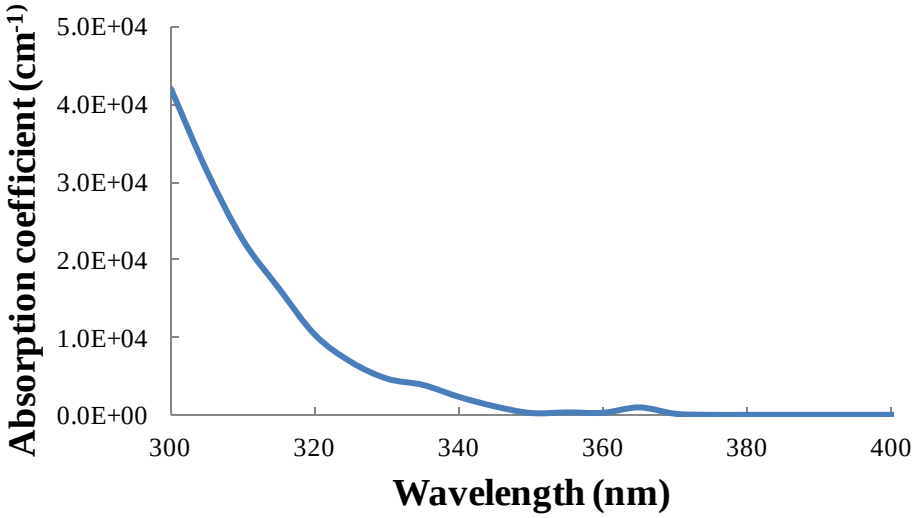

(b)

Figure 6-13: The calculated absorption of 20 nm TiO_x films (a) absorption spectrum (b) corresponding absorption coefficient

6.3.2. TiO_x improvement mechanism study

TiO_x films contains both Ti-OR functionalities and Ti-OH groups throughout. The residual Ti-OR functionalities bound into the sol-gel films are photooxidized under UV irradiation. The process consumes O_2 (gas) and produces CO_2 (gas) and H_2O (gas), as well as bound formate [HCOO-], H_2O and Ti-OH moieties. The photo activation of TiO_x films leads to O_2 scavenging which removes absorbed oxygen that would degrade the solar cell devices. Thus, TiO_x film protects the underlying surface from oxygen gas.

Figure 6-14 shows the infrared spectral measurements of the production of CO_2 (gas) and H_2O (gas) during UV photoactivation of the TiO_x film at room temperature during which the $^{16}O_2$ pressure was 20 Torr. Broadened CO_2 vibration-rotation bands, centered at 2349 cm^{-1}, is observed (asymmetric stretching mode) over the 32 hour irradiation period. It indicates that CO_2 is monotonically generated. Two spectral regions for H_2O (gas) are also observed. One is centered near 3700 cm^{-1} (stretching mode) and another is near 1600 cm^{-1} (bending mode). It indicates the monotonically develop absorbance of H_2O (gas). The infrared peaks positions were identified in accordance with the reported results as described in reference [82].

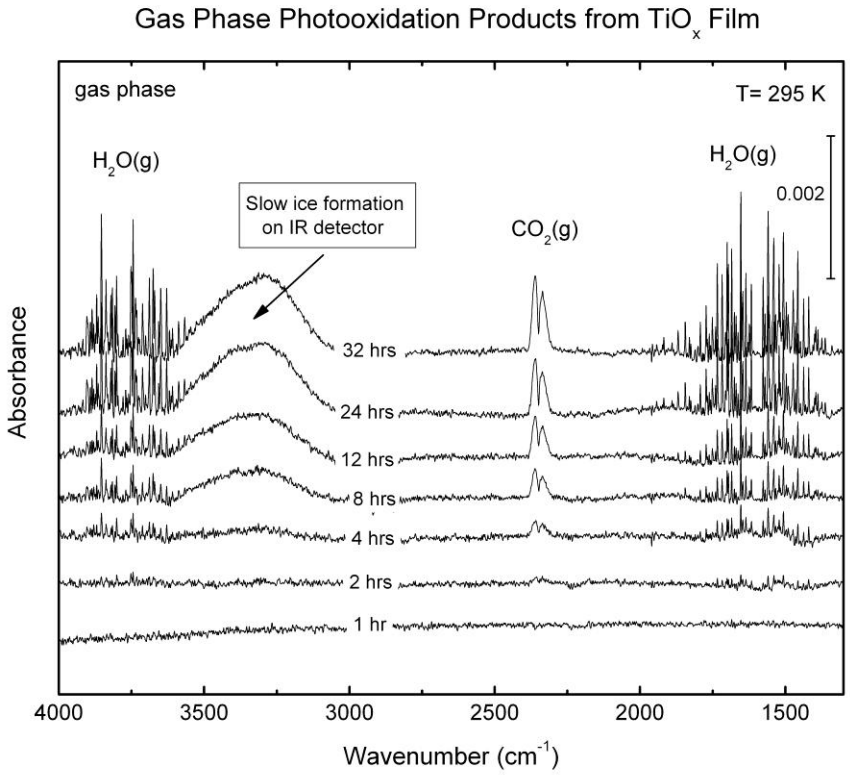

Figure 6-14: Gas phase photooxidation products from TiO_x films containing alkoxide functionalities. CO_2 (gas) and H_2O (gas) are observed. The slow formation of ice on the IR detector is an artifact to be disregarded. The spectrum through the gas phase at each time was ratioed by the spectrum taken before UV irradiation [72]

Figure 6-15 shows the infrared spectral developments when the TiO_x films are irradiated during an 8 hours at room temperature under $^{16}O_2$ (gas) at 20 Torr pressure. Characteristic of the alkoxide functional groups remaining in the TiO_x films is observed in the (C-H) stretching region. It may be seen that considerable loss of absorbance occurs at 2926 cm^{-1} and 2853 cm^{-1} when photooxidation of the alkoxide takes place. The modes at the frequencies above the (C-H) stretching region are due to surface hydroxyl (Ti-OH) groups and adsorbed water in the TiO_x films and their absorbances are observed to grow

during the photooxidation process. A very weak C≡N stretching mode [ν(C≡N)] at 2201 cm^{-1} is observed. It is due to the photo-oxidation of residual ethanolamine from the TiO_x precursor preparation.

Shifting to a congested spectral region below 1750 cm^{-1}, where asymmetric and symmetric OCO stretching modes develop for HCOO− species, subtle increases occur in absorbance at 1567 cm^{-1} and 1359 cm^{-1}, as marked. The vibrational frequencies observed are close to those found for formate species [HCOO−] on TiO_2 in published reports [83,84,85,86].

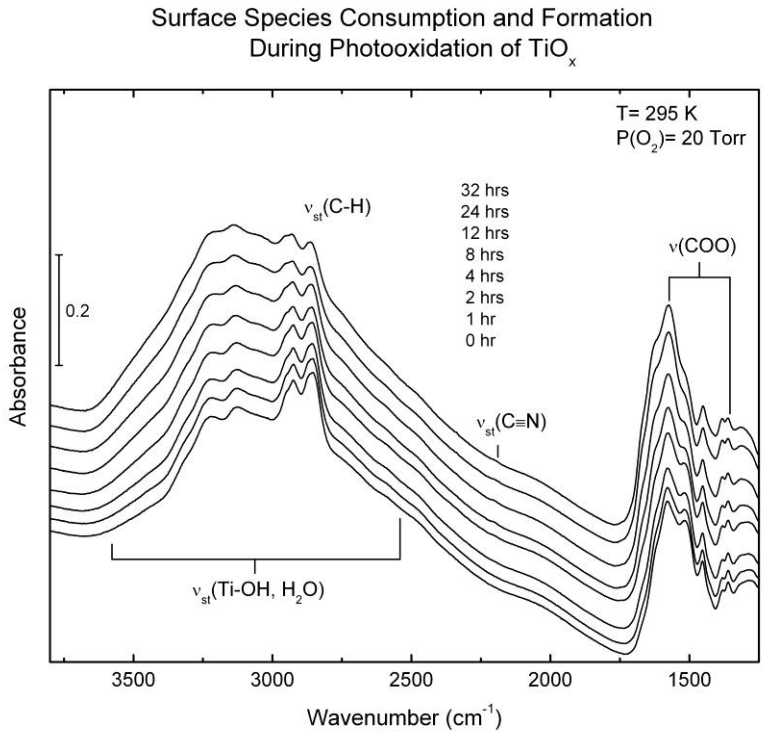

Figure 6-15: Surface species consumption and formation during photooxidation of TiO_x films containing alkoxide functionalities. The consumption of the alkoxide functionality is accompanied by the formation of carboxylate and hydroxyl surface-bound species, as well as nitrile moieties from the oxidation of ethanolamine [72]

Figure 6-16 shows ESR spectra of TiO_x material recorded after exposure to UV irradiation for 15 minutes in 1 atm of O_2 (g) at 295 room temperature. Three strong ESR features are observed at g = 2.030, g= 2.006 and g = 2.001. The three ESR transitions are assigned to adsorbed O_2^- [87,88]. The trapping of the electron by O_2 stabilizes the hole produced in the TiO_x films.

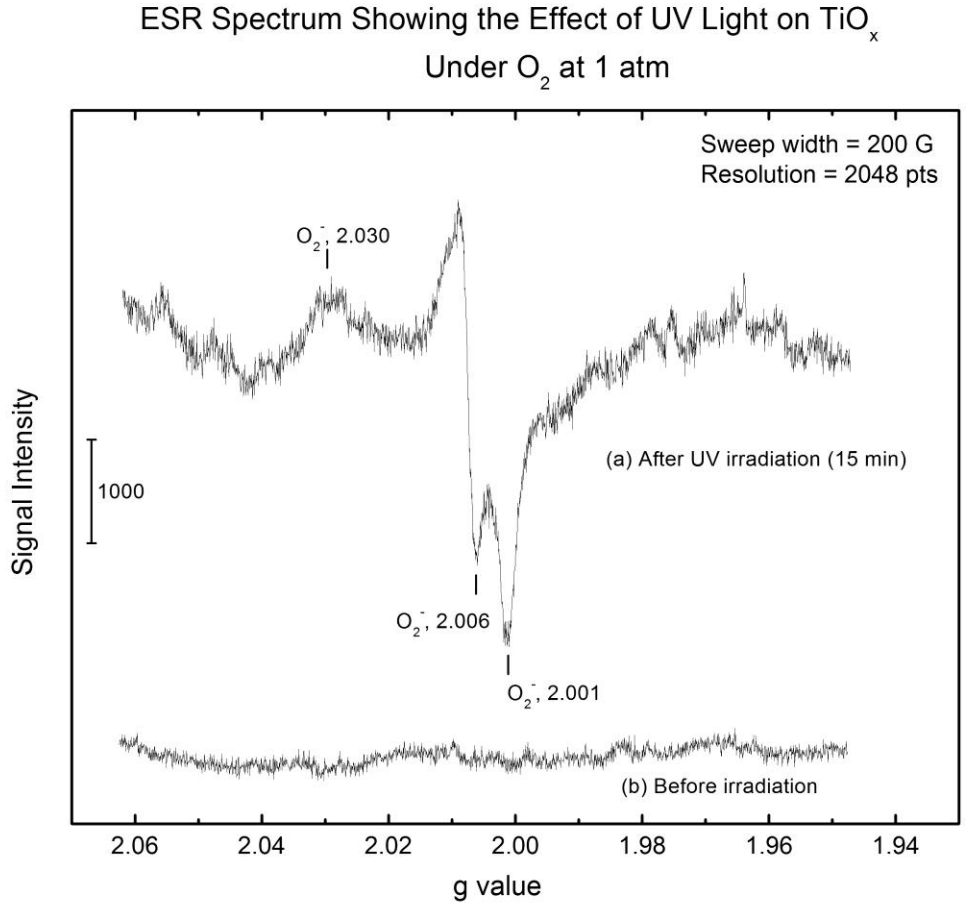

Figure 6-16: ESR spectrum showing the effect of UV light on TiO_x under O_2 at 1 atm. (a) after UV irradiation, 15 minutes; (b) before irradiation[72].

There is no production of O_2^- by UV irradiation for 60 minutes with the TiO_x sample under 1 atm of N_2, as shown in Figure 6-17. Compared to the results found for UV irradiation in O_2 in Figure 6-16, the results clearly indicate that the photo-formation of trapped electrons is directly associated with the formation of adsorbed O_2^-. O_2 (g) is required for photochemical formation of O_2^- species in TiO_x.

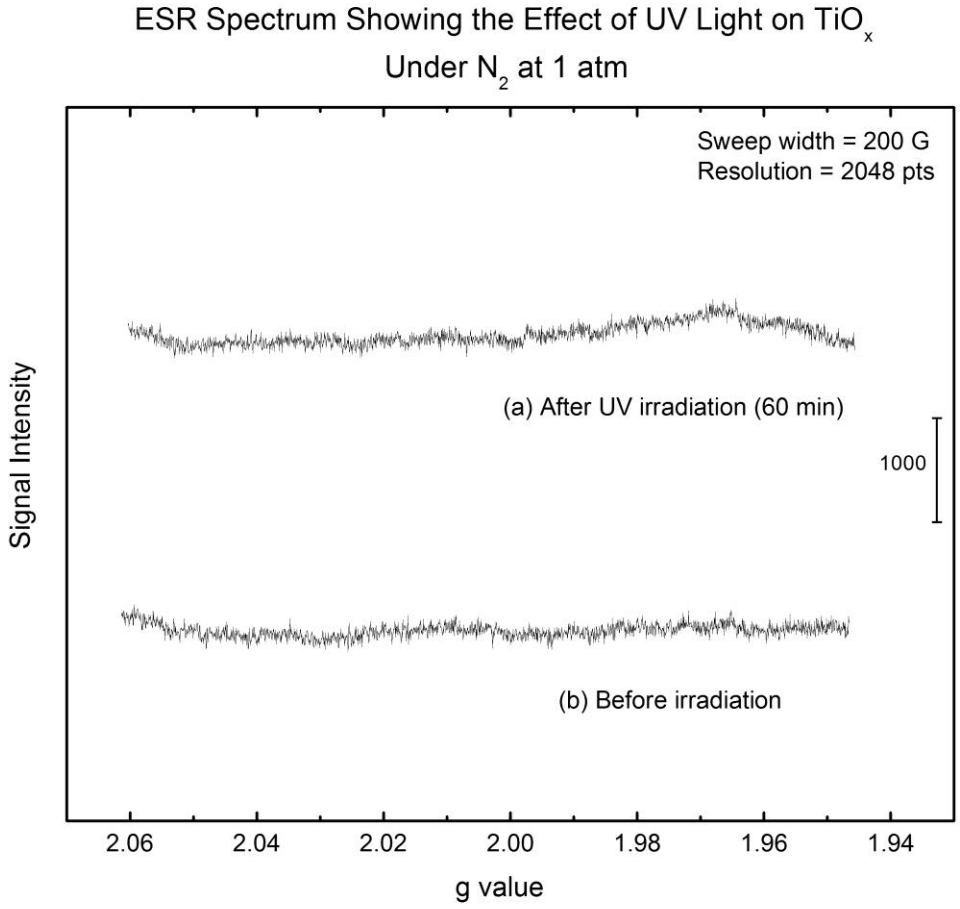

Figure 6-17: ESR spectrum of the effect of UV light on TiO_x under N_2 at 1 atm. (a) after UV irradiation, 60 minutes; (b) before irradiation. The results, compared to Figure 6-16, show that O_2^- species require O_2(g) for photochemical formation on TiO_x[72]

The ability of TiO_x films, containing internally chemically-bound alkoxide groups, to photochemically consume oxygen is not surprising based on the wide utility of TiO_2 for the photooxidation of *ex situ* organic and inorganic matter [89,90,91]. The TiO_x films carries its own sacrificial organic reactant while also containing ultraviolet light absorbing ⋯Ti-O-Ti⋯structures throughout the films, capable of making electron-hole pairs which then promote redox processes. It is also observed that the presence of adsorbed O_2 facilitates electron-hole pair separation by acting as an electron acceptor.

6.3.3 Protection capacity calculation

Estimation of the capacity of the bound –OR a group within the TiO_x films for reaction with oxygen gas is calculated here:

A 20 nm film of TiO_x contains about 3×10^{16} TiO_x units per cm^2. There is about 10 - 50 mole % of $–OCH_3$ groups exist in the films. The capacity for photo-oxidative reaction with O_2 is of order of $3 \times 10^{15} – 1.5 \times 10^{16}$ O_2 molecules cm^{-2}. There is a volume of about 1×10^{-5} cm^3 for the 120 nm active layer with 1 cm^2 surface area. It is reported that the critical doping level for electron traps generated by O_2 for P3HT is between 10^{16} cm^{-3} [92] and 10^{17} cm^{-3} [93]. It is about $10^{11} – 10^{12}$ per cm^2 of active area. Thus, the TiO_x protective films have a capacity of the order of 10^4 to 10^5 times than the quantity of O_2 which is needed to seriously influence the active layer performance.

As stated in the introduction chapter, oxygen deficiencies in the TiO_x films also provide adsorption sites for O_2. The TiO_x layer also acts as a diffusion barrier for oxygen which slows down the oxygen travel. The combination of these three mechanisms provides of the TiO_x protection for organic solar cells. Table 6-2 shows comparison of

efficiency degradation with time for the device with TiO_x protection and device without TiO_x. The efficiency of device without TiO_x protection degraded from 1.92% to 0.09% after 1 week while the efficiency of device with TiO_x protection degraded from 2.39% to 1.91%. The comparison indicates that the protection of TiOx lasts more than one hundred hours.

Table 6-2: Comparison of efficiency degradation with time for the device with TiO_x protection and device without TiO_x

	As prepared	1 week
Device without TiO_x	1.92%	0.09%
Device with TiO_x	2.39%	1.91%

6.4. Conclusions

From this study on stabilization of P3HT/PCBM based organic solar cells with a TiO_x layer, we can draw following conclusions:

(1) The P3HT/PCBM organic solar cell efficiency decreases with increase in air exposure time. No change was noted under nitrogen. Thin films of TiO_x on top of the active layer provided significant protection from air degradation.

(2) The cell performance decreases with increasing UV exposure under nitrogen. Thin films of TiO_x layer on top of the active layer provided significant protection from UV exposure.

(3) A higher decrease rate in cell efficiency was noted when exposed to the combined effect of UV and oxygen, as compared to the individual effects. The TiO_x protection is more effective in the presence of both UV and O_2. The TiO_x layer scavenges oxygen and consumes UV photons providing protection from UV and air exposure to organic solar cell devices.

From the TiO_x mechanism study, we have discovered the following properties of TiO_x sol-gel films which act as photochemically-activated oxygen scavengers:

(1) UV irradiation of TiO_x films containing alkoxide groups remaining from the sol-gel synthesis leads to the photochemical oxidation of these organic groups. This process removes O_2(gas) and forms H_2O (gas), CO_2 (gas), chemically-bound formate [HCOO-], H_2O(ad) and Ti-OH oxidation products. It is the photochemical removal of O_2 by TiO_x films that is postulated to lead to passivation of organic photocells from oxygen induced degradation.

(2). O_2^- species are observed to form where TiO_x films are irradiated in O_2 (g) at room temperature. In the absence of O_2 (g), these species are not detected by ESR upon UV irradiation.

Chapter 7. **Laser beam induced current mapping study on organic solar cell with TiO_x protection layer**

7.1 **Introduction**

Traditional electrical characterization of solar cells, which involves extracting the photovoltaic parameters such as open circuit voltage (V_{oc}), short circuit current (I_{sc}), fill factor and efficiency (η) by performing I-V scan, is useful for determining the overall parameters of solar cells. But it does not show the local information of the cells. The inhomogeneity of the local photocurrent has been reported in organic solar cells upon degradation for P3HT/PCBM cells [94]. T. Jeranko et al. conclude that degradation mechanisms appear to have a morphological component in MDMO-PPV/PCBM composite polymer solar cells [95]. This type of measurement is complemented with laser beam induced current (LBIC) mapping of the devices to gain further insight into the local degradation of the cells.

LBIC imaging is a non-destructive characterization technique suitable for the investigation of large two-dimensional arrays of semiconductor devices. It is a very useful tool in determining the spatial variability of properties such as power conversion efficiency and has been used to study defects [96] and crystalline effect [97] for organic solar cells.

In this chapter, we will use LBIC measurements to explore local photocurrent distribution in the cells with and without TiO_x protection layer and analyze the obtained degradation patterns.

7.2 Experiment

7.2.1 **Organic solar cell fabrication**

The organic solar cells were fabricated according to previous chapters with an effective active area of 0.1 cm^2. The photovoltaic parameters of the device with and without TiO_x layer are shown in Table 7-1.

Table 7-1: The photovoltaic parameters of the device for LBIC study

Device	Efficiency	V_{oc} (V)	J_{sc} (mA/cm^2)	Fill Factor (%)
No TiO_x	1.96	0.696	6.1	46.1
With TiO_x	2.36	0.708	7.17	46.5

7.2.3 **LBIC set up**

A schematic of LBIC set up is shown in Figure 7-1.

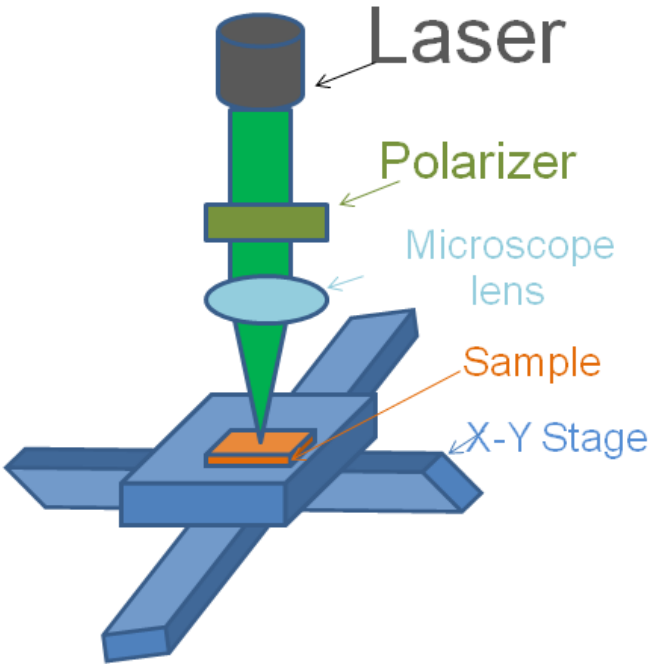

Figure 7-1: A schematic of LBIC set up

The the P3HT/PCBM blend (45%: 55%) absorption peak is around at 500~550 nm [98], a green diode laser (532 nm) following Gaussian power distribution was chosen as light source. The laser beam was focused on the cell in a small spot and the resulting photocurrent was measured point by point. The intensity, adjustable by polarizer, of the focused laser beam was 50 mW/cm^2 as measured by power detector.

The solar cells were mounted on a scan stage which allows movement of the sample in the x and y directions. The spatially resolved photocurrent images were obtained.

The image resolution depends on the size of the laser spot and scanning process. The limiting factor is the microscope lenses through which laser beam was focused. The laser beam was focused to 25 μm, which was measured by laser beam profiler (BP109-VIS, Thorlab).

A custom written computer program by Labview [99] was used to scan the solar cell devices in a pattern of 25 μm increment in the X and the Y directions, logging the increment coordinates and measured current. The current induced by the laser beam from the device was measured using a computer-interfaced source measure unit (Keithley 2600 instrument). The results were then converted into 2-D maps by Origin lab V7.5.

7.3 Results and discussion

7.3.1 Efficiency patterns

The current mapping for as prepared device with TiO_x layer is shown in Figure 7-2(a). Bright red represents the highest absolute current extracted while black represents the lowest current.

Devices with high initial efficiency usually show good uniformity. Less uniformity is indicated by larger LBIC variations in poor performing cells, as shown in Figure 7-2 (b).

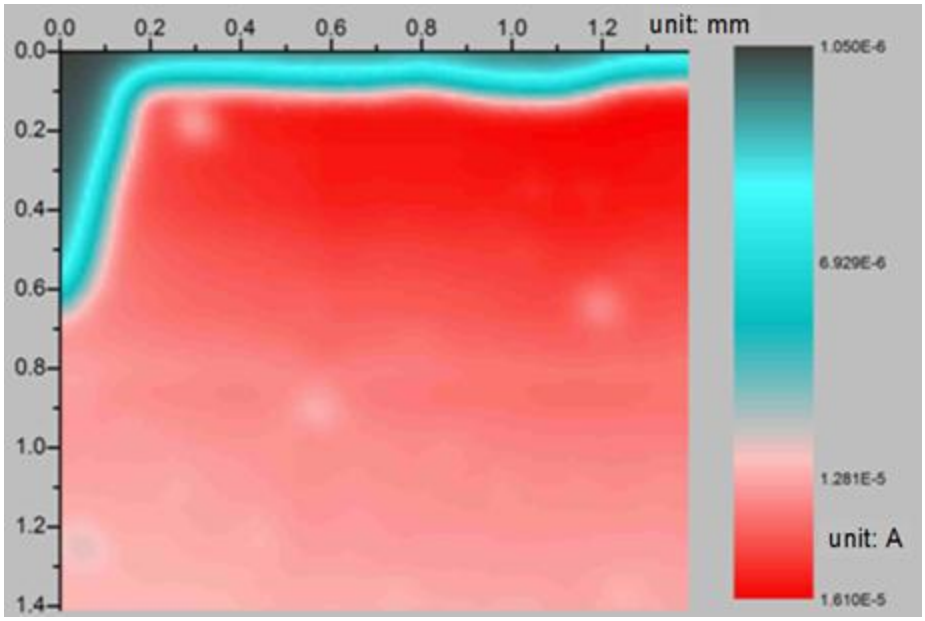

(a)

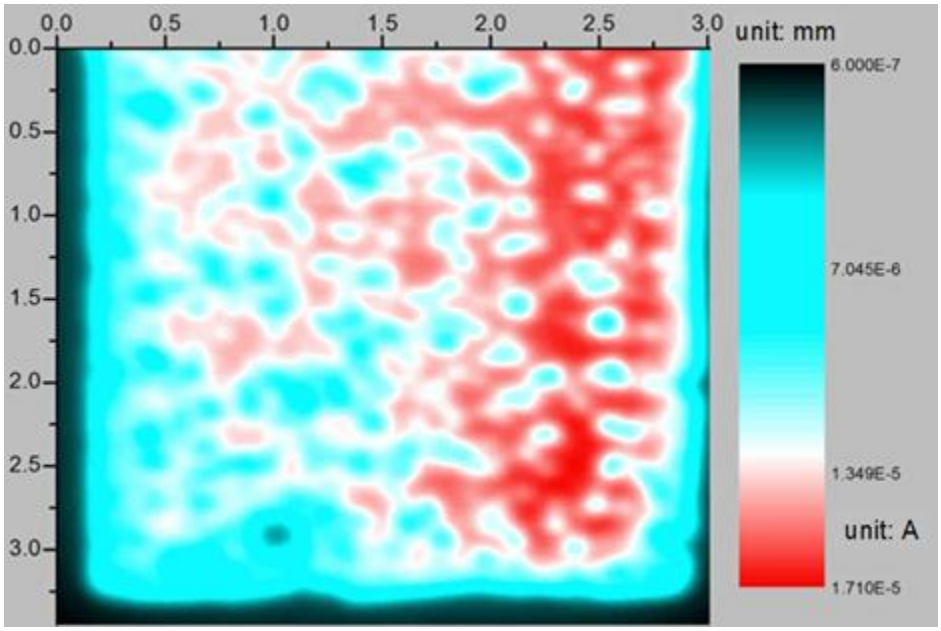

(b)

Figure 7-2: LBIC mapping of as prepared devices (a) with TiO_x (device efficiency η=2.4) (b) without TiO_x (device efficiency η=1.6)

7.3.2 Island formation

Upon degradation, islands of lower photocurrent occur. Figure 7-3 (a) shows defects regions. The islands in rectangular area are due to the bubbles in the Al contact, which form during the 130 ℃ annealing process as the remaining solvent, such as chlorobenzene, evaporates. The circular regions are most likely due to the non-uniformity in coating.

Figure 7-3 (b) shows defect regions appearing after degradation. It is probably due to the oxidation due to the microscopic pinholes in the Al electrode surface from ambient air. It has been reported that oxygen diffuses through pinholes in the aluminum electrode [100]. The sizes of the pin holes are up to a few micrometers in diameter and

their depth may be up to tens of nanometers. The aluminum electrode experiences oxidation/degradation in both the lateral and vertical plane.

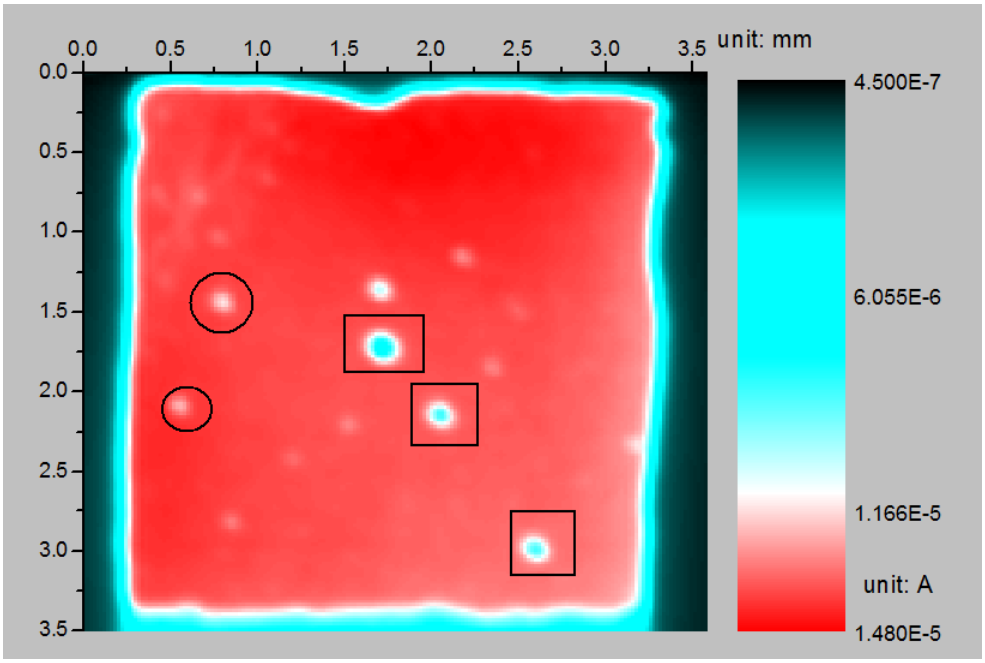

(a) as prepared device

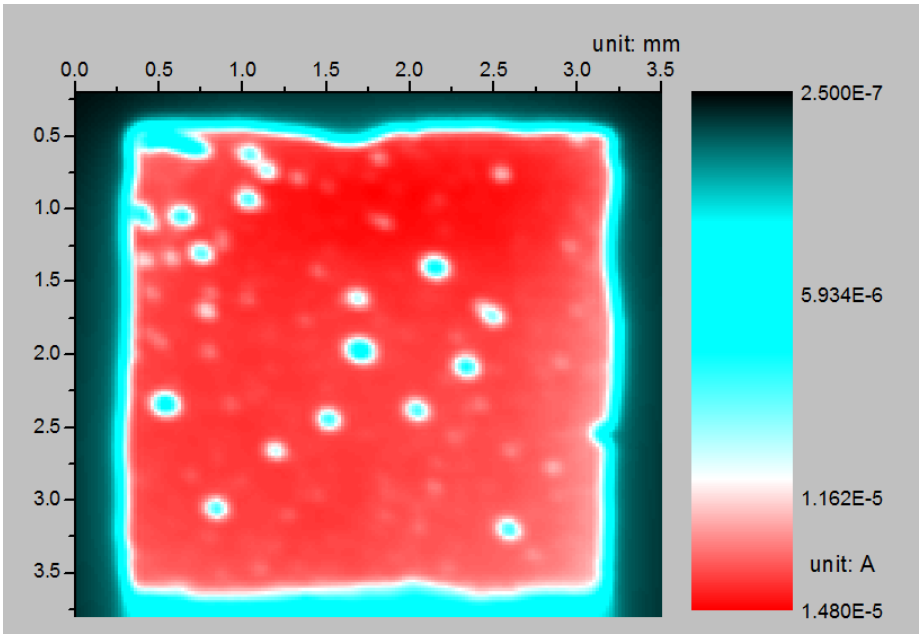

(b) Degraded device

Figure 7-3: Degradation pattern of OSC device with TiO_x layer (a) as prepared device (b) device degraded in dark for 1 week.

7.3.3 Comparison of devices with/without TiO_x protection

Figure 7-4 shows the degradation of the devices without TiO_x protection for 10 days. The LBIC mapping of as prepared cells without the TiO_x layer is shown in Figure 7-4(a). Figure 7-4(b), 7-4(c) and 7-4(d) show the device at various stages of degradation. As degradation occurred, the active area had apparently shrunk and more and more spots of low-photocurrent appeared.

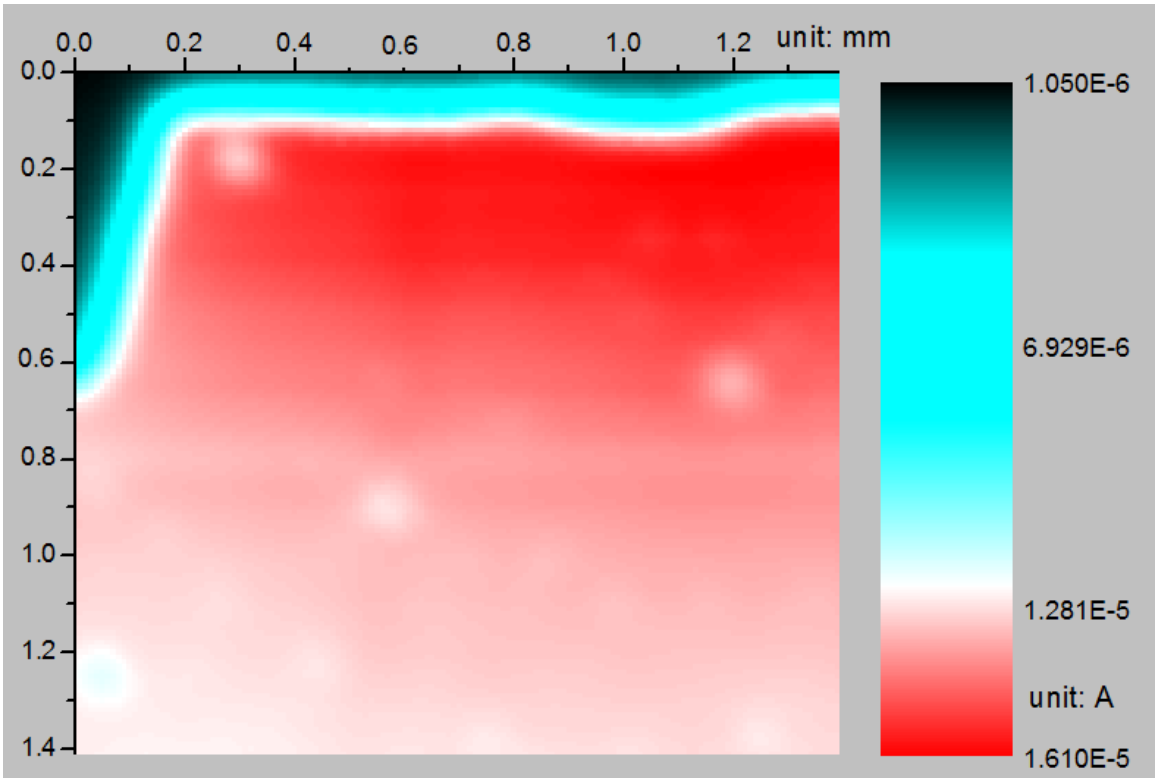

(a) as prepared device

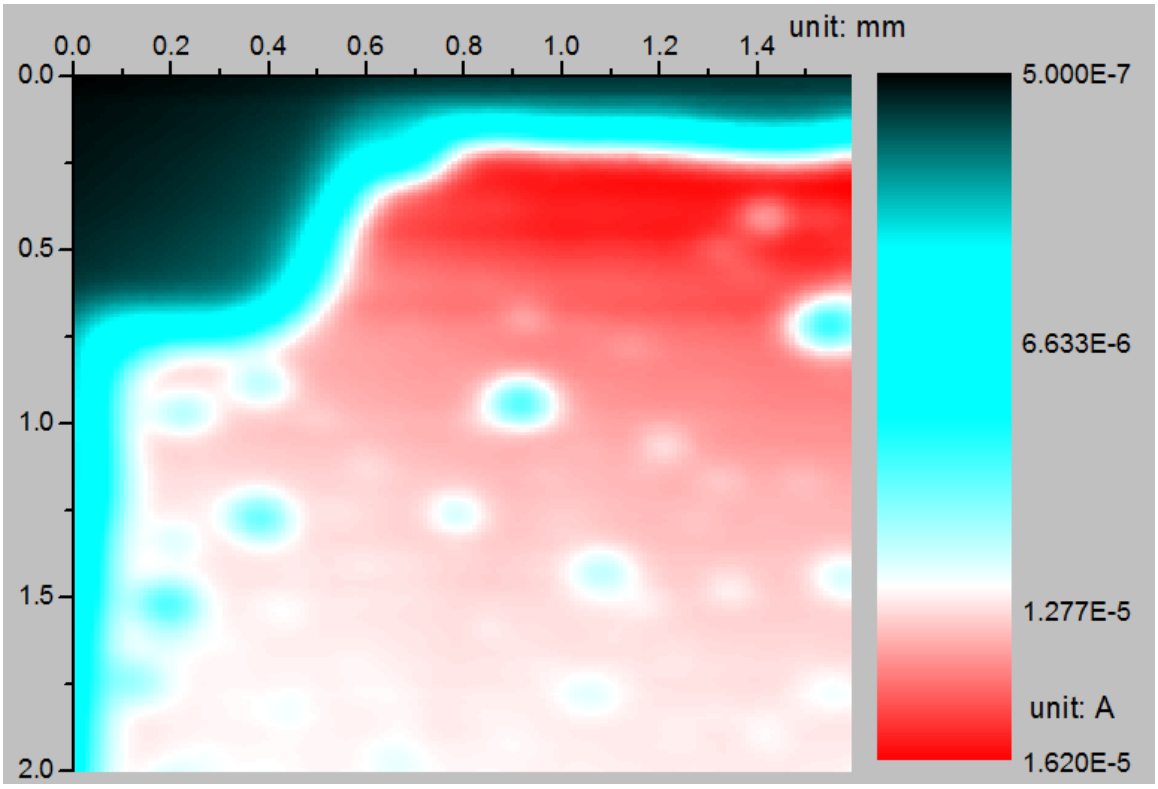
unit: mm
0.0
0.2
0.4
0.6
0.8
1.0
1.2
1.4
0.0
0.5
1.0
1.5
2.0
5.000E-7
6.633E-6
1.277E-5
unit: A
1.620E-5

(b) 1 day

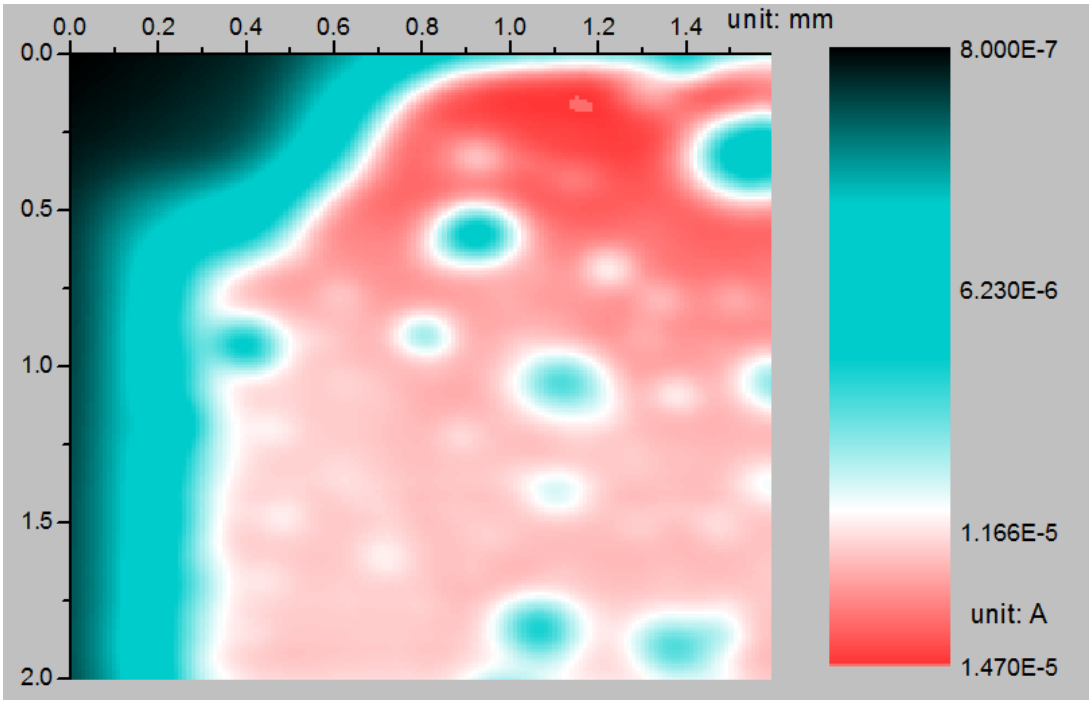
unit: mm
0.0
0.2
0.4
0.6
0.8
1.0
1.2
1.4
0.0
0.5
1.0
1.5
2.0
8.000E-7
6.230E-6
1.166E-5
unit: A
1.470E-5

(c) 3 days

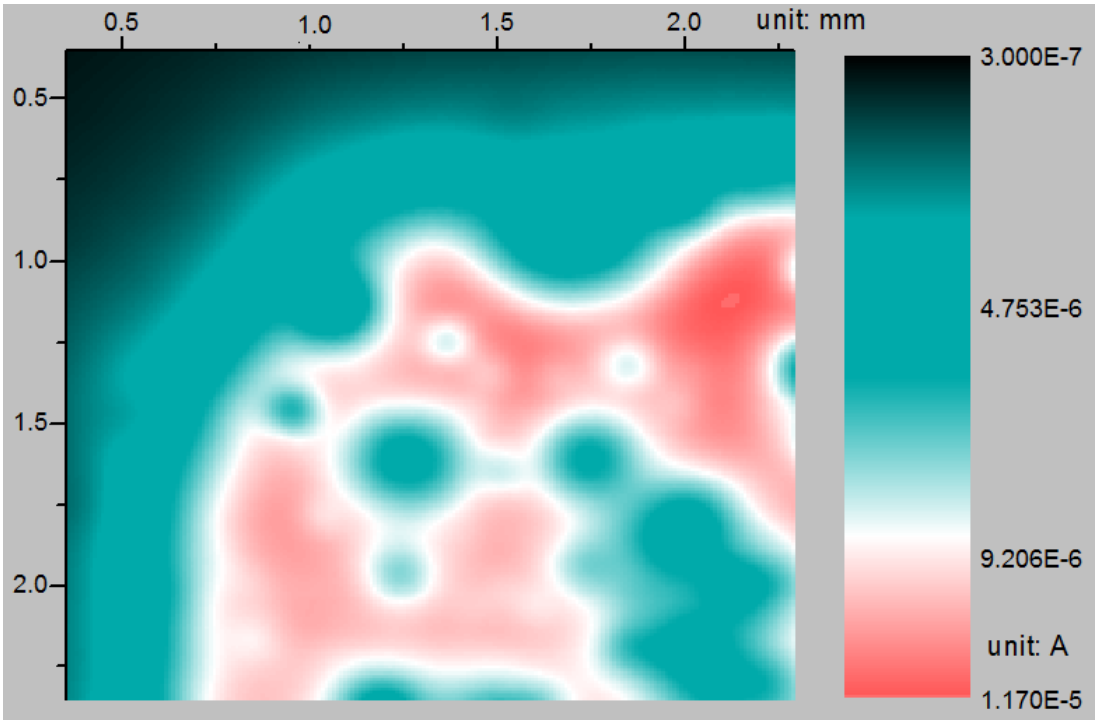

(d) 10 days

Figure 7-4: The mapping of degradation process for device without TiO_x protection (a) as prepared device (b) degradation after 1 day (c) degradation after 3 days (d) degradation after 10 days

For the cells with TiO_x protection layer, low photocurrent points were also observed (see Figure 7-5). But the shrinkage of the active area was not observed, and degradation spots were much smaller in comparison with the cell without the TiO_x layer.

It is also confirmed by full devices scanning. Figure 7-6 shows the current mapping of degradation of full device without TiO_x protection layer. Compared with device with TiO_x layer, as shown in Figure 7-3, the device without TiO_x layer degraded less in the device central region.

It has been reported that the shrinkage of the active region could be due to water in ambient air and oxidation of the contact [94]. PEDOT: PSS absorbs water from ambient air and accelerates the oxidation of Al, resulting a reduction in the efficiency. The TiO_x layer absorbs water and oxygen, therefore it prevents degradation from the edge area.

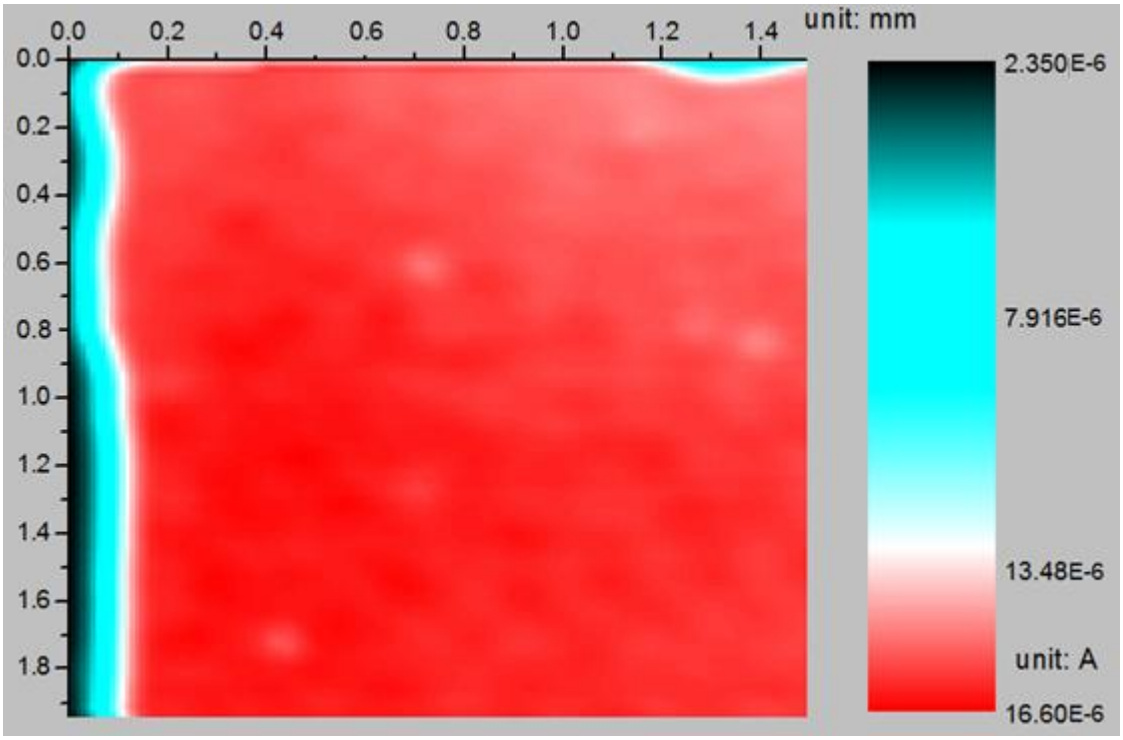

(a) as prepared device

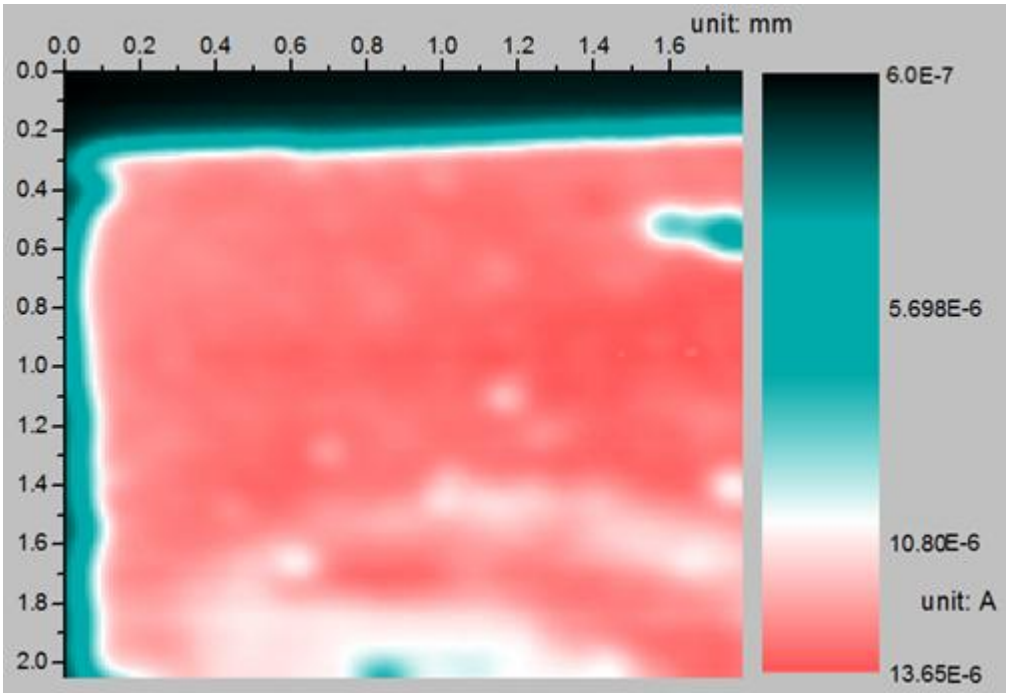

(b) 1 day

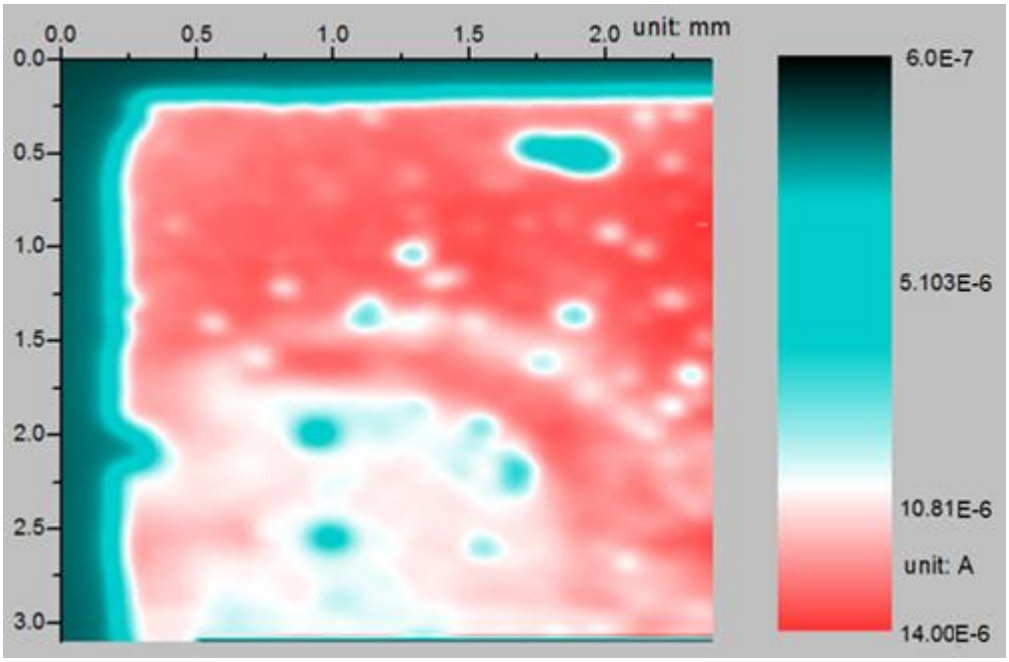

(c) 5 days

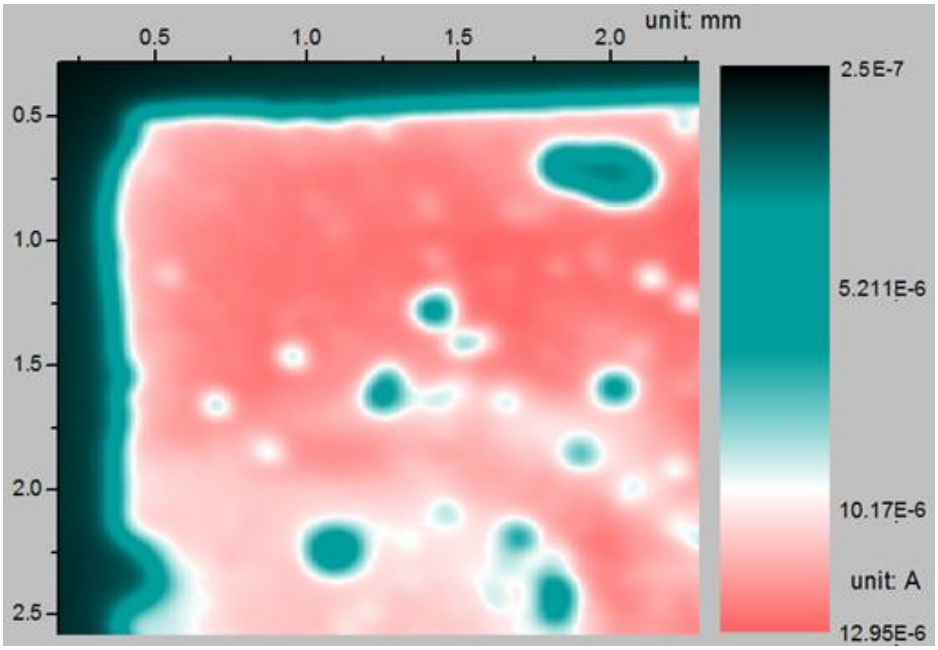

(d) 10 days

Figure 7-5: The current mapping of degradation process for device with TiO_x protection (a) as prepared device (b) degradation after 1 day (c) degradation after 5 days (d) degradation after 10 days

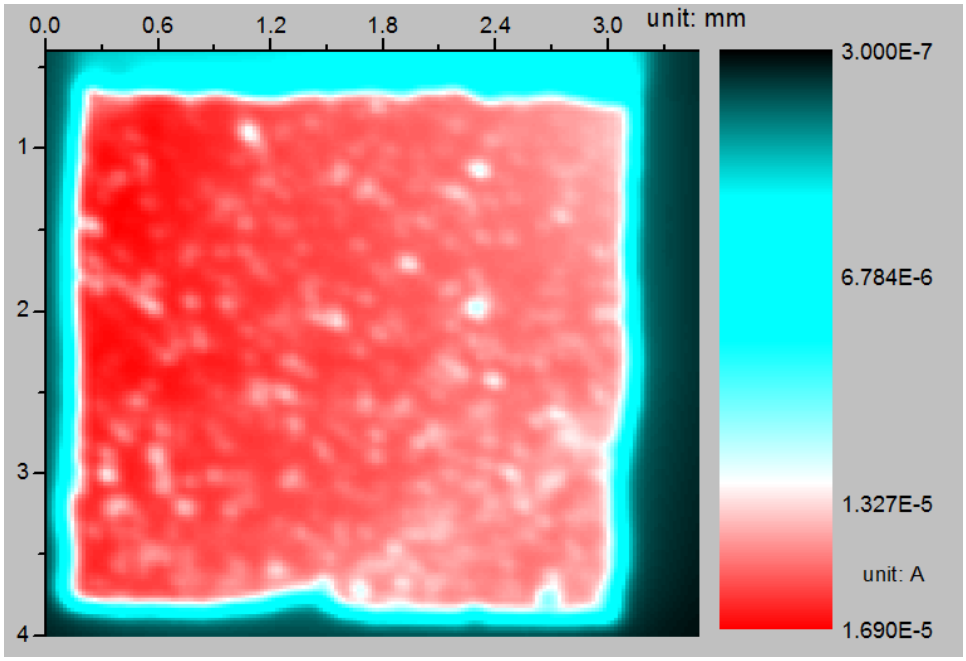

(a)

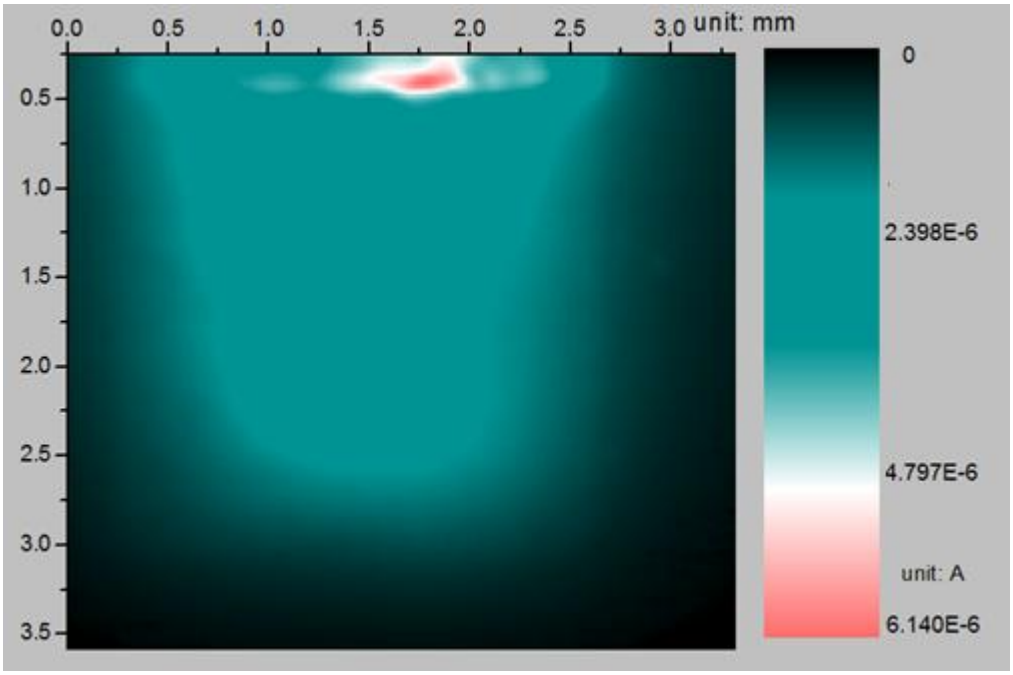

(b)

Figure 7-6: The current mapping of degradation without TiO_x protection (a) as prepared device (b) device after 1 week.

7.4 Conclusion

2D images of the local photocurrent in cells with and without TiO_x protection layers were obtained by LBIC measurements. Degradation spots were observed in devices. The enhancement of the degradation spots were observed with time in all the cells. However, the shrinkage of the active area from the edge was observed only in the OSC without TiO_x. The results show that the introduction of the TiO_x layer could effectively absorb water/oxygen from ambient air and protect the cells at the edge and top.

Chapter 8. A study on doping of TiO_x thin films

8.1 Introduction

Current problem

The enhancement of efficiency and long term stability of organic solar cells by TiO_x has been demonstrated in our previous study. However, the electrical resistance of such films is still high and may affect the conversion efficiency. The series resistance of the organic solar cell changes due to insertion of this additional TiO_x layer. [101] In our experiment, we explored method to reduce the series resistance of OSC after adding TiO_x layer. It has been demonstrated that the properties of metal oxides can be enhanced and tuned through the addition of various dopants and processing methods [103]. We have investigated the doping of TiO_x to improve performance of OSC.

Choice of dopant

The dopant must be compatible with sol-gel process employed in synthesis of the TiO_x precursor. The doped TiO_x should be prepared by wet chemical synthesis and should be highly soluble in methanol, which is used to dilute TiO_x precursor.

Cesium and Fe dopant

Cesium carbonate (Cs_2CO_3) has been widely incorporated for electron injection and transport enhancement in organic devices [102,103], usually as an n-type dopant in organic electron-transport films. Doped nanocrystalline TiO_2 prepared by adding a Cs_2CO_3 has been reported [104]. The interfacial TiO_2: Cs layer facilitates electron transport from the active layer to the cathode. Therefore the series resistance can be expected to decrease.

Another way to modify the electrical properties of is to introduce defects into the TiO_2 lattice by doping with transition metals, e.g. Fe(III). It is generally accepted that Fe(III) centers form shallow charge trapping sites with the TiO_2 matrix as well as on the particle surface through the replacement of Ti(IV) by Fe(III) [105], as shown in Figure 8-1. The trapping site will reduce the e - h recombination rate as electron transfers from the trapping site to molecular oxygen more rapidly than the undoped TiO_2.

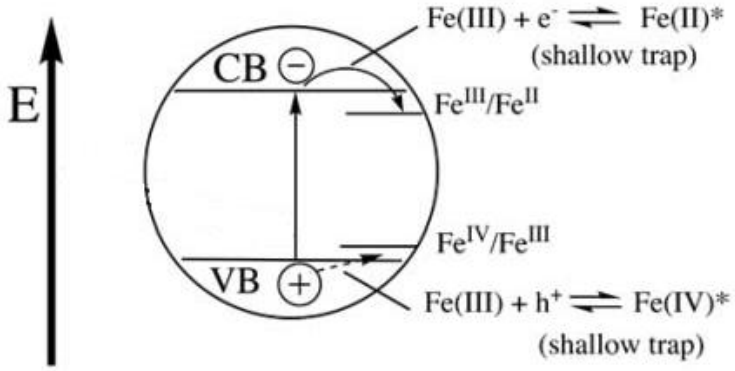

Figure 8-1: Energy level of TiO_2 changes after Fe doping, From C.-Y. Wang et. al 2003

The sol-gel method has been widely used for preparation of Fe-doped TiO_2 from $TiCl_4$ or titania alkoxide (TiO_x) and an iron precursor like $FeCl_3$, $Fe(NO_3)_3$ $9H_2O$ or Fe(III)-acetyloacetonate [106]. Since Fe (III)-acetyloacetonate is soluble in methanol, it was chosen as Fe dopant.

We have explored the application of novel TiO_x thin films doped with Cs_2CO_3 for OSC applications. We also noted the effect of doped TiO_x films on OSC device parameters like efficiency, open circuit voltage, short circuit current and fill factor.

8.2 **Experiment**

8.2.1 TiO_x precursor doping

The TiO_x precursor was synthesized according to previous chapter.

Because, as previously noted, Cs_2CO_3 has a high solubility in methanol. Thus, the doping of Cs_2CO_3 is compatible with the solution processing of TiO_x sol gel. Cs_2CO_3 was dissolved in methanol for the purpose of this experiment. TiO_x precursor was diluted to 1 % before mixing. Then the solutions of Cs_2CO_3 of different concentration were mixed with TiO_x sol-gel and mixing ratio was 1:1 by volume to dope TiO_x precursor.

Fe (III)-acetyloacetonate also has a high solubility in methanol. In this experiment, Fe (III)-acetyloacetonate was dissolved in methanol. Then the solutions of Fe (III)-acetyloacetonate of different concentration were mixed with TiO_x sol-gel at the ratio of 1:1 by volume to dope TiO_x precursor.

The solution of Fe (III)-acetyloacetonate is yellowish at low concentration (less than 1 %) and becomes reddish with the increasing Fe concentration. The Cs_2CO_3 solution is transparent.

8.2.2 Resistivity measurement

The resistivity of the TiO_x and doped TiO_x was measured by the structure shown in Figure 8-2. Two Al electrodes, 1 cm in length, were deposited on the top of insulating glass material by e-beam evaporation. The distance between two electrodes was 150 μm. The thickness of the electrode was 100 nm. TiO_x precursor was spin coated on the glass with Al electrode to a thickness of more than 100 nm, measured using a Veeco Dektak 8

stylus profilometer. Electrical measurements were made using HP 4145B semiconductor parameter analyzer.

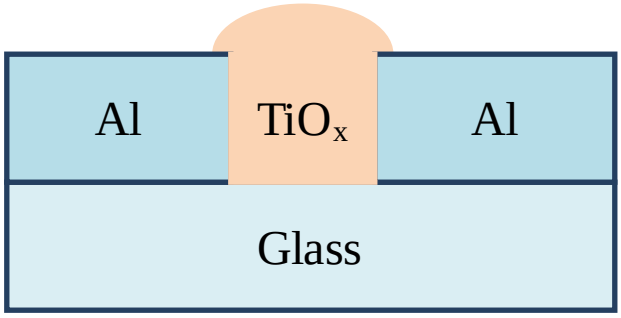

Figure 8-2: TiO_x between to electrodes to measure the resistivity

8.2.3 Organic solar cell fabrication

The fabrication of organic solar cell follows the recipe of previous chapters. Doped TiO_x precursor is made by mixing TiO_x precursor and the doped methanol solution. After coating of the active PCBM/P3HT layer, the doped precursor was spin-coated on the top of active layer. Doping did not change the wetting property of the TiO_x precursor. The coated device was soft baked on the 80 °C hot plate in air. Then Al electrodes were deposited using e-beam and the device was thermally annealed in vacuum for 2 minutes at 130 °C.

8.3 Results and discussion

8.3.1 Fe doped TiO_x

The photovoltaic parameters of devices of different doping levels are listed in Table 8-1.The TiO_x thin film thickness was optimized to obtain the highest efficiency. The data in the table is the average of optimized devices on one substrate.

The short circuit current is higher for the device with doped and undoped TiO_x due to enhancement of light absorption generated by the spacer layer. The device with doped TiO_x shows 5 % improvement than the devices with undoped TiO_x. Fill factor increases to around 8 % while the series resistance reduces by 9 %. Because Fe doping reduces the resistivity of TiO_x, which facilities the carrier transportation, therefore the current and fill factor improved upon doping. Fe doping also affects the energy level alignment because the open circuit voltage reduces compared with undoped TiO_x. The overall efficiency is 11 % higher for doped TiO_x.

Table 8-1 The photovoltaic parameters of devices with Fe doped TiO_x

Samples	V_{oc} (V)	J_{sc} (mA/cm^2)	Efficiency (%)	FF (%)	Rs ($ohm*cm^2$)
Reference	0.696	5.24	1.82	49.8	29
with TiO_x	0.708	7.17	2.36	46.5	24
TiO_x with 1 % F_e	0.687	7.54	2.62	50.6	22

Figure 8-3 shows the I-V curve of device with TiO_x of 1 % Fe doping. It is clear that Fe doping changes the short circuit current and open circuit voltage of the devices.

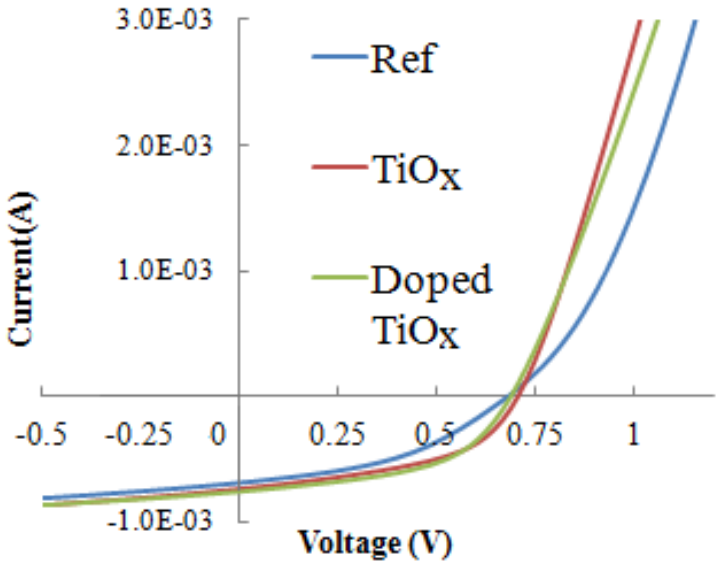

Figure 8-3 : I-V curve of device with 1 % Fe doped TiO_x under 1 sun light illumination. Ref stands for devices without TiO_x, TiO_x and doped TiO_x stand for devices with original TiO_x and doped TiO_x material, respectively

The resistivity of Fe doped TiO_x material is shown in Figure 8-4. The resistivity value is the average of 3 samples. It is observed that the resistivity of TiO_x material starts to reduce with increase of Fe doping. The resistivity decreases about 30 % with 1 % Fe doping. But the resistivity increases with more Fe doping. Therefore we can conclude that Fe doping slightly reduces the resistivity of TiO_x material.

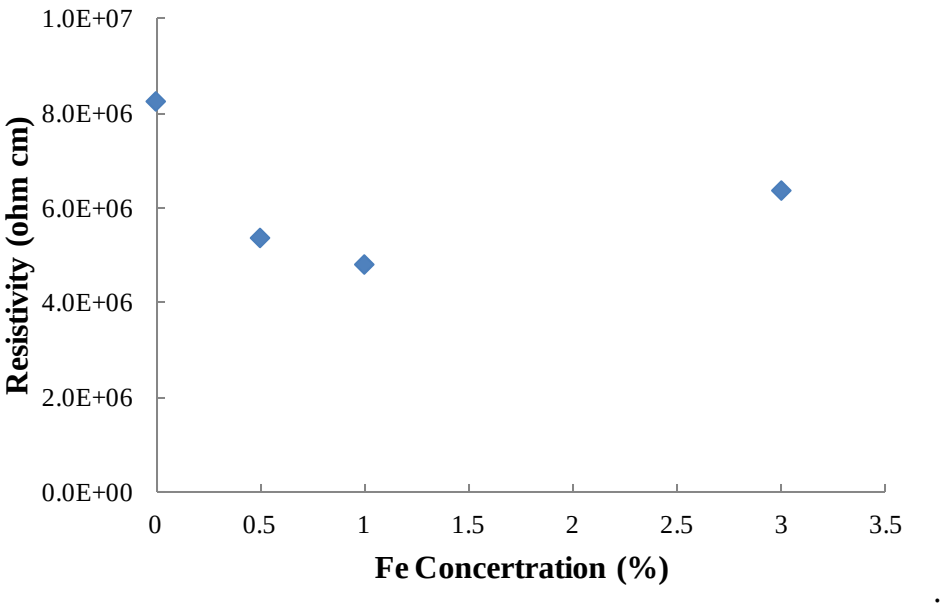

Figure 8-4: The resistivity of TiO_x material upon doping with Fe of different concentration

8.3.2 Cs doped TiO_x

Figure 8-5 shows the I-V curve of device with TiO_x of different Cs doping level in dark. It shows that doping with Cs reduces the resistance in the 0~1 V region. But the reverse current also increased for highly doped TiO_x.

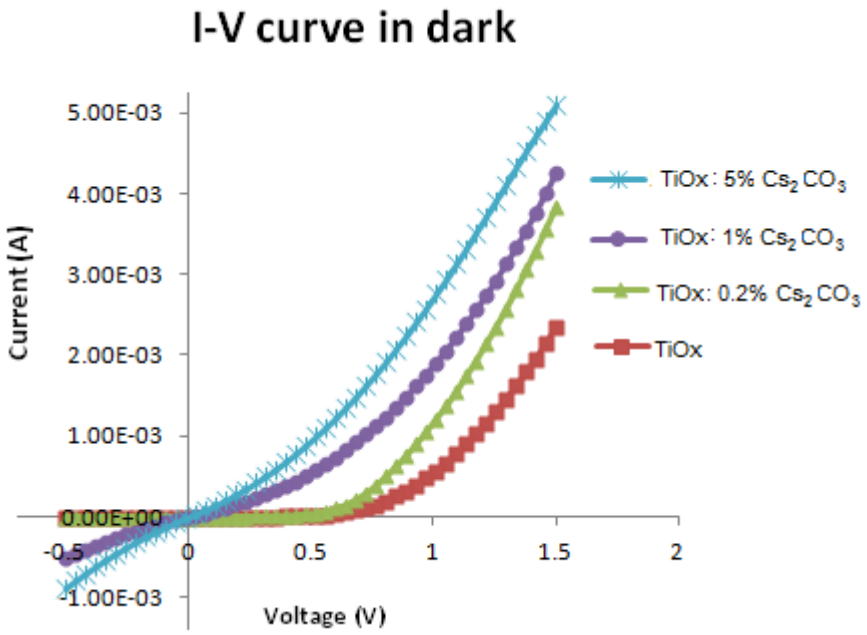

Figure 8-5 : I-V curve of device with 1% TiO_x of different Cs doping level.

The photovoltaic parameters of devices of different doping levels are listed in Table 8-2. The short circuit current is higher due to enhancement of light absorption generated by the space layer. The open circuit voltage is lower due to the possibility of energy level alignment modified by Cs doping. The overall performance for doped TiO_x material does not show significant improvement compared with undoped TiO_x. Therefore Cs doping does not improve the TiO_x for organic solar cells.

Table 8-2: Photovoltaic parameters of devices of different doping levels at various TiO_x concentration levels

Samples	V_{oc} (V)	J_{sc} (mA/cm^2)	Efficiency (%)	FF (%)
References sample	0.7	2.15	0.51	34
TiO_x only	0.48	3.34	0.61	38
TiO_x: 0.2 % Cs_2CO_3	0.51	3.04	0.6	39
TiO_x: 0.05 % Cs_2CO_3	0.51	1.53	0.26	33
TiO_x: 1 % Cs_2CO_3	0.14	0.73	0.03	26

8.4 Conclusion

In this chapter, we investigated the effect of Cs and Fe doping on the TiO_x properties. Device with Cs doped TiO_x does not show improvement on the photovoltaic performance whereas Fe does demonstrated doping improved series resistance, fill factor and short circuit current; therefore the power conversation efficiency improved by 11 %.

Chapter 9. TiO_x thin films as surface passivation and anti-reflection coating for silicon solar cells

9.1 Introduction

In this chapter, we first study the optical properties of TiO_x thin films on polished and chemically textured silicon surfaces. We then evaluate the properties of silicon solar cells with TiO_x thin films using the conventional solar cell fabrication process. We then study the surface passivation effect of these films by near-surface lifetime measurement technique [107].

9.2 Experiment

The TiO_x solution was spin-coated on p- and n-type Cz Si (100) with $\rho = 1\ \Omega$ cm and the bulk minority carrier lifetime > 500 μs. Chemically textured silicon surfaces were prepared using tetramethylammonium hydroxide (TMAH) solution [108]. Optical reflection measurements were carried out using a Filmetrics thickness measurement tool. Integrated reflection measurements were made by a spectrophotometer attached with an integrating sphere with incident angle of 35 °. The 80 °C annealing process was performed on hot plate in air. The 400 °C annealing process was performed in the RTA system using forming gas for 20 minutes.

Silicon solar cells were prepared on polished and chemically textured surfaces as shown in Figure 9-1[46].

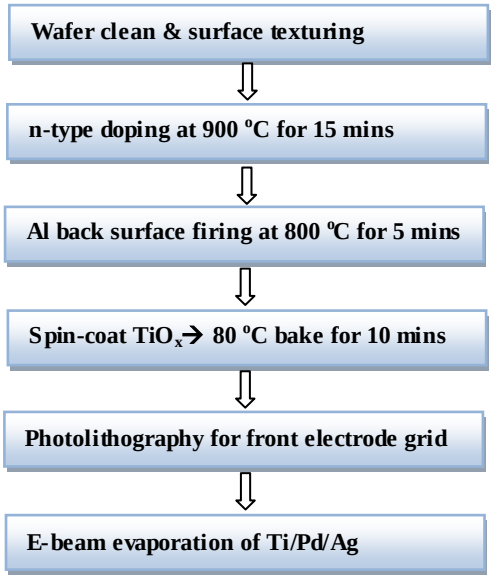

Figure 9-1: Process flow for fabricating silicon solar cells [46]

I–V measurements are carried out using solar simulator. Quantum efficiency is measured using an IV setup and a tungsten halogen lamp. A 270M Jobin Yvon monochromator was used to get individual wavelengths.

Near-surface lifetime was measured by a technique based on photoconductive decay (PCD) method. Figure 9-2 shows the experimental set-up for measuring the surface lifetime of TiO_x thin films spin-coated on Si substrate. The TiO_x thin films were then patterned using photo lithography. Two windows were opened up in the TiO_x thin films in order to make electrical contact with the wafer. The focused laser beam is illuminated between the contacts. The decay across the resistor is monitored on an oscilloscope.

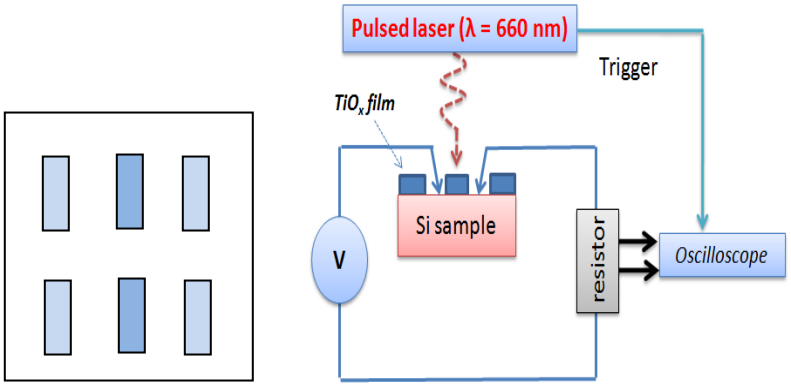

(a) (b)

Figure 9-2: (a) Pattern and (b) experimental set-up for surface lifetime measurement [46]

9.3 Results and discussion

9.3.1 Optical measurement

In chapter 3, we demonstrated that the Si reflection values from TiO_x coating are comparable to the values of conventional silicon nitride. Figure 9-3 shows that TiO_x films are able to reduce the reflection to about 5 % for chemically textured silicon surfaces.

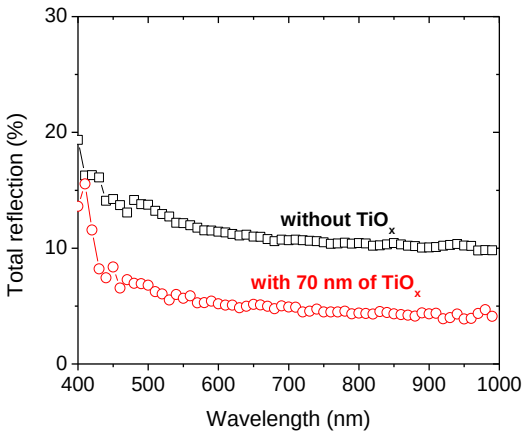

Figure 9-3: Total integrated reflection for a chemically textured surface with and without TiO_x films [46]

9.3.2 Photovoltaic device characterization

Si solar cell devices were fabricated on a polished p-type substrate with a phosphorus emitter. The device structures for Si solar cells with TiO_x layer only and for solar cells with SiO_2 and Si_3N_4 layers are shown in Figure 9-4. The obtained photovoltaic performance parameters are listed in Table 9-1. It can be seen that the performance of device with TiO_x as anti-reflection and passivation layer are comparable to the one using SiO_2 and Si_3N_4 layers.

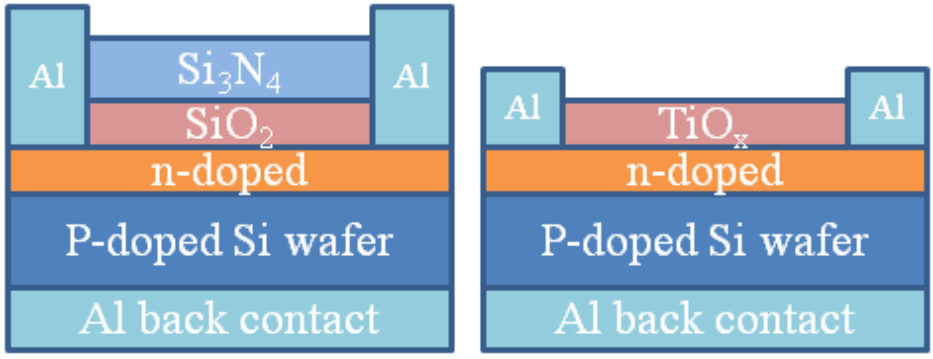

Figure 9-4: Device structures for Si solar cells with (a) SiO_2 and Si_3N_4 layer and (b) TiO_x layer

Table 9-1: Device performance for the Si solar cells with TiO_x layer and SiO_2 and Si_3N_4 layers

	Efficiency (%)	V_{oc} (mV)	J_{sc} (mA/cm^2)	Fill Factor
with TiO_x	15.74	606.8	33.72	76.92%
SiO_2+Si_3N_4	14.9	605	34.8	70%

The I-V characteristic curve and external quantum efficiency of the solar cells with TiO_x coatings are shown in Figure 9-5.

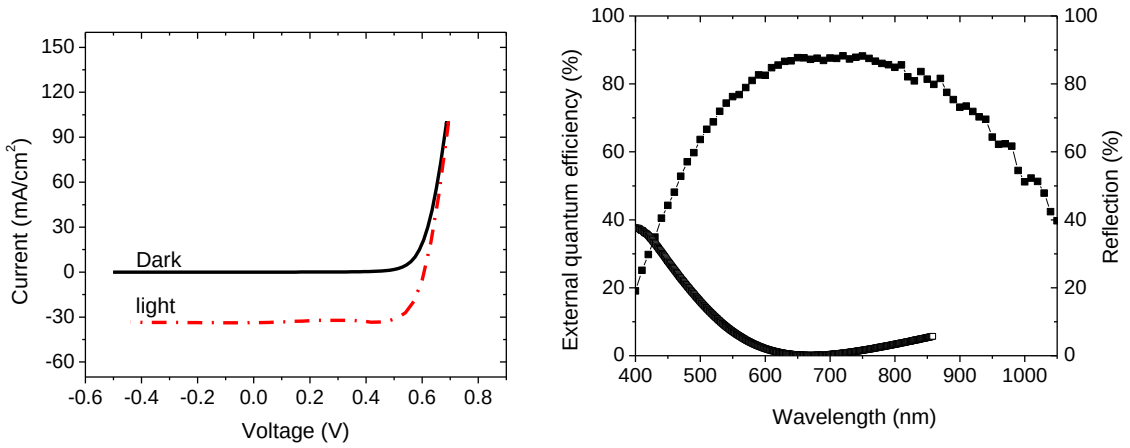

(a) (b)

Figure 9-5: (a) Dark and light I-V curves and (b) external quantum efficiency and reflection curves for Si solar cells with TiO_x thin films as the surface passivation and anti-reflection coating[46]

The results of the devices with chemically textured surfaces, which also has TiO_x thin films as the surface passivation and anti-reflection coating, is shown in Figure 9-6. Compared with polished device, the textured device shows a 4 % reduction in the open circuit voltage and a 7 % drop in fill factor. The reduction in open circuit voltage may be attributed to the coating for textured structure is not as well as the coatings on polished surface. The quantum efficiency of the textured device is more flat than that of the polished one. It can be attributed to the reflection curves also shown on the right axis.

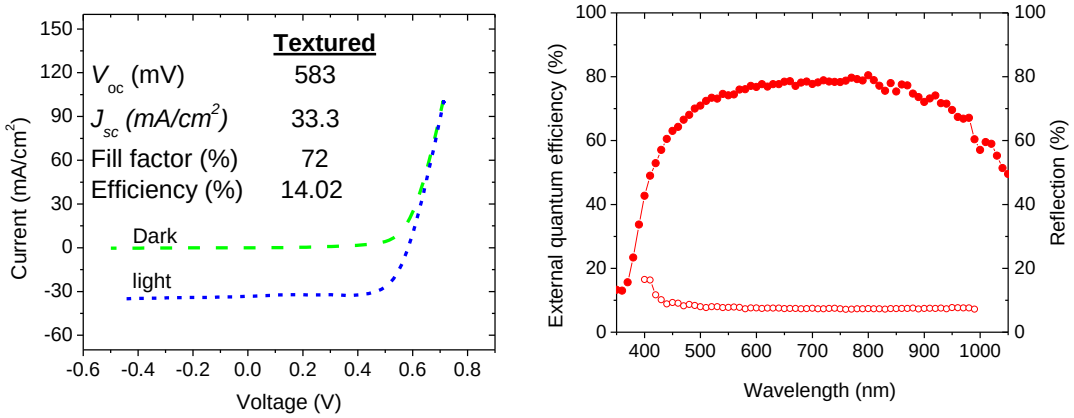

Figure 9-6: (a) Dark and light I-V curves and (b) external quantum efficiency and reflection curves for Si solar cells with TiO_x thin films as the surface passivation and anti-reflection coating on chemically textured surface [46]

9.3.3 Surface passivation

PCD method is useful for characterizing the near-surface regions of semiconductors. PCD measures an effective minority carrier lifetime given by

$$\frac{1}{\tau_{\text{effective}}} = \frac{1}{\tau_{\text{surface}}} + \frac{1}{\tau_{\text{bulk}}}$$

Where τ_{bulk} is the bulk lifetime, $\tau_{surface}$ is the surface lifetime, $\tau_{effective}$ is the effective lifetime. The surface treatment will not change τ_{bulk}, so any observed change in $\tau_{effective}$ is correlated to a change in the surface electrical properties. $\tau_{effective}$ is predominantly determined by $\tau_{surface}$ for a thin sample region, and the bulk contribution does not need to be known.

The optical absorption coefficient for Si is 2.5×10^3 cm^{-1} at a wavelength of 658 nm, and the light penetration depth (α^{-1}) is approximately 4 μm. Hence, using λ= 658 nm, the minority carrier lifetime is measured in a substrate region within 4 μm from the

surface of the wafer. The measured properties should be heavily influenced by the characteristics of the surface.

The principle of PCD technique is based on excess carriers injected by the illumination pulse, which increase the conductivity of the Si by

$$\Delta\sigma = q(\mu_n \Delta n + \mu_p \Delta p)$$

where $\Delta\sigma$ is the increase in conductivity (photoconductivity), q is the electron charge, μ_n is the electron mobility, μ_p is the hole mobility, and Δn and Δp are excess electron and hole concentrations respectively.

Assuming $\Delta n = \Delta p$, then $\Delta\sigma$ is proportional to a change in Δn (or Δp). If we also assume that the carrier decay time, governed by the carrier lifetime τ, is given by

$$\Delta n(t) = \Delta n(0) e^{(-\frac{t}{\tau_{eff}})}$$

Then the slope of the semi-log curve of $\Delta n(t) / \Delta n(0) - t$ plots would be

$$Slope = \frac{d \ln(\Delta n(t))}{dt} = \frac{\ln(10) d \log(\Delta n(t))}{dt} = -\frac{1}{\tau_{eff}}$$

Taking the linear portion of the plot gives τ_{eff} . The voltage decay is proportional to the excess carrier density [109]. The initial decay of the PCD signal is linear on a semi-log plot and is representative of the surface component.

We studied the passivation effect of TiO_x layer by comparing with samples without any passivation layer and samples with SiO_2 as passivation layer. The results are shown in Figure 9-7. Figure 9-7 (a) shows the passivation on n-type wafer, Figure 9-7 (b) shows the passivation on p-type wafer. The near surface life time is 60 μs for n-type wafer without any passivation. The TiO_x layer increases the near-surface carrier lifetime

to 80 µs for both n-type and p-type wafers. Therefore, TiO_x layer effectively passivated the Si surface. It is not as effective as SiO_2 passivation layer for n-type wafer. The passivation could be due to the charge accumulation at the Si/TiO_x interface [110].

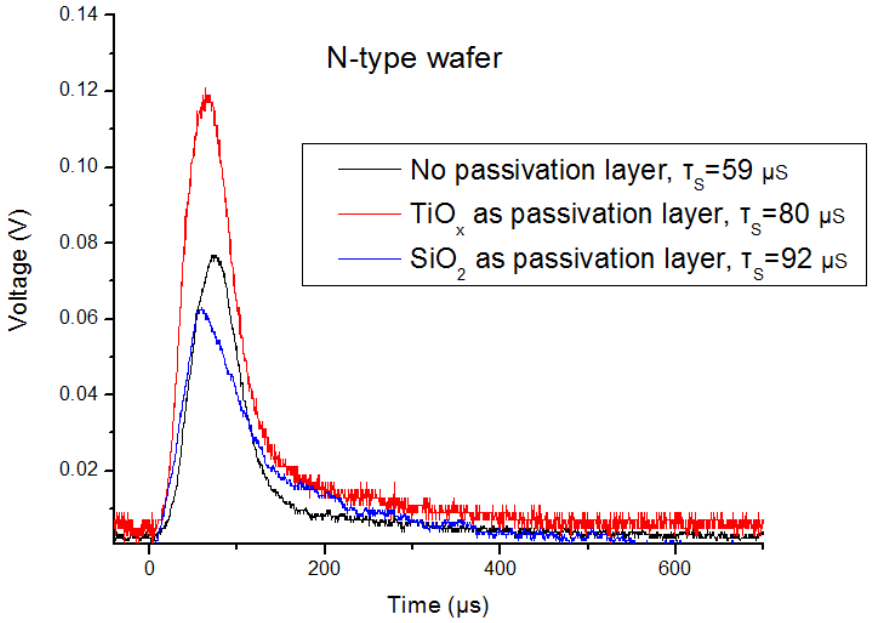

(a) N-type wafer

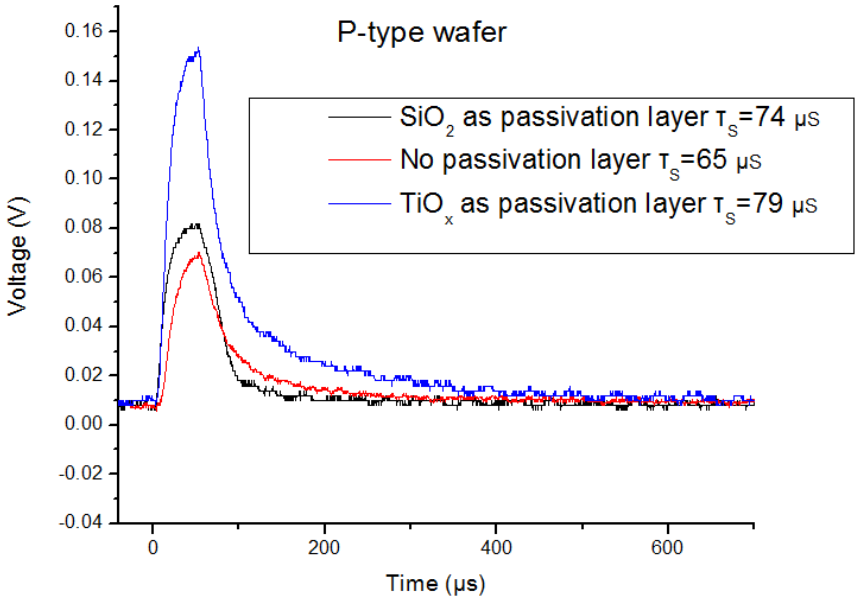

(b) P-type wafer

Figure 9-7: (a) The passivation on n-type wafer, (b) The passivation on p-type wafer,

9.4 Summary

In summary, we have successfully demonstrated TiO_x thin films as surface passivation and anti-reflection coatings for silicon solar cells. We report the results of TiO_x thin films as anti-reflection coating and surface passivation layers for polished as well as textured silicon solar cells. Silicon solar cells fabricated with TiO_x thin films for ARC and surface passivation showed an efficiency of 15.7 %. Surface passivation quality is evaluated by near-surface lifetime technique .The TiO_x layer increases the near-surface carrier lifetime to 80 μs.

Chapter 10. **Summary and future work**

10.1 Summary

In this dissertation, we explored a novel TiO_x material for low cost photovoltaic applications. The fundamental properties, including optical, electrical, structural, and morphological were studied. The TiO_x photochemically activated protection mechanisms for organic solar cells were investigated using electrical and chemical methods. Laser beam induced mapping technique was used to explore the local degradation of the devices. Cs and Fe doping of the TiO_x thin films were examined for improving the material properties. TiO_x material has also been demonstrated to be an effective anti-reflection and passivation layer for Si solar cells. The passivation effects were evaluated by near surface carrier life time measurements.

Refractive index of the TiO_x thin films was calculated using a three-layer model incorporating the ellipsometrical method. At the wavelength of 600 nm, the obtained refractive index ranges from 1.77 to 2.57 depending on the annealing temperature. The range can be explained by the changes in the crystalline structure, the difference of surface morphology and the increase of the packing density of the films as indicated by SEM, AFM and XRD results. The high refractive index and high transmission in the visible spectrum indicate sol-gel TiO_x films may be useful in optical thin films applications as antireflection layer.

The bulk resistivity of as-deposited TiO_x thin films was found to be 1.5×10^7 Ω·cm. Thermal annealing decreases the resistivity. The resistance of Al/TiO_x/ITO structure is stable for temperature from 20 ℃ to 140 ℃.

We studied the stabilization behavior of P3HT/PCBM organic solar cells under air and UV irradiation using TiO_x protection layer. Significant improvements were observed with TiO_x layer protection from the data on the degradation of solar cell performance under air and UV exposure. The protection mechanism was also investigated by transmission IR and ESR spectroscopy. The results of this study suggest a photochemically activated protection mechanism. The photooxidation of the bound organic moieties causes oxygen gas scavenging when excited by UV photons. Around 10% UV energy in the standard solar irradiation was absorbed by the TiO_x layer.

2D images of the local photocurrent in the cells with and without TiO_x protection layers were obtained by LBIC measurements. Degradation spots were observed in various organic solar cells. Enhancement of the degradation spots was observed from all the cells, but the shrinkage of the active area from the edge was observed only in the organic solar cells without TiO_x. The results show that the introduction of the TiO_x layer could effectively absorb water/oxygen from ambient air and protect the cells at the edge of the devices.

We explored the applications of these TiO_x thin films doped with Cs_2CO_3 and Fe for organic solar cells applications. Initial results show that Fe doping could reduce the series resistance of the organic solar cells. Thus, the power conversion efficiency increases around 10% compared to devices with undoped TiO_x. The results of the effect of doped TiO_x films on organic solar cells parameters like efficiency, open circuit voltage, short circuit current and fill factor were presented. The variation of resistances for the organic solar cells with TiO_x material of different Cs_2CO_3 doping concentrations was reported.

We have successfully fabricated silicon solar cells using TiO_x thin films for surface passivation and anti-reflection coatings. We made silicon solar cells with TiO_x on polished as well as textured surfaces. The devices showed an efficiency of 15.7 %, which is comparable with Si solar cells using SiO_2 and Si_3N_4 as passivation and anti reflection layers, respectively. Surface passivation quality was evaluated by the near-surface lifetime technique and we obtained a maximum value of 80 μs for n-type Cz-Si wafers.

10.2 Future work

TiO_x material has been demonstrated as an effective optical spacer and protection layer, and the material properties have been studied and modified. However, TiO_x material may have further applications with new structures or dopants. For example, it could be used in organic solar cells on new textured structures to alleviate the non-conformal problem. The stability of organic solar cells may be improved further using a combination of TiO_x and a stable hole transport layer other than PEDOT: PSS. The carrier transport and passivation effects may be improved through other dopants. We will discuss future work in the following sections:

10.2.1 Optical absorption enhancement by textured structure

As discussed in the previous chapter, in P3HT: PCBM material system, there is a mismatch between optical absorption length (>100 nm) and average distance for charge transport (~10 nm). It is highly desired to develop new methodologies that can enable efficient optical absorption in films thinner than the currently used (100 nm) and to reduce series resistance.

Textured substrates for improved light trapping are common in traditional inorganic solar cells. They utilize the effect of multi-reflection by roughening the entrance interface and randomizing the light propagation direction, which results in a much longer optical path length at the surface and hence a substantial absorption enhancement. Realizing organic solar cells on such topographies provides an efficient way to achieve light-trapping without compromising the electrical characteristics.

However, textured substrates have not been successfully applied to polymer-based organic solar cells. Enhancement in optical absorption was demonstrated in different patterning schemes, for example, grating-type organic solar cells [111], V-shape organic solar cells built by mounting two cells together, [112] microprism substrates, [113] and azopolymer-based sub-micrometer topography substrate[114] have been reported. Efficient OSC cells could not be realized due to the processing bottlenecks of solution-processing nano-scale thick and conformal active layers on topographical surfaces. Attempts to spin-coat active-layer on textured substrates led to over filling of the valleys and shunts at the crests, which severely affected the device performance, as shown in Figure 10-1:

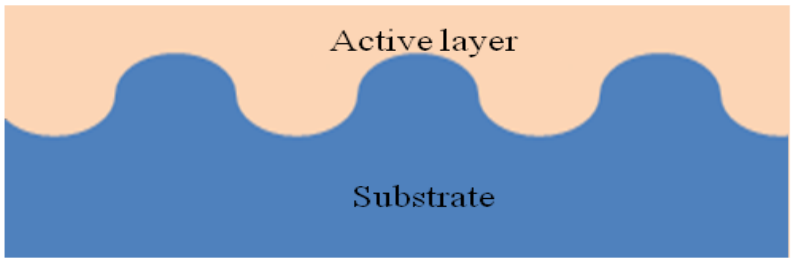

Figure 10-1: Non-conformal coating on top of textured substrate

It has been demonstrated [115] that a TiO_x spacer layer benefits a thin active layer, but it is less effective with an optimized thick active layer. If a TiO_x spacer layer were

used in organic solar cells coated on the textured surface, as shown in Figure 10-2, it is possible to get high efficiency in both the thin and thick area. In the thick coating area, the device keeps high efficiency. In the thin coating area, the spacer layer will enhance the optical absorption; therefore the efficiency will increase the efficiency. The overall efficiency of the cell may not decrease.

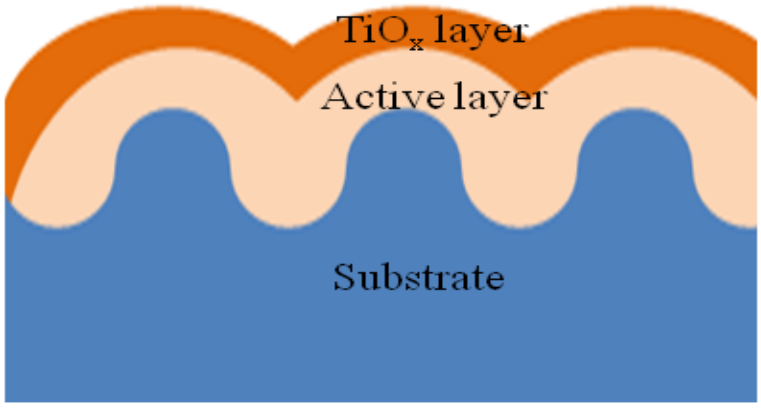

Figure 10-2: TiO_x on the top of the non-conformal coating on textured substrate

10.2.2 Further improvement from degradation

In typical OSC devices, PEDOT: PSS is commonly used as the hole transport layer. But the use of PEDOT: PSS induces numerous problems; among them is its tendency to absorb atmospheric water, which contributes to significant degradation or performance reduction of the device. Therefore, alternatives to PEDOT: PSS have been intensively studied, such as graphene oxide [116], nickel (II) oxide (NiO) and so on. [117]

Soo Young Kim et. al demonstrated that OSC with ~3 nm graphene oxide hole extraction layers exhibits increased power conversion efficiency[116]. J. R. Manders et.al fabricated high efficiency OSCs with efficiency comparable to PEDOT: PSS-based devices using nickel oxide hole transport layers [117]. The unencapsulated NiO-based

devices show a 300% improvement over PEDOT: PSS-based devices in the maintaining >50% of the original efficiency with time.

We demonstrated that TiO_x extends the lifetime of the OSC with a PEDOT: PSS layer. It could effectively prevent degradation from the edge of the OSC, which is probably due to water absorption of the PEDOT: PSS layer.

The stability of the device with TiO_x and nickel oxide instead of PEDOT: PSS may be improved further because of the double protection from both sides of the active layer, as shown in Figure 10-3. It would be of interest to test this new device. The protection of combining TiO_x and graphene oxide could also be explored.

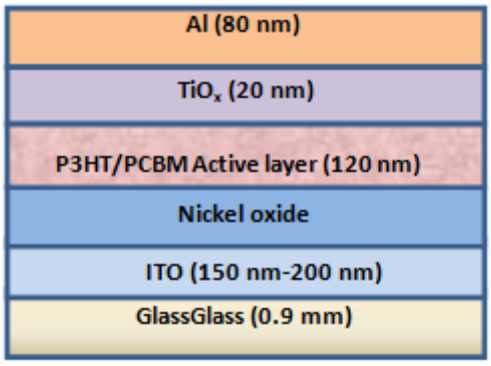

Figure 10-3: Proposed structure of device with TiO_x and nickel oxide protection layer

10.2.3 TiO_x material property tuning

We explored the effects of Cs and Fe doping on the performances of the organic solar cells. It has been demonstrated**Error! Bookmark not defined.** that the properties of metal oxides can be tuned through the addition of various dopants and processing methods other than Cs and Fe doping.

Several approaches for TiO_2 modification have been proposed: metal-ion doped TiO_2 (using transition metals: Cu, Co, Ni, Cr, Mn, Mo, Nb, V, Fe, Ru, Au, Ag, Pt) [118,119,120], non-metal doped-TiO_2 (N, S, C, B, P, I, F) [121, 122, 123], and TiO_2 doped with an upconversion luminescence agent [124]. The introduction of dopants offers a convenient method for producing functional materials.

Therefore, it is of interest to explore the effects of other dopants that may facilitate the carrier transport and the lifetime of the organic solar cell devices. Also, the passivation for the Si solar cell by TiO_x material may be affected by the doping. Doping induces different energy levels and charge compositions, which will affect the passivation.

Appendix

Publications:

1. J. Li, A. M. DeBerardinis, L. Pu and M. C. Gupta, Optical properties of solution processable semiconducting TiO_x thin films for solar cell and other applications, Applied Optics,51,1131-1136,2012
2. J. Li, L. Pu and M. C. Gupta, Optical and electrical properties of solution processable TiO_x thin films for solar cell and sensor applications, MRS Proceedings, 1352, 75-79, 2012
3. J. Li, S. Kim, S. Edington, J. Nedy, S. Cho, K. Lee, A. J Heeger, M. C. Gupta, and J. T. Yates Jr, A study of stabilization of P3HT/PCBM organic solar cells by photochemical active TiO_x layer, Solar Energy Materials and Solar Cells, 95, 1123-1130, 2011
4. J. Li, V. V. Iyengar, and M. C. Gupta, Solution processable semiconducting TiO_x thin films for low cost solar cell applications (submitted to MRS Proceedings)
5. V. V. Iyengar, J. Li and M. C. Gupta, Solution processable TiOx thin films as surface passivation and anti-reflection coating for silicon solar cells (to be submitted)
6. J. Li, A. M. DeBerardinis, L. Pu and M. C. Gupta, A study on electrical resistivity of solution processable TiOx thin films (to be submitted)

Presentations:

1. J. Li, V. V. Iyengar, and M.C. Gupta, Solution processable semiconducting TiOx thin films for low cost solar cell applications, MRS spring meeting 2012, San Francisco, CA, 2012
2. J. Li, L. Pu and M. C. Gupta; "Optical and Electrical Properties of Solution Processable TiOx Thin Films for Solar Cell and Sensor Applications, MRS spring meeting 2011, San Francisco, CA, 2011

References

[1] C. J. Brabec, V. Dyakonov, J. Parisi, N. S. Sariciftci, Organic Photovoltaics: Concepts and Realization, Springer, 2003

[2] National Renewable Energy Laboratory (NREL), 2010 Solar Technologies Market Report, 2010

[3] L. Dou, J. You, J. Yang, C. Chen, Y. He, S. Murase, T. Moriarty, K. Emery, G. Li and Y. Yang, Tandem polymer solar cells featuring a spectrally matched low-bandgap polymer. Nature Photon, 6, 180–185, 2012

[4] K. Lee, J. Y. Kim, S. H. Park, S. H. Kim, S. Cho, A. J. Heeger, Air-stable polymer electronic devices, Adv. Mater.,19, 2445-2449, 2007

[5] S. Cho, K. Lee, A. J. Heeger, Extended lifetime of organic field-effect transistors encapsulated with titanium sub-oxide as an active passivation/barrier layer, Adv. Mater., 21, 1941-1944 , 2009

[6] J. Y. Kim, S. H. Kim, H. H. Lee, K. Lee, W. Ma, X. Gong, A. J. Heeger, New architecture for high efficiency polymer photovoltaic cells using solution based titanium oxide as an optical spacer, Adv. Mater., 18, 572-576 , 2006

[7] W. Calderon, Titanium dioxide: A primer on the compound named for the mythical mothers and fathers of earth, IEEE Potentials, 14, 13–16, 1995

[8] N. Nobuhiro, S. Mitsunori, M. Mitsunobu, B. Nobuyoshi and S. Naruhito, TiO_2–SiO_2 based glasses for infrared hollow waveguides, Appl. Opt., 30, 1074-1079, 1991

[9] J. Barbé, A. F. Thomson, E. Wang, K. McIntosh, K. Catchpole, Nanoimprinted TiO_2 sol–gel passivating diffraction gratings for solar cell applications, Progress in Photovoltaics: Research and Applications, 20, 143–148, 2012

[10] C. Euvananont, C. Junin, K. Inpor, P. Limthongkul, C. Thanachayanont, TiO_2 optical coating layers for self-cleaning applications, Ceramics International, 34, 1067-1071, 2008

[11] S. Lin, S. Chen, Y. Hung, TiO_2 nanoceramic films prepared by ion beam assisted evaporation for optical application, Ceramics International, 35, 1581-1586, 2009

[12] S.H. Toma, H. E. Toma, Versatile electrochromic displays based on TiO_2 nanoporous films modified with triruthenium clusters, Electrochemistry Communications, 8, 1628-1632, 2006

[13] A. Szeghalmi, M. Helgert, R. Brunner, F. Heyroth, U. Gösele, M. Knez, Atomic layer deposition of Al_2O_3 and TiO_2 multilayers for applications as bandpass filters and antireflection coatings, Appl. Opt., 48, 1727-1732, 2009

[14] B. S. Richards, J. E. Cotter and C. B. Honsberg Enhancing the surface passivation of TiO_2 coated silicon wafers, Appl. Phys. Letters, 80, 1123-1125, 2002

[15] M. Taguchi, K. Kawamoto, S. Tsuge, T. Baba, H. Sakai, M. Morizane, K. Uchihashi, N. Nakamura, S. Kiyama, and O. Oota, HITTM cells - high-efficiency crystalline Si cells with novel structure, Progress in Photovoltaics, 8, 503–513, 2000

[16] B. O'Reagen and M. Gräzel, A low-cost, high-efficiency solar cell based on dye-sensitized colloidal TiO_2 films, Nature, 353, 737-740, 1991

[17] S. Phadke, J. D. Sorge, H. Sherwood, D. P. Birnie, III, Broad band optical characterization of sol–gel TiO_2 thin film microstructure evolution with temperature, Thin Solid Films, 518, 5467–5470, 2010

[18] B. R. Sankapal, M. Ch. Lux-Steiner, A. Ennaoui, Synthesis and characterization of anatase-TiO_2 thin films. Appl. Surf. Sci., 239, 165–170, 2005

[19] P. Eiamchai, P. Chindaudom, A. Pokaipisit, P. Limsuwan, A spectroscopic ellipsometry study of TiO_2 thin films prepared by ion-assisted electron-beam evaporation, Curr. Appl. Phys. 9, 707–712 , 2009

[20] S. Karuuchamy, K. Nonomura, T. Yoshida, T. Sugiura and H. Minoura, Cathodic electrodeposition of oxide semiconductor thin films and their application to dye-sensitized solar cells, Solid State Ionics, 151, 19-27, 2002

[21] P. R. McCurdy, L. J. Sturgess, S. Kohli, E. R. Fisher, Investigation of the PECVD TiO_2–Si (1 0 0) interface, Appl. Surf. Sci., 233, 69-79 , 2004

[22] G. A. Battiston, R. Gerbasi, A. Gregori, M. Porchia, S. Cattarin, G.A. Rizzi, PECVD of amorphous TiO_2 thin films: effect of growth temperature and plasma gas composition, Thin Solid Films, 371, 126-131, 2000

[23] N. Albertinetti and H. T. Minden, Granularity in ion-beam-sputtered TiO_2 films, Appl. Opt., 35, 5620-5625 , 1996

[24] S. R. Kurtz and R. G. Gordon, Chemical vapor deposition of doped TiO_2 thin films, Thin Solid Films, 147, 167–176, 1997

[25] H. K. Ardakani, Electrical and optical properties of in situ hydrogen-reduced titanium dioxide thin films deposited by pulsed excimer laser ablation, Thin Solid Films, 248, 234–239, 1994

[26] S. Zhang, Y. F. Zhu, and D. E. Brodie, Photoconducting TiO_2 prepared by spray pyrolysis using $TiCl_4$, Thin Solid Films, 213, 265–270, 1992

[27] H. Yanagi, Y. Ohoka, T. Hishiki, K. Ajito, and A. Fujishima, Characterization of dye doped TiO_2 films prepared by spray pyrolysis, Applied Surface Science, 113/114, 426–431, 1997

[28] W. Kaewwiset, W. Onreabroy and P. Limsuwan, Effect of annealed temperatures on the morphology of TiO_2 films, Nat. Sci., 42, 340 – 345, 2008

[29] K. Kawano, R. Pacios, D. Poplavskyy, J. Nelson, D.C. Bradley and J. R. Durrant, Degradation of organic solar cells due to air exposure, Sol. Energy Mater. Sol. Cells., 90, 3520-3530, 2006

[30] M. O. Reese, A. J. Morfa, M. S. White, N. Kopidakis, S. E. Shaheen, G. Rumbles, D. S. Ginley, Pathways for the degradation of organic photovoltaic P3HT:PCBM based devices, Sol. Energy Mater. Sol. Cells., 92, 746-752, 2008

[31] S. A. Gevorgyan, M. Jørgensen and F. C. Krebs, A setup for studying stability and degradation of polymer solar cells, Sol. Energy Mater. Sol. Cells., 92,736 -745, 2008

[32] L. M. Doeswijk, H. H. C. de Moor, D. H. A. Blank, H. Rogalla, Passivating TiO_2 coatings for silicon solar cells by pulsed laser deposition, Applied Physics A: Materials Science & Processing, 69, S409-S411, 1999

[33] B. S. Richards, J. E. Cotter, C. B. Honsberg, Enhancing the surface passivation of TiO_2 coated silicon wafers, Applied Physics Letters, 80, 1123, 2002

[34] J. Barbé, A. F. Thomson, E. C. Wang, K. McIntosh, K. Catchpole, Nanoimprinted TiO_2 sol–gel passivating diffraction gratings for solar cell applications, Progress in Photovoltaics: Research and Applications, 20, 143–148, 2012

[35] B. S. Richards, Comparison of TiO_2 and other dielectric coatings for buried-contact solar cells: a review, Progress in Photovoltaics: Research and Applications, 12, 253-281, 2004

[36] G. Crotty, T. Daud, R. Kachare, Front surface passivation of silicon solar cells with antireflection coating, Journal of Applied Physics, 61, 3077-3079, 1987

[37] J. Livage, M. Henry, C. Sanchez, Sol-gel chemistry of transition metal oxides, Progress in Solid State Chemistry,18,1259-341,1988

[38] D. Mardare and P. Hones, Optical dispersion analysis of TiO_2 thin films based on variable-angle spectroscopic ellipsometry measurements, Mater. Sci. Eng., B. 68, 42–47, 1999

[39] M. M. Rahman, G. Yu, K. M. Krishna, T. Soga, J. Watanabe, T. Jimbo, and M. Umeno, Determination of optical constants of sol-gel-derived inhomogeneous TiO_2 thin films by spectroscopic ellipsometry and transmission spectroscopy, Appl. Opt. 37, 691–697, 1998

[40] V. N. Van, S. Fisson, J. M. Frigerio, J. Rivory, G. Vuye, Y. Wang, and F. Abel´es, Growth of low and high refractive index dielectric layers as studied by in situ ellipsometry, Thin Solid Films, 253, 257–261, 1994

[41] J. Li, A. M. DeBerardinis, L. Pu and M. C. Gupta, "Optical properties of solution processable semiconducting TiO_x thin films for solar cell and other applications", Applied Optics,51,1131-1136, 2012

[42] A. R. Forouhi, I. Bloomer, Optical dispersion relations for amorphous semiconductors and amorphous dielectrics, Phys. Rev. B 34, 7018-7026, 1986

[43] D. Mergel, D. Buschendorf, S. Eggert, R. Grammes, and B. Samset, Density and refractive index of TiO_2 films prepared by reactive evaporation, Thin Solid Films, 371, . 218–224, 2000

[44] M. W. Ribarsky, Titanium dioxide (TiO_2) (rutile), in Handbook of Optical Constants (Vol. 1), E. Palik, Ed. 795–804. Academic Press Inc., Orlando, 1985

[45] G. Hass, Preparation, properties and optical applications of thin films of titanium dioxide, Vacuum, 4, 331–345, 1952

[46] V. V. Iyengar, J. Li, and M. C. Gupta, Solution processable TiO_x thin films as anti-reflection and passivation layer for Si solar cells. (Manuscript submitted to IEEE Journal of Photovoltaic)

[47] R. Asahi, Y. Taga, W. Mannstadt and A. J. Freeman, Electronic and optical properties of anatase TiO_2, Physical Review B 61, 7459-7465, 2000

[48] A. K. Hassan, N. B. Chaure, A. K. Ray, A. V. Nabok and S. Habesch, Structural and electrical studies on sol–gel derived spun TiO_2 thin films, J. Phys. D: Appl. Phys., 36, 1120–1125 , 2003

[49] M. S. P. Sarah, M. Z. Musa, M. N. Asiah, M. Rusop, Electrical conductivity characteristics of TiO_2 thin film, International Conference on Electronic Devices, Systems and Applications, Malaysia, 2010

[50] K. Pomoni, A. Vomvas , Chr. Trapalis, Electrical conductivity and photoconductivity studies of TiO_2 sol–gel thin films and the effect of N-doping, Journal of Non-Crystalline Solids, 354, 4448–4457, 2008

[51] Y. Shen, K. Li, N. Majumdar, J. C. Campbell, M. C. Gupta, Bulk and contact resistance in P3HT:PCBM heterojunction solar cells, Sol. Energy Mater. Sol. Cells 95, 2314-2317, 2011

[52] W. Shockley, Research and investigation of inverse epitaxial UHF power transistors, Report No. A1-TOR-64-207, Air Force Atomic Laboratory, Wright-Patterson Air Force Base, Ohio, 1964

[53] R. J. Meyer and E. H. E. Pietsch, Gmelins Handbuch Der Anorganischen Chemie: Titan,vol. 41, Verlag Chemie, Weinheim, 1951

[54] J. Li, L. Pu and M. C. Gupta, Optical and electrical properties of solution processable TiO_x thin films for solar cell and sensor applications, MRS Spring Meeting, San Francisco, April 2011

[55] B. R. Weinberger, M. Akhtar, S. C. Gau, Polyacetylene photovoltaic devices, Synth. Met., 4, 187-197, 1982

[56] C. W. Tang, US Patent 4,164,431, August 14, 1979 C.W. Tang,

[57] C. W. Tang, Two-layer organic photovoltaic cell, Appl. Phys. Lett., 48, 183-185, 1986

[58] N. S. Sariciftci, L. Smilowitz, A.J. Heeger, F. Wudl, Semiconducting polymers (as donors) and buckminsterfullerene (as acceptor): photoinduced electron transfer and heterojunction devices. Synth. Met., 59 , 333-352, 1993

[59] G. Yu, K. Pakbaz, A.J. Heeger, Dual-function semiconducting polymer devices: Light - emitting and photodetecting diodes, Appl. Phys. Lett., 64 , 1540-1542, 1994

[60] National Renewable Energy Laboratory, Research cell efficiency records, http://www.nrel.gov/ncpv/images/efficiency_chart.jpg

[61] F. Wudl, The chemical properties of buckminsterfullerene (C_{60}) and the birth and infancy of fulleroids, Acc. Chem. Res., 25, 157-161, 1992

[62] C. J. Brabec, A. Cravino, D. Meissner, N. S. Sariciftci, T. Fromherz, M. T. Rispens, L. Sanchez, and J. C. Hummelen, Origin of the open Circuit voltage of plastic solar cells, Adv. Funct. Mater. 11, 374-380, 2001

[63] K. Kawano, R. Pacios, D. Poplavskyy, J. Nelson, D. C. Bradley and J. R. Durrant, degradation of organic solar cells due to air exposure, Sol. Energy Mater. Sol. Cells. 90, 3520-3530, 2006

[64] M. O. Reese, A. J. Morfa, M. S. White, N. Kopidakis, S. E. Shaheen, G. Rumbles, D. S. Ginley, Pathways for the degradation of organic photovoltaic P3HT:PCBM based fevices, Sol. Energy Mater. Sol. Cells . 92, 746-752, 2008

[65] S. A. Gevorgyan, M. Jørgensen and F. C. Krebs, A setup for studying stability and degradation of polymer solar cells, Sol. Energy Mater. Sol. Cells., 92,736 -745, 2008

[66] M. Jørgensen, K. Norman, F. C. Krebs, Stability/degradation of polymer solar cells, Sol. Energy Mater. Sol. Cells. 92, 686 -714, 2008

[67] M. Lira-Cantu, K. Norrman, J. W. Andreasen, and F. C. Krebs, Oxygen release and exchange in niobium oxide MEHV hybrid solar cells, Chemistry of Materials,18, 5684-5690, 2006

[68] K. Norrman, S. A. Gevorgyan and F. C. Krebs, Water-induced degradation of polymer solar cells studied by $H_2{}^{18}O$ labeling, ACS Applied Materials & Interfaces, 1 , 102-112, 2009

[69] F. C. Krebs, S. A. Gevorgyan and J. Alstrup, A roll-to-roll process to flexible polymer solar cells: model studies, manufacture and operational stability studies, J. Mater. Chem ., 19 , 5442-5451, 2009

[70] J. A. Hauch, P. Schilinsky, S. A. Choulis, R. Childers, M. Biele, C. J. Brabec, Flexible organic P3HT:PCBM bulk-heterojunction modules with more than 1 year outdoor lifetime, Solar Energy Materials & Solar Cells, 92 , 727-731, 2008

[71] G. Li, Y. Yao, H. Yang, V. Shrotriya, G. Yang, Y. Yang, Solvent annealing effect in polymer solar cells based on Poly(3-hexylthiophene) and Methanofullerenes, Adv. Funct. Mater., 17, 1636-1644, 2007

[72] J. Li, S. Kim, S. Edington, J. Nedy, S. Cho, K. Lee, A. J. Heeger, M. C. Gupta, and J. T. Yates Jr, A study of stabilization of P3HT/PCBM organic solar cells by photochemical active TiO_x layer, Solar Energy Materials and Solar Cells, 95, 1123-1130,2011

[73] S. Jia, M. Reese, D. Laird, J. Hauch, Organic photovoltaic lifetime assessment: recommended practices, The third annual summit on OPV stability, Amsterdam, 2009

[74] P. Basu, T. H. Ballinger, J. T. Yates, Jr., Wide temperature range IR spectroscopy cell for studies of adsorption and desorption on high area solids, Rev. Sci. Inst., 59, 1321-1328, 1998

[75] C. N. Rusu, J. T. Yates, Jr., Photochemistry of NO chemisorbed on TiO_2 (110) and TiO_2 powders, J. Phys. Chem., B, 104, 1729-1737, 2000

[76] C. Féry, B. Racine, D. Vaufrey, H. Doyeux, S. Cinà, Physical mechanism responsible for the stretched exponential decay behavior of aging organic light-emitting diodes, Appl. Phys. Lett., 87, 213502, 2005

[77] M. Vogel, S. Doka, Ch. Breyer, M. Ch. Lux-Steiner, and K. Fostiropoulos, On the function of a bathocuproine buffer layer in organic photovoltaic cells, Appl. Phys. Lett., 89 , 163501, 2006

[78] S. T. Zhang, Y. C. Zhou, J. M. Zhao, Y. Q. Zhan, Z. J. Wang, Y. Wu, X. M. Ding, and X. Y. Hou, Role of hole playing in improving performance of organic light-emitting devices with an Al_2O_3 layer inserted at the cathode-organic interface, Applied Physics Letters, 89, 043502 (3 pages), 2006

[79] F. C. Krebs, K. Norrman, Analysis of the failure mechanism for a stable organic photovoltaic during 10000 h of testing, Prog. Photovolt.: Res. Appl. 15 , 697-712, 2007

[80] M. Glatthaar, M. Riede, N. Keegan, K. Sylvester-Hvid, B. Zimmermann, M. Niggemann, A. Hinsch and A. Gombert, Efficiency limiting factors of organic bulk heterojunction solar cells identified by electrical impedance spectroscopy, Sol. Energy Mater. Sol. Cells, 91, 390–393, 2007

[81] M. R. Lilliedal, A. J. Medford, M. V. Madsen, K. Norrman, F. C. Krebs, The effect of post-processing treatments on inflection points in current–voltage curves of roll-to-roll processed polymer photovoltaics, Sol. Energy Mater. Sol. Cells, 94, 2018-2031, 2010

[82] G. Socrates, Infrared characteristic group frequencies, Wiley, 1980

[83] C. C. Chuang, W. C. Wu, M. C. Huang, I. C. Huang, J. L. Lin, FTIR study of absorption and reactions of methyl formate on powdered TiO_2, J. Catal, 185, 423-434, 1999

[84] M. El-Maazawi, A. N. Finken, A. B. Nair, V. H. Grassian, Adsorption and photocatalytic oxidation of acetone on TiO_2: an in situ transmission FT-IR study, J. Catal., 191, 138-146, 2000

[85] W. C. Wu, C. C. Chuang, J. L. Lin, Bonding geometry and reactivity of methoxy and ethoxy groups adsorbed on powdered TiO_2, J. Phys. Chem. B, 104, 8719-8724, 2000

[86] J. M. Coronado, S. Kataoka, I. Tejedor-Tejedor, M. A. Anderson, Dynamic phenomena during the photocatalytic oxidation of ethanol and acetone over nanocrystalline TiO_2: simultaneous FTIR analysis of gas and surface species, J. Catal., 219,219-230, 2003

[87] K. Komaguchi, T. Maruoka, H. Nakano, I. Imae, Y. Ooyama and Y. Harima, ESR study on the reversible electron transfer from $O2^{2-}$ to Ti^{4+} on TiO_2 nanoparticles induced by visible-light illumination, J. Phys. Chem. C, 113, 1160-1163, 2009

[88] T. M. Berger, M. Sterrer, O. Diwald, E. Knozinger, D. Panayatov, T. L. Thompson, J. T. Yates, Jr., Light-induced charge separation in anatase TiO_2 particles, J. Phys. Chem. B, 109, 6061-6068, 2005

[89] T. Thompson, J. T. Yates, Jr., Surface science studies of the photoactivation of TiO_2: new photochemical processes, Chem. Rev., 106, 4428-4453, 2006

[90] A. Linsebigler, G. Lu, J. T. Yates, Jr., Photocatalysis on TiO_2 surfaces: principles, mechanisms, and selected results, Chem. Rev., 95, 735-758, 1995

[91] M. Henderson, The interaction of water with solid surfaces: fundamental aspects revisited, Surf. Sci. Rep., 46, 1-308, 2002

[92] A. Seemann, T. Sauermann, C. Lungenschmied, O. Armbruster, S. Bauer, H.-J Egelhaaf, and J. Hauch, Reversible and irreversible degradation of organic solar cell performance by oxygen, Solar Energy 85, 1238–1249, 2011

[93] J. Schafferhans, A. Baumann, A. Wagenpfahl, C. Deibel and V. Dyakonov, Oxygen doping of P3HT:PCBM blends: Influence on trap states, charge carrier mobility and solar cell performance, Organic Electronics, 11, 1693-1700, 2010

[94] T. Yamanari, T. Taima, J. Sakai, J. Tsukamoto., and Y. Yoshida, Effect of buffer layers on stability of polymer-based organic solar cells, Japanese Journal of Applied Physics 49, 01AC02-01-AC02-4, 2010

[95] T. Jeranko, H. Tributsch, N.S. Sariciftci, J.C. Hummelen, Patterns of efficiency and degradation of composite polymer solar cells, Solar Energy Materials & Solar Cells, 83, 247–262, 2004

[96] F. C. Krebs, R. Søndergaard, M. Jørgensen, Printed metal back electrodes for R2R fabricated polymer solar cells studied using the LBIC technique, Solar Energy Materials and Solar Cells, 95, 1348–1353, 2011

[97] T. A. Bull, L. S. C. Pingree, S. A. Jenekhe, D. S. Ginger, C. K. Luscombe The role of mesoscopic PCBM crystallites in solvent vapor annealed copolymer solar cells, ACS Nano, 3, 627–636, 2009

[98] W. Bagienski, M. C. Gupta，Temperature dependence of polymer/fullerene organic solar cells，Solar Energy Materials and Solar Cells,95, 933–941, 2011

[99] Vikram V. Iyengar, Efficient Solar Cells Using Ultrafast Laser Micro-Textured Silicon Surfaces, Ph.D. Dissertation, 2011

[100] K. Norrman, N. B. Larsen, and F. C. Krebs, Lifetimes of organic photovoltaics: combining chemical and physical characterisation techniques to study degradation mechanisms, Sol. Energy Mater. Sol. Cells 90, 2793-2814, 2006

[101] J. H. Lee, S. Cho, A. Roy, H. T. Jung, and A. J. Heeger, Enhanced diode characteristics of organic solar cells using titanium suboxide electron transport layer, Appl. Phys. Lett., 96, 163303-1-163303-3, 2010

[102] T. Hasegawa, S. Miura, T. Moriyama, T. Kimura, I. Takaya, Y. Osato, and H. Mizutani, Novel electron-injection layers for top-emission OLEDs, SID Int. Symp. Digest Tech. Papers, 35, 154-157, 2004

[103] C. I. Wu, C. T. Lin, Y. H. Chen, M. H. Chen, Y. J. Lu, and C. C. Wu, Electronic structures and electron-injection mechanisms of cesium-carbonate-incorporated cathode structures for organic light-emitting devices, Appl. Phys. Lett., 88, 152104-1-152104-3, 2006

[104] M. H. Park, J. H. Li, A. Kumar, G. Li, Y. Yang, Doping of the metal oxide nanostructure and its influence in organic electronics, Advanced Functional Materials, 19, 1241-1246, 2009

[105] M. I. Litter, J. A. Navio, Photocatalytic properties of iron doped titania semiconductors, J. Photochemistry and Photobiology A, 98, 171-181 , 1996

[106] C.-Y. Wang, C. Bttcher, D. W. Bahnemann, J. K. Dohrmann, A comparative study of nanometer sized Fe (III)-doped TiO_2 photocatalysts: synthesis, characterization and activity, J. Mater. Chem., 13, 2322-2329 , 2003

[107] P. Drummond, A. Kshirsagar, J. Ruzyllo, Characterization of near-surface electrical properties of multi-crystalline silicon wafers, Solid-State Electronics, 55, 29-36, 2011

[108] P. Papet, O. Nichiporuk, A. Kaminski, Y. Rozier, J. Kraiem, J.F. Lelievre, A. Chaumartin, A. Fave, M. Lemiti, Pyramidal texturing of silicon solar cell with TMAH chemical anisotropic etching, Solar Energy Materials and Solar Cells, 90, 2319-2328, 2006

[109] D. K. Schroder, Semiconductor material and device characterization, Wiley-Interscience, 2006

[110] L. M. Doeswijk, H. H. C. d. Moor, D. H. A. Blank, H. Rogalla, Passivating TiO_2 coatings for silicon solar cells by pulsed laser deposition, Applied Physics A: Materials Science & Processing, 69, 409-411,1999

[111] K. S. Nalwa and S. Chaudhary, Design of light-trapping microscale-textured surfaces for efficient organic solar cells, Optics Express, 18, 5168-5178, 2010

[112] S. B. Rim, S. Zhao, S. R. Scully, M. D. McGehee, P. Peumans, An effective light trapping configuration for thin-film solar cells, Appl. Phys. Lett., 91, 243501-1-243501-3, 2007

[113] M. Niggemann, M. Glatthaar, P. Lewer, C. Muller, J. Wagner, A. Gombert, Functional microprism substrate for organic solar cells, Thin Solid Films, 511, 628-633, 2006

[114] C. Cocoyer, L. Rocha, C. Fiorini-Debuisschert, L. Sicot, D. Vaufrey, C. Sentein, B. Geffroy, P. Raimond, Implementation of a submicrometer patterning technique in azopolymer films towards optimization of photovoltaic solar cells efficiency, Thin Solid Films, 511, 517-522, 2006

[115] L. Chen, Z. Xu , Z. Hong and Y. Yang, Interface investigation and engineering – achieving high performance polymer photovoltaic devices, J. Mater. Chem., 20, 2575-2598, 2010

[116] S. Y. Kim, K. S. Choi, Y. Park, Graphene oxide and reduced graphene oxide as hole extraction layers in organic photovoltaic cells, 2012 MRS Spring Meeting, San Francisco, 2012

[117] J. R. Manders, S. Tsang, S. Chen, T. Lai, M. J. Hartel, C. M. Amb, K. Zong, J. J. Deininger, J. R. Reynolds, F. So, Low temperature solution-processed nickel oxide hole transport layers in high efficiency organic photovoltaics, 2012 MRS Spring Meeting, San Francisco, 2012

[118] M. Anpo, Use of visible light. Second-generation titanium dioxide photocatalysts prepared by the application of an advanced metal ion-implantation method. Pure Appl Chem, 72, 1787-1792, 2000

[119] M. Fuerte, A. J. Maira, A. A. Martinez, M. Fernadez-Garcia, J. C. Conesa, J. Soria Visible light-activated nanosized doped-TiO_2 photocatalysts. Chem Commun., 24, 2718-2719, 2001

[120] H. Yamashita, M. Harada, J. Misaka, Application of ion beam techniques for preparation of metal ion-implanted TiO_2 thin film photocatalyst available under visible light irradiation: Metal ionimplantation and ionized cluster beam method. J Synchrotron Rad., 8, 569-571, 2001

[121] T. Ohno, T. Mitsui, M. Matsumura, Photocatalytic activity of S doped TiO_2 photocatalyst under visible light. Chem Lett., 32: 364-365, 2003

[122] Y. Liu , X. Chen, J. Li, C. Burda, Photocatalytic degradation of azo dyes by nitrogen-doped TiO_2 nanocatalysts. Chemosphere, 61, 11-18, 2005

[123] J. Yu, L. Zhang, Z. Zheng, J. Zhao, Synthesis and characterization of phosphated mesoporous titanium dioxide with high photocatalyticactivity. Chem Mater., 15, 2280 - 2286, 2003

[124] W. Zhou, Y. Zheng, G. Wu, Novel luminescent RE/TiO_2 (RE = Eu, Gd) catalysts prepared by in-situation sol-gel approach construction of multi-functional precursors and their photo or photocatalytic oxidation properties. Appl. Surf. Sci. 252, 1387-1392, 2006